**TECHNISCHE
UNIVERSITÄT
DRESDEN**

Determination of the γ-Ray-Angular Distribution in the Inelastic Scattering of Fast Neutrons on ^{56}Fe at nELBE

vorgelegt von

MIRCO DIETZ B.Sc.
geboren am 02.10.1989 in Zwickau

Institut für Kern- und Teilchenphysik
Fachrichtung Physik
Fakultät Mathematik und Naturwissenschaften
Technische Universität Dresden
2016

Eingereicht am 18.02.2016:

1. Gutachter: Prof. Dr. Kai Zuber
                Technische Universität Dresden
                Zuber@physik.tu-dresden.de
2. Gutachter: PD Dr. Daniel Bemmerer
                Helmholtz-Zentrum Dresden-Rossendorf
                d.bemmerer@hzdr.de
Betreuer: Dr. Arnd R. Junghans
                Helmholtz-Zentrum Dresden-Rossendorf
                a.junghans@hzdr.de

Contents

Abstract

The inelastic neutron scattering reaction on ^{56}Fe was studied at the nELBE time-of-flight facility of HZDR. The incoming neutron energy ranges in the fast neutron spectrum from 100 keV to 10 MeV, where high precision nuclear data are needed. Regarding the recent CIELO evaluation on ^{56}Fe, there is a great interest in improving the knowledge of inelastic scattering angular distribution and increasing the resolution on the few literature data of gamma-ray-angular distribution.

To investigate angular distributions of the emitted γ-rays, a new detector setup has been installed. It contains five HPGe detectors and five LaBr$_3$ scintillation detectors, which can be set under different angles. For this measurement they were positioned under 30°, 55°, 90°, 125° and 150°, relative to the beam axis. By cyclical measurement with and without the natural Fe-target the intrinsic and the neutron induced background from the setup, except the target, has been subtracted. Corrections for gamma-self-absorption inside the target and extended source efficiency were achieved using GEANT4 simulations.

The γ-ray-angular distribution data measured with the HPGe detectors are compared with data from D. L. Smith, Argonne, 1976. Due to the much better time resolution in LaBr$_3$ detectors high resolution data have been obtained and very interesting resonant structures have been observed for the γ-ray-angular distribution. In the end, the influence of angular distribution coefficient a_4 is demonstrated by a anisotropy correction factor for experiments, using only one detector under an angle of 125°.

Zusammenfassung

Die inelastische Neutronenstreureaktion an ^{56}Fe ist an der Neutronenflugzeitanlage nELBE (HZDR) untersucht worden. Ein schnelles Neutronenspektrum im Bereich von 100 keV bis über 10 MeV wird genutzt, um benötigte hoch-aufgelösten Kerndaten in diesem Bereich zu ermitteln. Es besteht ein großes Interesse, mehr Kenntnisse über die Winkelverteilung der inelastischen Streureaktion zu erlangen und die Auflösung der wenigen γ-Winkelverteilungen in der Literatur zu erhöhen, wie die aktuelle CIELO-Evaluation nahelegt. Um die Winkelverteilungen der emittierten γ's zu bestimmen, wurde ein neuer Detektoraufbau verwendet. Fünf HPGe Detektoren und fünf LaBr$_3$ Szintillations-Detektoren wurden unter 30°, 55°, 90°, 125° und 150° relativ zur Strahlachse aufgestellt. Der intrinsische und neutroneninduzierte Untergrund des Messaufbaus, außer dem Target selbst, wurden mit zyklischen Messungen mit dem Target innerhalb und außerhalb des Neutronenstrahls reduziert. Korrekturfaktoren für γ-Selbstabsorption im Target und die Effizienz einer ausgedehnten Quelle wurden mit GEANT4 simuliert. Die von HPGe-Detektoren gemessene γ-Winkelverteilung wurde mit Ergebnissen von D. L. Smith verglichen. Aufgrund der viel besseren Zeitauflösung der LaBr$_3$-Detektoren konnten hoch-aufgelöste γ-Winkelverteilung mit sehr interessanten resonanten Strukturen gemessen werden. Letztlich wird der Einfluss des Koeffizienten a_4 durch einen Korrekturfaktor für Experimente mit nur einem Detektor unter 125° gezeigt.

1. Introduction and Motivation

Neutrons are important probes for nuclear structure and for nuclear-reaction mechanisms. Studies of processes with neutrons have often suffered from the difficulty of producing sufficiently intense neutron beams with the required energy. Nuclear reactions such as $d + t \rightarrow {}^4He + n$, ${}^7Li + p \rightarrow {}^7Be + n$ etc. have been used to produce reasonably intense neutron beams by exploiting kinematic focusing, which is especially effective in a narrow energy region. Cross section measurements over a wide energy range have been mainly performed by using time-of-flight tagging after the neutrons are produced from pulsed electrons (ORELA at ORNL, GELINA at IRMM/Geel) or from protons (LANSCE at Los Alamos, nToF at CERN). According to the flight paths of 20 to 200 m and the repetition rates of 0.4 to 800 Hz realized at these installations the usable energy range goes down to some eV by using a target moderator combination and the energy resolution is in the 1% region at 1 MeV neutron energy. At CERN nToF about $10^4 - 10^5$ neutrons per s cm^2 are available at the target per energy decade. The CERN-nToF collaboration has a additional flight path of 20 m, where $\approx 10^7$ neutrons arrive – however, only with 5% energy resolution. In these four installations, the γ-rays necessarily produced with the neutrons arrive at the target some ns to μs before the neutrons. The much larger instantaneous photon flux results in a "flash" causing problems for the detection of the products from the neutron bombardment, which often are registered in devices that are also sensitive to photons.

ELBE is the first superconducting linear accelerator worldwide also used for neutron production. A great advantage is the permanently present radiofrequency that allows the acceleration of nearly any pulse repetition rate delivered by the electron gun. With the repetition rate of 100 kHz and a flight path of roughly 8 m, up to $2 \cdot 10^5 \frac{n}{s\,cm^2}$ arrive at the target. At ≈ 1 MeV, a resolution $\Delta E/E$ of $\approx 1\%$ is reached with detectors of ≈ 1 ns time resolution.

The neutron spectrum of the photoneutron source nELBE [BBE$^+$13] is similar to the spectrum of fission neutrons, which makes nELBE especially suited for the research of importance for the design of nuclear power and transmutation equipment using unmoderated neutrons. First experiments are aimed at targets of iron, which are easily available in quantities of grams and which are important e.g. as structure materials. The inelastic neutron scattering cross section and the total neutron cross section of fast neutrons are the most important quantities in a transmutation facility, such as a Generation IV reactor.
In earlier neutron-scattering experiments at nELBE, the time-of-flight (ToF) signals of incoming and inelastically scattered neutrons were detected. Energy spectra of the scattered neutrons obtained from the ToF measurement were used to determine the $(n, n'\gamma)$ cross section. In a

pilot experiment, one high-purity germanium (HPGe) detector was used to measure the γ-rays emitted from excited states in ^{56}Fe in inelastic neutron scattering. This measurement required the determination of the time-of-flight of the incident neutrons only. The analysis of the high-resolution gamma-ray spectra resulted in the determination of scattering cross sections for individual excited states in ^{56}Fe. The results were published in [BSH$^+$14]. In this experiment, the detector was positioned at 125 degrees relative to the incident neutron beam. At this angle, the Legendre polynomial of second order has a zero, which reduces the effect of angular distributions of the gamma rays on the cross sections.

However, as discussed in [BSH$^+$14], the Legendre polynomial of fourth order may cause a considerable deviation from isotropy at 125 degrees. This deviation affects the deduced cross sections and needs correction. Experimental information about the angular distributions of γ-rays following scattering of fast neutrons is scarce and inconsistent. Hence, there is also little knowledge about the influence of angular distributions on cross sections. To obtain precise experimental information about the angular distributions of the γ-rays, their intensities at various angles relative to the incident beam are measured.

This thesis presents experimental results of the measured angular distributions of γ-rays emitted in the ^{56}Fe$(n, n'\gamma)$ reaction. For this purpose, a special detector setup has been installed at nELBE. The setup is discussed in detail in sec. 3.3.1 and shown in fig. 3.4. It comprises five HPGe detectors at angles of 30°, 55°, 90°, 125° and 150°, respectively. In addition, LaBr$_3$ scintillation detectors are positioned at the identical angles in the other hemisphere. The usage of both detector types with all the advantages and disadvantages will be explicitly outlined with the analysed experimental spectra.

Furthermore, a closer look follows at literature detailing inelastic scattering on ^{56}Fe and its angular distribution. Thereafter the required theoretical background and the experiment are described. The main part delves into the data analysis and in the end, the achieved results are shown. The references used are listed in alphabetical order at the end of this thesis.

Gamma-ray and neutron angular distribution studies from the literature

A compilation of literature on experimental and theoretical studies of neutron inelastic scattering on ^{56}Fe and its angular distribution gives an overview of previous work:

A detailed description of the history of the investigation on the inelastic scattering reaction from neutrons can be found in [MF63]. In the 1930s, contributions came from P. Auger, who suggested an observed inelastic scattering reaction near his neutron source, D. Lea [Lea35] studied the behaviour of neutrons passing through matter and thereby producing γ-rays and Seaborg et al. [SGG37] finally proved, by observing the slowed down neutrons, that the γ-rays were definitely caused by inelastic scattering.

In 1956, Day [Day56] determined first yields and cross sections of the few known states of different Fe isotopes at that time. Because of the structural use in reactors, iron was studied in the second half of the last century quite intensely. Next to investigations of the thermal neutron region, there were many experiments of elastic and inelastic scattering of fast neutrons (keV - MeV) in the 1970s. The measurements of Barnard et al. [BVE+68], Voss et al. [VCK71] and Dickens et al. [DMP73] are still of value today, because they either determine cross sections over a wide MeV range (from threshold to 20 MeV) or gained high-resolution data (which are not easily achievable although the experimental technology is much better today). The measurements were often carried out with one lithium doped germanium (Ge[Li])-detector, which was set up under 125° and partial cross sections were determined. By assumption of isotropic scattering, these were normalised with 4π to the total cross section of inelastic scattering. However, some groups also measured angular distributions, either from gamma rays or the scattered neutrons:

The crucial work of D. L. Smith [Smi76] in 1976 gives γ-ray angular distributions at eleven different incident neutron energies from 0.93 to 2.1 MeV, each energy measured at mostly 12 different angles. It pointed out significant influence of the fourth order Legendre polynom and an energy dependence of the first γ-transition. Other results are only found for neutron angular distributions for neutron energy of 1088, 1236, 1311 keV by Barnard [BVE+68], which have a close to isotropic shape typical for elastic scattering of neutron proceeding mainly through s-waves. Another results of Korzh et al. (1977) [KMM+77] at E_n = 1.5, 2.0, 2.5 and 3.0 MeV (p-t-source) show very diverse data and the neutron angular distributions have a maximum close to 90°.
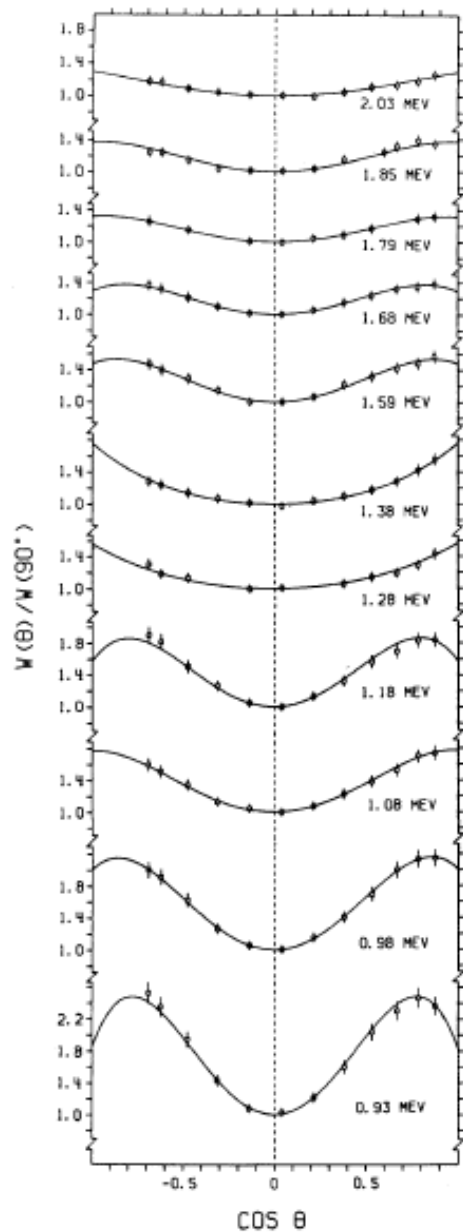

Figure 1.1.: Original graph of γ-angular distribution of inelastic scattering from threshold up to 2 MeV from D. L. Smith [Smi76].

For higher neutron energies above $4\,\mathrm{MeV}$, there are only angular distribution results of the scattered neutrons from the 846.8 keV excitation level from Kinney and Perey [KP70] and Boschung et al. [BLS71] with $4.2 \leq E_\mathrm{n} \leq 8.6\,\mathrm{MeV}$ and from D. Schmidt et al. [SMKN94] with $9.4 \leq E_\mathrm{n} \leq 15.2\,\mathrm{MeV}$. In general, the angle dependence of inelastic scattering was studied up to $25\,\mathrm{MeV}$ by Marcinkowski et al. [MFRP$^+$83] in 1983.

In total, there are several experimental results over a wide range of fast neutrons, but they all are studied with "(quasi-)monoenergetic" neutron beams, which tend to have a lower energy resolution due to the limited intensity possible and the energy loss of the beam in the neutron-producing target (see tab. 3.2 and sec. 3.2.1). To gain γ-angular distribution data with high energy-resolution by using a white neutron source and time-of-flight technique is one focus of this work, which will be compared mostly with the main work of Smith for the 1$^{\mathrm{st}}$ excited state of ^{56}Fe.

Important to mention are the most recent results on the inelastic scattering cross section. High-resolution data from the Institute of Reference Materials and Measurements (EC-JRC-IRMM) in Geel, Belgium, were presented by Negret et al. [NBD$^+$14], who measured under $110°$ and $150°$ and a flight path of $200\,\mathrm{m}$ with the Gamma Array for Inelastic Neutron Scattering (GAINS). These data have an excellent time-of-flight resolution and result with a neutron energy resolution in one per mill range. The results from recent experiment at HZDR were published also in 2014 by Beyer et al. [BSH$^+$14]. This was the pilot experiment of this work as mentioned before.

To investigate total inelastic cross sections by only measuring under two specific angles a Gaussian Method was presented in 2002 by Brune [Bru02] and it is often used at IRMM e.g. by Negret. Pursuant to the experiments, some early theoretical works were done on "Angular Distribution of Scattering and Reaction Cross Section" by Blatt and Biedenharn [BB52] and "...of Nuclear Reaction Products" by G. R. Satchler [Sat56] and "...on Angular Correlation in Inelastic Nucleon Scattering" by E. Sheldon [She63] in the 1950s and 1960s.

In 1952 Hauser and Feshbach presented "the Inelastic Scattering of Neutrons" [HF52] and over the years a statistical theory of compound and direct reaction with including angular distributions has been developed, published by Feshbach et al. [FKK80] in 1980 and continuously refined. The theoretical understanding of inelastic scattering is based on the statistical model of nuclear reactions and on scattering theory of nuclear collision. Quite recent papers were published on the random-matrix theory on compound nucleus scattering reactions by Mitchell et al. [MRW10] in 2010 and by Kawano et al. [KTW15] in 2015. Basic concepts of them will be discussed in sec. 2.

CIELO-Project

A considerable amount of data was measured in the past for ^{56}Fe as well as for natural iron. Searching on EXFOR [EXF], more than 600 entries for ^{56}Fe can be found.

The CIELO project - Collaborative International Evaluated Library Organisation, focused on neutron reactions of ^{1}H, ^{16}O, ^{56}Fe, ^{235,238}U and ^{239}Pu [CDB^{+}14] - was founded to join forces and build the first international evaluated data base. Among other things, they aimed to evaluate that huge amount of iron data. In October of 2015, there was a β-release of their new evaluated iron file [CIE]. This shows the current activities and ongoing interest on this ^{56}Fe-topic. In November 2013, there was a central workshop on NEMEA and CIELO, from which the following interesting discussions and quotations are taken.
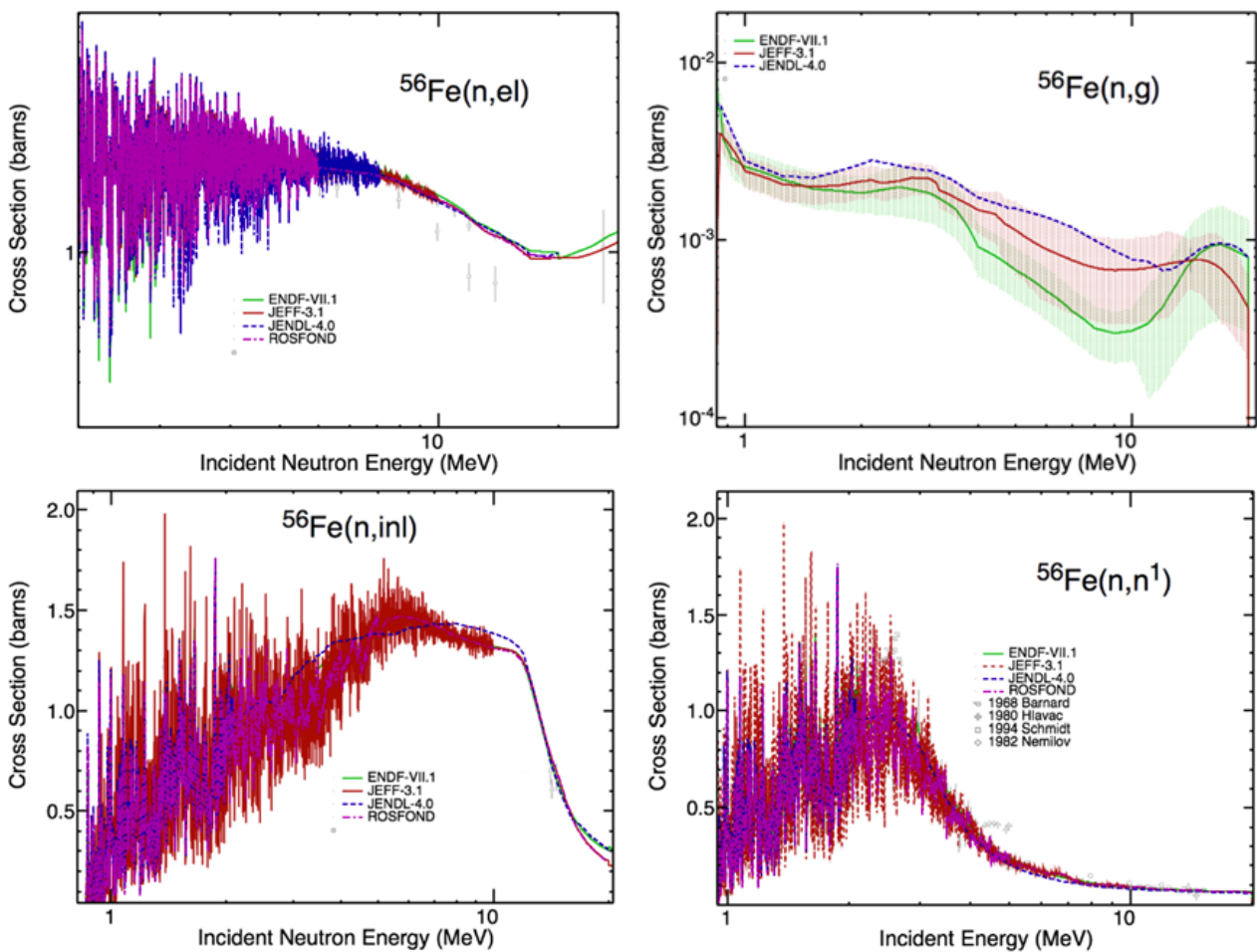

Figure 1.2.: The cross section in the fast neutron region for important reactions are plotted, such as (n, el), (n, γ), (n, inl), and (n, n^1). Plots are taken from [HTB13].

To understand different processes in ^{56}Fe-related experiments, the cross sections of possible

reactions are compared in fig. 1.2. Basically the cross section of elastic (n, el) and inelastic (n, inl) scattering are at the same order of some barns and the probability of (radiative) neutron capture (n, γ) is two or three orders of magnitude lower. Moreover the inelastic scattering cross section is dominated by the (n, n^1)-reaction, which means inelastic scattering with excitation of the first state. Similiar sharp peak structures are indicators for excited states in the compound nucleus (see sec. 2) and should be observable in every decay channel, if the resolution is sufficient. The proceedings of Herman et al. [HTB13] pointed out two interesting things about the neutron angular distributions:

"RECENTLY, A LOT OF ATTENTION HAS BEEN PAID TO ELASTIC AND INELASTIC ANGULAR DISTRIBUTIONS SINCE, IN THE PAST, THEIR IMPACT ON THE INTEGRAL PERFORMANCE OF THE EVALUATIONS HAS NOT BEEN PROPERLY RECOGNISED." and that "IMPROVING ELASTIC AND INELASTIC ANGULAR DISTRIBUTIONS WILL BE ONE OF THE MAJOR CHALLENGES IN THE CIELO EVALUATION". In the neutron angular distribution of elastic scattering, big disagreements are found between data and evaluation, as shown in fig. 1.3.
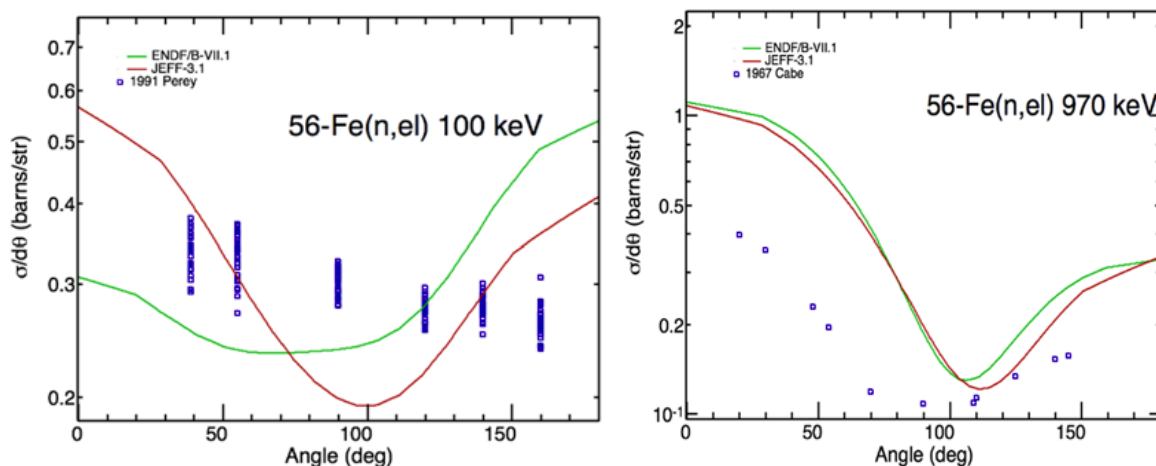

Figure 1.3.: Disagreements between evaluated and experimental data in the neutron angular distribution of elastic scattering on ^{56}Fe are shown.

In [II13], neutron angular distributions for inelastic scattering are found for E_n = 5 MeV and E_n = 14 MeV for neutrons from the first excited state (see fig. 1.4). It is again pointed out, that "THE DIVERSITY OF THE MEASURED ANGULAR DISTRIBUTIONS IS RELATIVELY LARGE, AND THUS WE CANNOT JUDGE WHICH LIBRARIES ARE BETTER TO REPRODUCE THE EXPERIMENTAL DATA. MUCH EXPERIMENTAL EFFORT IS NEEDED TO INCREASE THE ACCURACY OF NUCLEAR DATA FOR THE INELASTIC SCATTERING ANGULAR DISTRIBUTIONS". Although the quotation is about the angular distribution of scattered neutrons, a comparable observation is made by studying the literature of γ-angular distributions. For example, the JENDL 3.3 evaluation [JEN] is based on inelastic scattering data from Voss et al. [VCK71]

from 1971 and only on the γ-ray-angular distribution data from D. L. Smith [Smi76]. Thus the results of the γ-angular distributions can also contribute in this current ongoing evaluation, because no high-resolution data is yet available and found in the iron-file [CIE].
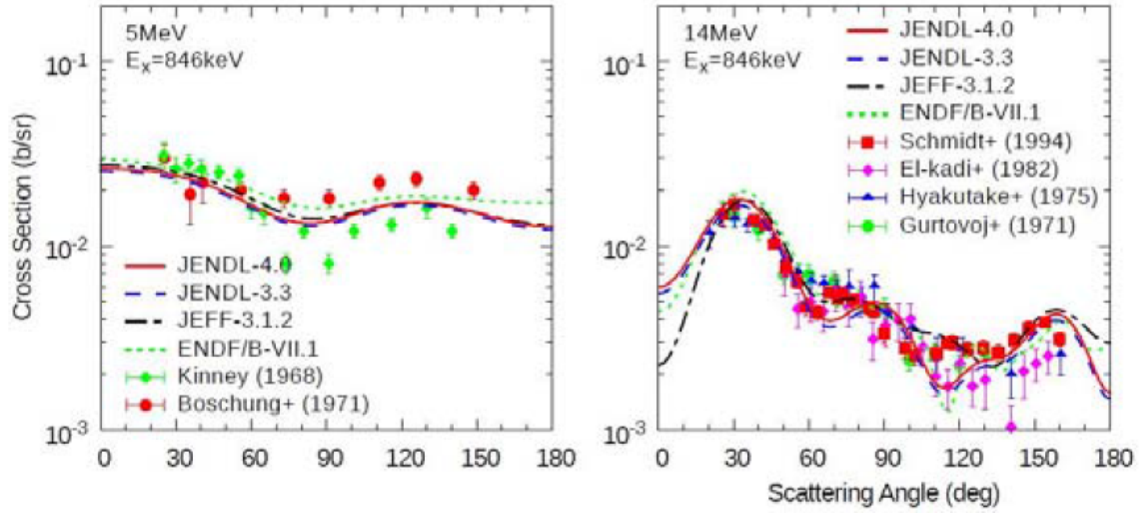

Figure 1.4.: Some angular distribution data of inelastic scattering for high neutron energy of $E_\mathrm{n} = 5\,\mathrm{MeV}$ and $E_\mathrm{n} = 14\,\mathrm{MeV}$ are taken from [II13].

2. Theoretical Ideas

Angular Distribution - Part I

In nuclear spectroscopy, the analysis of angular distribution is an important tool to determine the spins of states and the γ-ray intensity. Assuming a nuclear system with two states, an excitation with sufficient energy will populate the higher energetic state. Depending on the life time of the state, it will de-excite into the lower state by emission of a γ-ray. Both states have certain physical properties, which are described by quantum numbers. Mainly, there are the angular momentum $\vec{l}$, spin $\vec{s}$ and total momentum $\vec{j} = \vec{l} + \vec{s}$. These quantum variables are not independent and can be described by less variables - $\vec{j}$ and $\vec{s}$. Every state has also a parity π, which describes the reflexion symmetry of the wave function, if all spatial coordinates change their sign. De-excitation gammas will carry the energy $E_\gamma \cong E_i - E_f$, where E_i and E_f denote the energies of initial and final state, respectively. The gamma radiation is described by a multipole expansion with $l \geq 1$ (the spherical wave with $l = 0$ is forbidden). Common notation is a dipole transition for $l = 1$, a quadrupole transition for $l = 2$ and for $l = 3$ an octupole one. To specify the multipole character, the angular distribution is studied, which has a typical projection respective to a quantization axis, that is implied in the experiment by the projectile beam axis. Depending on the parity changes, the transitions are also divided in electric and magnetic transition (E1/E2 and M1/M2), which are linked to certain shapes of angular distribution All these features of an angular distribution were used in gamma spectroscopy to extract properties of observed transitions as one possibility to reconstruct level schemes of nuclei often step by step from ground state. In this experiment the known $2^+ \rightarrow 0^+$ transition of $847\,\mathrm{keV}$ in $^{56}\mathrm{Fe}$ will be studied, which is an E2-transition, but this will be discussed later.

Angular distributions are also important in the determination of cross section, because they are the link between total and differential cross section. The cross section σ defines the probability of certain reaction between e.g. projectile a and target b (eq. 2.1). It depends on the fluence of incoming projectiles Φ_a hitting the target, the areal density of possible scatter centres N_b, the amount of reactions taking place N [PRSZge, p. 44]. In this experiment most of the quantities also depend on the time-of-flight/energy of the incoming projectile.

$$\sigma_b(t_\mathrm{a}) = \frac{N(t_\mathrm{a})}{\Phi_a(t_\mathrm{a}) \cdot N_\mathrm{b}} \tag{2.1}$$

It has to be taken into account if the projectile beam and the target size are matched. As a result of the use of detectors with a finite opening angle in the experiment the cross section is measured mostly for certain solid angle interval, which generates the differential cross section $\frac{d\sigma}{d\Omega}$. This often depends on the angle between the neutron beam and the detector. To draw conclusions on the total cross section an integration over the differential cross sections is needed:
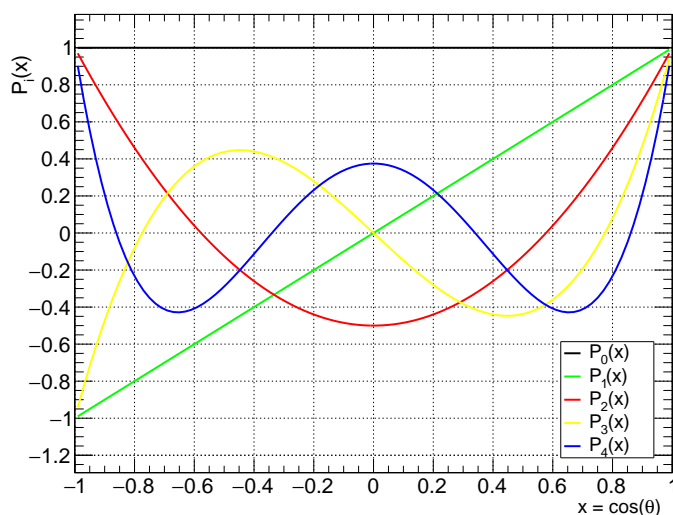
$$\sigma_{\text{tot}} = \int_{4\pi} \frac{d\sigma}{d\Omega} d\Omega = 2\pi \int_{-1}^{1} \frac{d\sigma}{d\Omega} d(\cos\theta). \tag{2.2}$$

The following expansion with Legendre polynomials gives the normalized angular distribution $W(\theta)$ [Bru02].

$$\frac{d\sigma}{d\Omega} = \frac{\sigma_{\text{tot}}}{4\pi} W(\theta) \qquad \text{with} \tag{2.3}$$

$$W(\theta) = 1 + \sum_{i=1}^{\inf} a_i P_i(\cos\theta) \tag{2.4}$$

In most nuclear physics experiments only few Legendre polynomials are requested to describe the data sufficiently and the first $P_i(x = \cos\theta)$ are listed here and plotted until the fourth order in fig. 2.1.

$$P_0(x) = 1 \qquad P_1(x) = x$$

$$P_2(x) = \frac{1}{2}(3x^2 - 1) \tag{2.5}$$

$$P_3(x) = \frac{1}{2}(5x^3 - 3x)$$

$$P_4(x) = \frac{1}{8}(35x^4 - 30x^2 + 3) \tag{2.6}$$

Figure 2.1.: Plot of the first Legendre Polynomials up to to fourth order.

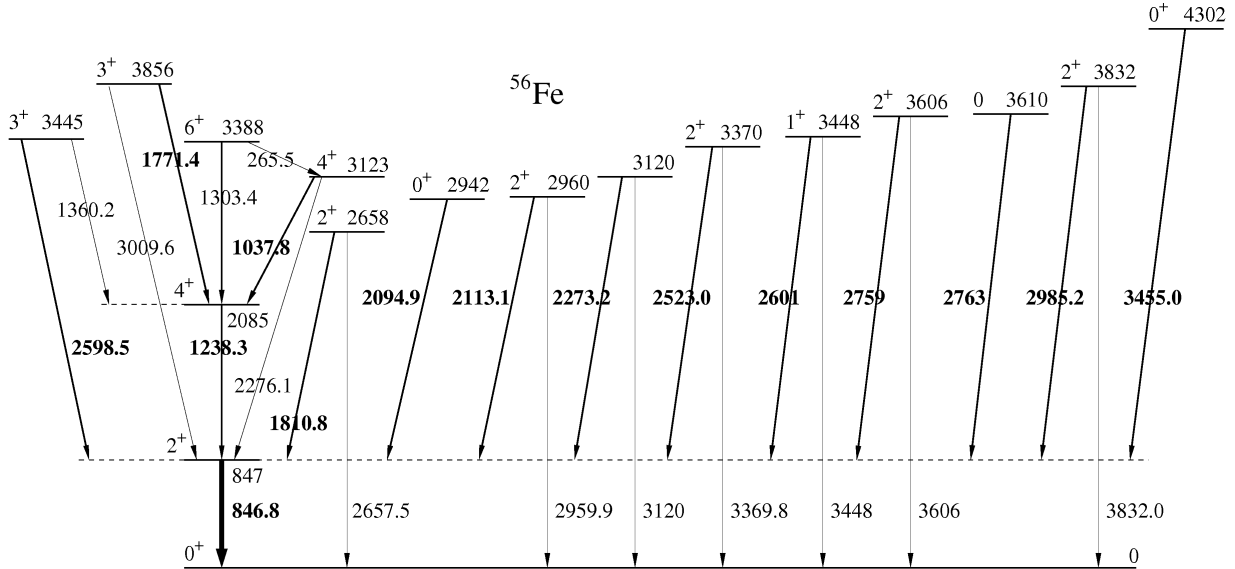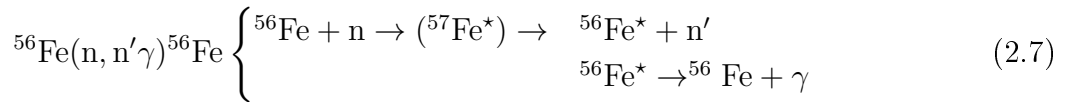# Inelastic Scattering on ^{56}Fe and Compound Nucleus Reactions

Figure 2.2.: A partial scheme of ^{56}Fe is shown - with highlighted transition energies observed in this experiment. (taken from [BSH$^+$14])

As laid out inelastic neutron scattering reaction on ^{56}Fe is the central topic of this work and it is shown in different notations:

$$^{56}\text{Fe}(\text{n}, \text{n}'\gamma)^{56}\text{Fe} \begin{cases} ^{56}\text{Fe} + \text{n} \rightarrow (^{57}\text{Fe}^\star) \rightarrow & ^{56}\text{Fe}^\star + \text{n}' \\ & ^{56}\text{Fe}^\star \rightarrow^{56}\text{Fe} + \gamma \end{cases} \quad (2.7)$$

^{56}Fe and natural iron were studied extensively and now 21 states with energy, momentum, parity and spin are more or less known until $< 4\,\text{MeV}$ excitation energy [NND]. By closer look at the level scheme in fig. 2.2, it is obvious that the first transition is very important and a significant indicator for the inelastic $(\text{n}, \text{n}'\gamma)-$ reaction, because it is populated also by the decay of almost every higher state. Why should the first transition of ^{56}Fe ($E_\gamma = 846.7\,\text{keV}$) be studied, if it is a known $2^+ \rightarrow 0^+$ transition and a quadrupole transition is expected? The reason is that the expectation will not be fulfilled in the sense of constant parameters.

D. L. Smith [Smi76] measured fluctuations in the a_2 and a_4 coefficients with varying neutron energy. He gained eleven escalating neutron energies E_n ($< 2\,\text{MeV}$), decreasing parameter a_2 and alternating a_4 (see table 5.1). The interest of this work will be higher (E_n + resolved angular distribution data. A further question is what is the explanation for the discrepancies

of non-constant parameters of the same transition, which is up to 2 MeV the only one in the inelastic scattering channel?

Analysing of nuclear reactions theorists distinguish neutron induced reactions depending on neutron incident energy and the resulting intermediate state.
For neutron energy $(E_n < 20\,\text{MeV})$ [MRW10] a "Compound Nucleus" is formed with lifetime $\tau \approx (10^{-19} - 10^{-15})\,\text{s}$ [Ber07, p. 274]. For higher neutron energies so called "direct reactions" take place, because the lifetime would be $\tau \approx 10^{-22}\,\text{s}$, which coincides with the time a particle needs traveling through the dimensions of the target nucleus. Of course, this is just a model idea. Moreover, these two extreme cases overlap or play a major or minor role in every nuclear reaction. But the angular distribution of reaction products allows to distinguish the reaction mechanism! Direct reactions scattered particle are forwards peaked. In Compound Nucleus reactions there is a symmetry around 90°.

Niels Bohr, Nobel laureate in 1922, well-known for having created one of the first atomic models based on quantum physics, hypothesized in 1936 [Boh36], that the projectile is captured and forms an intermediate compound nucleus, whose decay is independent from its formation due to its relatively long life-time. In the experiment, the compound nucleus $^{57}\text{Fe}^\star$ is formed after the incident neutron hitted the ^{56}Fe, which can be described as shown in fig. 2.3. In the Compound Nucleus there is a continuum of states above the separation energy S_n.
To model this continuum of states, one says that spacing D between two adjacent states is smaller than the width Γ of the states, so that they overlap. If $D >> \Gamma$ discrete states above S_n can be populated and will appear as a "resonance" in the cross section - a sharp, often high, peak. Mainly well described in elastic scattering theory in the epithermal region (eV), one can extract information from the properties of this resonant states, e.g. s- or p-waves. This describes the angular momentum of the incident neutron or particle with $l = 0$ (s) and $l = 1$ (p) forming the compound nucleus.

Different population of exited or continuum states in Compound Nucleus can have an influence on the inelastic scattering process and beyond. This could explain different angular distribution of one transition, because the properties like l and s of the incoming and outgoing neutron will influence state exitation in the compound nucleus.
The compound nucleus reactions have higher impact at low energies and are often connected with their characteristic symmetry on angular distribution about 90° due to the conservation of parity during the reaction. This fact limits $W(\theta)$ to only even terms of $P_i(\cos\theta)$.

The resonant structures, which will also be presented in sec. 5 might result from two possibilities. At low energies these structures can be explained by resolved resonances as it was indicated before. At energies above about 1.4 MeV neutron energy the resonant structure can be interpreted as Ericsson fluctuations. These fluctuations were first described by T. Ericson [Eri60].

Ericson fluctuations can be traced back to chaotic scattering in the regime of strongly overlapping resonances and can be explained by random-matrix theory (e.g. [MRW10]). The recent measurement of the inelastic scattering cross section by Negret et al. [NBD+14] at GAINS was analyzed in terms of the level structure of the compound nucleus. Up to a neutron energy of about 1.4 MeV the spacing of the observed resonant structures in the cross section corresponds approximately to the level spacing expected from a Backshifted Fermi-Gas Model. Above 1.4 MeV the resonant structures in the inelastic cross section have a larger spacing than the increasing level density predicts. Therefore, it can be assumed that the observed structures are Ericson fluctuations in the cross section. Finally the angular distributions should show the same fluctuations.
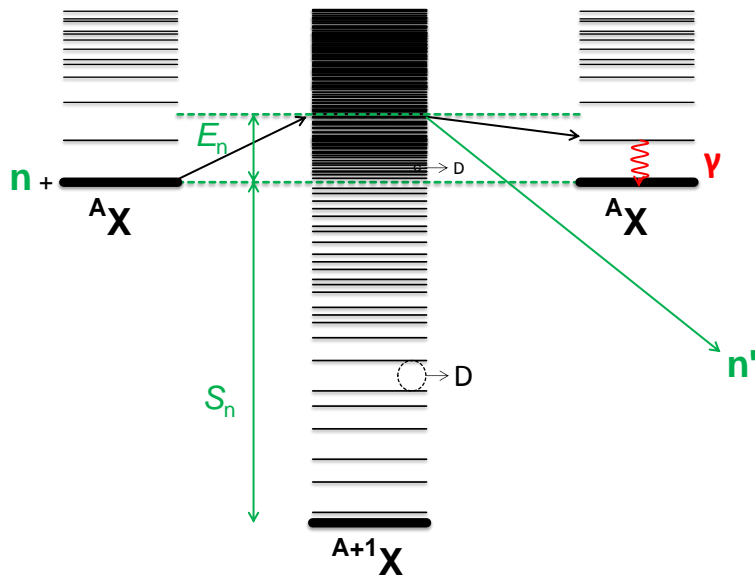

Figure 2.3.: An inelastic neutron scattering reaction in compound nucleus model is shown.

Angular Distribution - Part II

In a typical experiment for inelastic neutron scattering the target atoms in their ground states (spin parity 0^+) are randomly oriented and a neutron beam impinges from a particular direction. After formation of the compound nucleus the nuclei ($^{57}Fe^\star$) are again in a state of well defined spin and parity, but they are not randomly oriented since the compound nucleus has been prepared by absorption of a neutron on beam direction.

As a consequence radiation or particles emitted from the compound nucleus state will not be isotropic but correlated with the direction of the incoming beam. The incoming neutrons and the emitted neutrons have well defined spins and parities depending on how the intermediate compound nucleus states can be formed, e.g. s-waves, p-waves ...

By selecting a certain γ-transition, the spin parity of the residual state in the target nucleus is fixed. The quantum mechanical laws for the addition of angular momentum determine completely the γ-ray angular distribution, which generally depends on the angular momentum couplings possible.

For inelastic scattering to the first $2^+ \to 0^+$-transition of ^{56}Fe the angular correlations are determined by:

$$0^+ \xrightarrow{j_i} J_1\pi_1 \xrightarrow{j_f} 2^+ \to 0^+ \tag{2.8}$$

As it was pointed out, the incoming neutron particle with j_i is not irrelevant and to investigate the evidence Smith published, angular distributions will be measured with great interest at narrow incident neutron energy windows.

$$\sigma_\theta(E_\gamma, \Delta E_n) = \frac{d\sigma}{d\theta}(E_\gamma, \Delta E_n) = \frac{N_{\gamma,\theta}(E_\gamma, \Delta E_n)}{\Phi_n(E_n)n_{at}} \tag{2.9}$$

The differential cross section (eq. 2.9) depends on neutron energy as well as the contributions of the number of γ-rays $N_{\gamma,\theta}$ under certain angle θ and the incoming neutron fluence Φ_n, which is the number of neutrons hitting the target, depend on the neutron energy. The (areal) density of the target atoms n_{at} is determined by the iron sample.

The advantage of angular distribution is its relative measurement as ratio of differential cross sections, which will be explained in sec. 5 in detail. Relying upon the conservation of parity, the angular distribution shortens to only even orders of P_l with a_2 and a_4 mainly and the data will be fitted with:

$$W(\theta) = 1 + a_2(E_n)P_2(\cos\theta) + a_4(E_n)P_4(\cos\theta). \tag{2.10}$$

An expectation of the author is that the experimental results can give a motivational feedback for the theoretical process to get a deeper understanding of the inelastic scattering reaction and its compound nucleus states to describe the angular distribution of γ-rays from exited states with all the observed anisotropies - depending on the incident neutron energy.

3. Experiment

In this chapter the complete facility, beamline and setup of the experiment is described in detail with parameters and visualization.

3.1. ELBE - Center for High-Power Radiation Sources

The center for high-power radiation sources ELBE is a major multi-user facility at Helmholtz-Zentrum Dresden-Rossendorf (HZDR). ELBE is the superconducting **E**lectron **L**inac for beams with high **B**rilliance and low **E**mittance, which can operate on constant mode of 24 hour and 7 days a week. Electron bunches up to 77 pC are released by a pulsed injector with an energy of 250 keV and up to a 13 MHz repetition rate into the main accelerator. This consists of two linacs working with superconducting Nb cavities, which are cooled with helium to 1.8 K and have an operation frequency of 1.3 GHz. The two nine-cell radio frequency(rf) cavities with gradient of 15 MV/m each can accelerate the electron beam up to maximum 40 MeV. Other main beam parameters are listed in table 3.1.

The time structure will be handed to secondary radiation, which can be adjusted for different requirements. ELBE has different beamlines for fundamental application and physics experiments, which are listed on the next page:

Table 3.1.: Main parameters of the ELBE Linac. Parameters used in this work are given in a separate column.

Parameter	ELBE	this Experiment
Electron beam energy [MeV]	$8 - 40$	30
Max. bunch charge [pC]	77	77
Max. average beam current [μA]	1000	7.7
Normalized transverse emittance [mm mrad] (rms)	20	not measured
Normalized longitudinal emittance [keV ps](rms)	140	not measured
Micropulse duration [ps]	$1 - 10$	$1 - 10$
Micropulse repetition rate [kHz]	13000	101.325

- The electron beam can be used for detector tests especially timing resolution on the picosecond time scale.

- FELBE - Free-Electron Laser is $4-150\,\mu$m coherent infrared radiation pulsed with 13 MHz repetition rate for solid state & material research.

- γELBE - Bremsstrahlung up to 20 MeV is used in nuclear physics cave to study interesting nuclei with high energy photons (if necessary also polarized ones).

- nELBE - Neutron Time of Flight experiments to study transmission, fission and elastic and inelastic scattering reactions.

- pELBE - Positrons are used in positron spectroscopy for material research to investigate defects in crystalline material using the γ-rays from the e^+e^--annihilation.

- Laser-particle acceleration (electrons or ions) is a new application investigated currently for medical therapy uses.

- The D-T-neutron Generator operated by TU Dresden uses 14 MeV neutrons for fusion research.
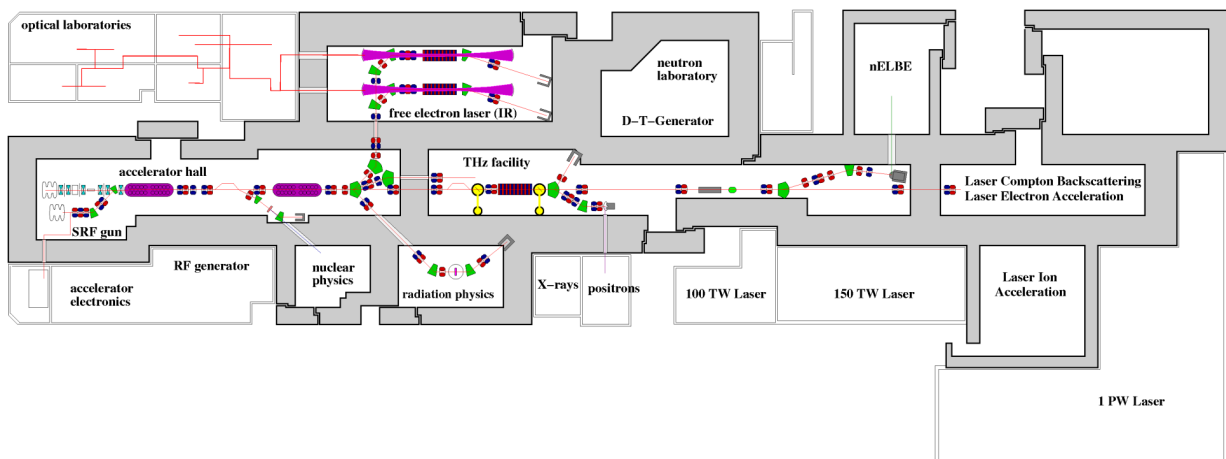

Figure 3.1.: The floor plan of the ELBE building is shown.

3.2. nELBE - Neutron Time of Flight Facility

The nELBE - Neutron Time of Flight Facility is a quite new white neutron source, established at ELBE, HZDR. It's the first photo-neutron source worldwide using an electron beam from superconducting linear accelerator (linac). The ELBE building was expanded in 2013 and the

Table 3.2.: The "Big Four" reactions for quasi mono-energetic neutron beams. Mostly solid targets are used, but also gas targets are possible. E_n range is an example with a $7\,\mathrm{MV}$ Van-de-Graaf, which is placed at IRMM, Geel.

| Reaction	Reaction (short)	Q-Value [MeV]	Energy range E_n [MeV]
$\mathrm{p} + {}^7\mathrm{Li} \to {}^7\mathrm{Be} + \mathrm{n}$	${}^7\mathrm{Li(p, n)}{}^7\mathrm{Be}$	-1.644	$0 - 5.3$
$\mathrm{p} + {}^3\mathrm{H} \to {}^3\mathrm{He} + \mathrm{n}$	$\mathrm{T(p, n)}{}^3\mathrm{He}$	-0.764	$0 - 6.2$
${}^2\mathrm{H} + {}^2\mathrm{H} \to {}^3\mathrm{He} + \mathrm{n}$	$\mathrm{D(d, n)}{}^3\mathrm{He}$	$+3.269$	$1.8 - 10.1$
${}^2\mathrm{H} + {}^3\mathrm{H} \to {}^4\mathrm{He} + \mathrm{n}$	$\mathrm{T(d, n)}{}^4\mathrm{He}$	$+17.59$	$12.1 - 24.1$

new experimental hall of 9.3x6x6 m has a lower background than the old one due to the increased distance to the wall. With a flight path of $5 - 11\,\mathrm{m}$ ToF-experiments with neutron energies of some $100\,\mathrm{keV}$ up to $10\,\mathrm{MeV}$ are possible.
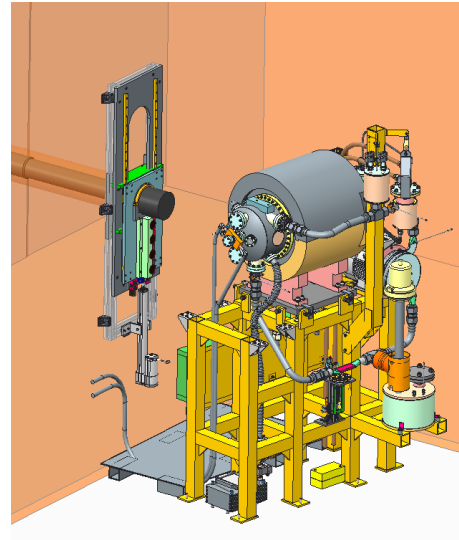
3.2.1. Photo-Neutron Source

As free neutrons decay quickly ($\tau_\mathrm{n} = 880.0 \pm 0.9\,\mathrm{s}$ according to [K.A14]), neutron beams must be produced using nuclear or photonuclear reactions. The first method of these two possibilities is the usage of so called "quasi" mono-energetic neutron reactions of light nuclei with protons or deuterons, given in tab. 3.2. Each reaction has a certain range, where the emitted neutron energy is a single valued function of the emission angle, which depends on the reaction kinematics. The energy resolution of such a neutron source is mainly determined by the energy-loss and straggling of the projectile inside the target due to its thickness, which also mainly affects the outgoing neutron flux.

The second method uses a continuous neutron spectrum produced by an electron beam impinging on a heavy target of uranium or lead. The so called "white neutron source" emits neutrons in a large energy range, and this energy will be determined by the "Time-of-Flight"-technique (see section 4.3).

To generate the neutron pulses, the very short electron bunches of ELBE are partly stopped in the dense, high Z material lead. This produces bremsstrahlung and neutrons are emitted by following $(\gamma, \mathrm{n})-$reactions. The volume of the neutron radiator framed by a molybdenum tube has a very small size of $1\,\mathrm{cm}^3$, to avoid broadened neutron pulses through multiple scattering. Almost perpendicular to the forward peaked bremsstrahlung, the isotropic emitted neutrons are guided though a collimator in the $2.5\,\mathrm{m}$ heavy concrete wall. With borated polyethylen(PE) and lead tubes, the free neutron beam is collimated to target position and the neutron/photon ratio can be improved by different absorbers before the collimator. A berylium entrance window ensures the separation of the vacua between ELBE-beamline ($10^{-9}\,\mathrm{mbar}$) and neutron radiator ($1\,\mathrm{mbar}$). The high power deposition of the electron beam would melt a solid target regardless of Z, so that a liquid lead circuit driven by an electromagnetic pump and a heat exchanger was
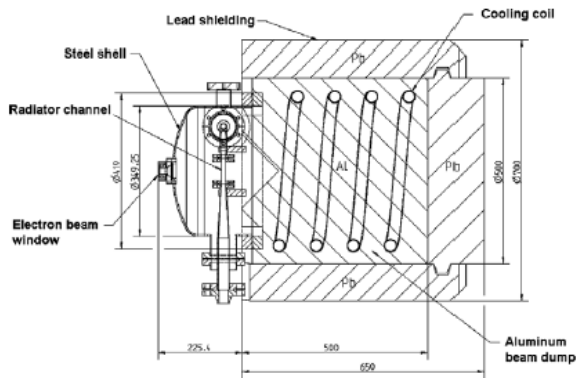
(a) Technical drawing

(b) CAD model by Armin Winter (HZDR).

Figure 3.2.: Visualizations of the photo-neutron-source. (designed and constructed at HZDR)

developed. A detailed description of the liquid lead loop plus all the nessecary surroundings as a very compact photo-neutron source is given in [ABF$^+$07], where the figure 3.2 is taken from.

nELBE - Parameters and Comparison with other ToF-Facilities

As the currently world's only neutron source at a superconducting electron linac, there are a lot of benefits, such as the time structure of the accelerator and repetition rates in the order of MHz, a great amount of bunches in a second can be used, if the electronic of experiment can also handle the occuring data. In table 3.3, there is a comparison of neutron sources worldwide. The resulting neutron flux and the energy resolution is a trade off between flight path, production target plus its dimensions, the accelerator power and resulting source strength and the time resolution of detectors (amongst others see equation 3.1).

Table 3.3.: Comparison of main parameters of nELBE with other neutron sources worldwide.([ABF+07],[SBD+12])

Facility	CERN n_TOF EAR1	CERN n_TOF EAR2	LANSCE	ORNL ORELA	IRMM GELINA	ELBE nELBE
Pulse charge [nC]	$\sim 10^3$	$\sim 10^3$	$4 \cdot 10^3$	$\sim 10^2$	$\sim 10^2$	0.08
Power [kW]	10	10	60	8	7	5
Pulse rate $[\frac{1}{s}]$	0.4	0.4	20	500	800	$1.0 \cdot 10^5$
Flight path [m]	183	20	60	40	20	$5-11$
n pulse length [ns]	>7	>7	125	>4	>1	<0.01
$E_{\min}$ [eV]	0.1	0.1	1	10	10	$1 \cdot 10^5$
$E_{\max}$ [eV]	$3 \cdot 10^8$	$3 \cdot 10^8$	$\sim 10^8$	$5 \cdot 10^6$	$4 \cdot 10^6$	$1 \cdot 10^7$
Resolution at 1 MeV [%]	0.5	5	~ 10	<1	<2	~ 1
n flux density $[\frac{1}{scm^2 E-\text{decade}}]$	10^5	$\sim 10^7$	$\sim 10^6$	10^4	$4 \cdot 10^4$	$4 \cdot 10^5$

Table 3.4.: Overview of experimental distances of the setup. The detectors were mounted on a circle with 30 cm radius to the front face of the detectors. The target is mounted with an angle $\theta_{\text{target}} = 109.5°$ to the neutron beam axis.

Equipment	distance to source [mm]
end of vacuum beam pipe	5119
HZDR Uranium fission chamber (front)	5847
PTB (H19) Uranium fission (center)	6232
target position	8300

Table 3.5.: The natural abundances of stable iron isotopes [NND], the target is composed of.

Isotope	Abundance [%]
^{56}Fe	91.754 ± 0.036
^{54}Fe	5.845 ± 0.035
^{57}Fe	2.119 ± 0.010
^{58}Fe	0.282 ± 0.004

3.3. Angular Distribution Experiment

To study the angular distribution of γ-rays in an efficient way, a special setup and number of detectors is requested. In the 1970s, the group of D. L. Smith [Smi76] used only one (Lithium doped)- Germanium detector and switched postion and neutron energy for every new setting. It took probably some months to complete the experiment. The ANL fast neutron generator produced quasimonoenergetic neutrons. The experiment might also have been possible at an electron accelerator. But the ^{7}Li$(p, n)^{7}$Be neutrons with their resolution of 50 keV were well suited for the use with a HPGe detector.

Today, beam times are shorter and a more efficient experiment is designed with a number of several different detectors (see fig. 3.3 and 3.4), employing a white neutron spectrum and the time-of-flight technology.

3.3.1. The Setup - Target, Detectors and Fission Chambers

The target forms a cylindric disk of natural iron with 79.5 mm diameter and 4.5 mm thickness and its mass is determined as 172.103 g. In table 3.5, the isotopic abundances of iron are listed. The γ-ray angular distribution from ^{56}Fe$(n, n'\gamma)$ can be investigated quite well due to its high natural abundance and an enriched target is not necessary.

At flight path $s = 8300$ mm, the target is positioned and in 300 mm circular distance ten detectors were set up (see fig. 3.3 and 3.4). Five lanthanum bromide scintillation (LaBr$_3$) and five high-purity germanium (HPGe) detectors are mounted under angles of 30°, 55°, 90°, 125°
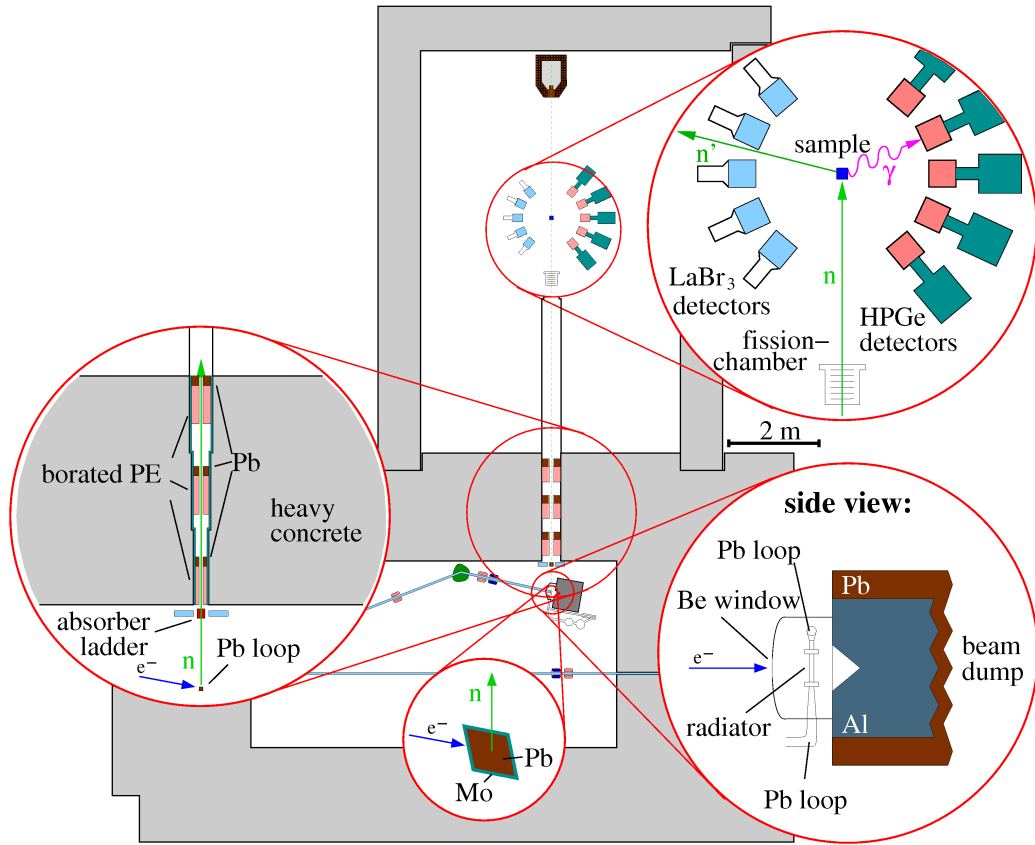
Figure 3.3.: Floorplan of the new nELBE facility. The insets show a sideview of the liquid kead circuit, where the photoneutron source is located, a cross section of the Mo tube, the neutron beam collimator consisting of Pb and borated PE elements and the experimental setup for γ-ray angular distibution measurements using five HPGE and five LaBr$_3$ scintillation detectors.

and 150°, relative to the beam axis. The scintillation detectors are very fast($\Delta t \approx 300\,\text{ps}$) and read out with Hamamatsu R2059 photomultipliers. The HPGes are semiconductor detectors and for high resolution γ-spectroscopy they have to be cooled with liquid nitrogen (77 K) to reduce the leakage current and noise. At nELBE, this can be realized with an automatic filling and observation system.

In front of the target, two fission chambers were placed (distances listed in table 3.4). Both chambers are based on fissile ^{235}U and can measure the absolute neutron flux to determine energy differential cross sections for inelastic neutron scattering. H19 is a standard fission chamber from PTB ("Physikalisch-Technische Bundesanstalt", Braunschweig), which is used as a reference in many neutron related experiments. The other fission chamber was constructed at HZDR with a different design and needs the reference for its absolute calibration. Due to the fact that their data are not yet analysed in this work, they are not further discussed here, but more information can be found in the related PhD-thesis of Toni Kögler [K16].
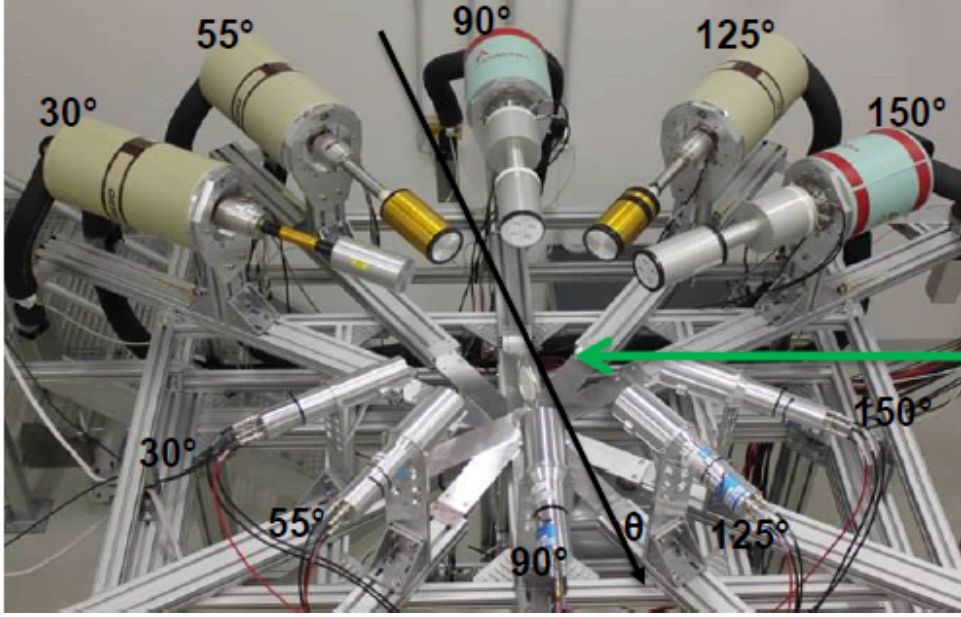
Figure 3.4.: New setup to study angular distributions with LaBr$_3$ and HPGe detectors.

In a ToF experiment, the neutron energy resolution is not only dependent on the source and its distance, but also on the detectors used. The relativistic equation (3.1) shows this connection

$$\frac{\Delta E}{E} = \gamma(\gamma + 1)\sqrt{\left(\frac{\Delta t}{t}\right)^2 + \left(\frac{\Delta d}{d}\right)^2} \tag{3.1}$$

with $\Delta t \approx 1\,\mathrm{ns}$ as time resolution of (detector + accelerator) and Δd the uncertainty of the flight path. The flight path is a trade-off between the energy resolution and the neutron flux at the measuring point. It was chosen in order for target size and neutron beam spot size to match.

In the past, beam profil and size was investigated by Beyer et al. [BBE$^+$13] for the nELBE facility. With a well shaped profile and the linear equation (3.3), the neutron beam size of $(80 \pm 1)\,\mathrm{mm}$ is in good agreement with the target diameter. For the analysis, it is generally assumed that the target was homogenueous and larger than the neutron beam.

$$d = a + b \cdot l \quad \text{with } a = -5.5(4)\,\mathrm{mm}; \ b = 0.103(1)\,\frac{\mathrm{mm}}{\mathrm{cm}} \tag{3.2}$$

$$d_{\mathrm{beam}}(l = 830\,\mathrm{cm}) = 80 \pm 1\,\mathrm{mm} \tag{3.3}$$

4. Data Analysis

The experiment and data acquisition was done from the 15th to 24th of September in 2014. Repeated measurements with target in- and outside the neutron beam were performed to determine the neutron induced background through a substraction afterwards. Moreover there were background and γ-calibration measurements without neutron beam. The total data in list-mode-data(lmd)-files add up to almost 300 GB. Two programmes, developed at GSI Darmstadt, were used: MBS (Multi-Branch-System) for data acquisition, which enables fast data transfer in self-structured lmd-files and Go4 (plus some ROOT scripts) for data analysis (Manuals are found in [EK10] and [AMATB$^+$15]). After removal of files with small gain shifts (sec. 4.2) 1440 lmd-files were used in the analysis, which result in the experimental periods shown in table 4.1. The following calibrations were carried out:

1. energy calibration (sec. 4.1)

2. efficiency calibration including a simulation of the extended source geometry (sec. 4.1 and sec. 4.5.3)

3. Test of gain stability of the detectors in data taking (sec. 4.2)

4. Time-of-Flight (ToF) calibration (sec. 4.3)

5. ToF channel dependent dead time correction (sec. 4.4.1)

After the calibrations, the correlation between γ-ray energy and neutron time-of-flight (ToF) is considered (sec. 4.4.2). With projection to different neutron energy regions, the yield of the 847 keV γ-transition is deduced by a Gaussian fit procedure (sec. 4.4.3) and the correction for the different detection efficiencies. Furthermore, the absorption of γ-rays inside the target material is simulated for each detector and with this correction, neutron energy dependent γ-ray intensities are calculated. Finally by a normalisation to 90° data γ-ray-angular distributions are achieved for different incident neutron energy resolution depending on the type of detector (sec 5).

Table 4.1.: Measurement periods of the used data.

Typ of measurement	Times [h]
Target inside beam	103
Target outside beam	38
sources & background (without beam)	59
sources:	
^{137}Cs	2.2
^{60}Co	2.7
^{88}Y	4.8

Table 4.2.: Energy calibration of the five lanthanum bromide detectors (LaBr$_3$). A linear fit function of $E_\gamma = f \cdot Q[\text{ch}] + b$ was used.

detector	number	factor f $\left[\frac{\text{keV}}{\text{ch}}\right]$	offset b [keV]
LaBr$_3$	01	7.922 ± 0.035	-414.9 ± 6.0
	02	7.546 ± 0.014	-277.3 ± 2.4
	03	7.869 ± 0.013	-340.3 ± 2.2
	04	7.768 ± 0.054	-426.4 ± 8.9
	05	7.429 ± 0.031	-435.8 ± 5.4

Table 4.3.: Energy calibration of the five High-Purity Germanium detectors (HPGe). A linear fit function of $E_\gamma = f \cdot Q[\text{ch}] + b$ was used.

detector	number	factor f $\left[\frac{\text{keV}}{\text{ch}}\right]$	offset b [keV]
HPGe	01	1.0523 ± 0.0004	-76.8 ± 0.4
	02	1.0503 ± 0.0003	-74.1 ± 0.3
	03	1.0618 ± 0.0003	-89.2 ± 0.4
	04	1.0444 ± 0.0002	-66.6 ± 0.2
	05	1.0406 ± 0.0001	-59.9 ± 0.1

4.1. Energy and Efficiency Calibration

Gamma-ray interact with the detector material by photo-effect, compton scattering and/or if the energy is above $1.02\,\mathrm{MeV}$ pair production. The electron-ion pair created in the HPGe crystal or in the $\mathrm{LaBr_3}$ create a charge signal or a flash of scintillation light respectively. Each HPGe charge signal is integrated by the preamplifier and a spectroscopic amplifier and digitized by a peak sensitive ADC charge. A fast timing amplifier is used to create a timing signal using a constant fraction discriminator (CFD) and digitized by a multi hit multi event TDC. The fast PMT signals of the $\mathrm{LaBr_3}$ scintillators are splitted passively. The timing signal is also created by constant fraction discriminator. The signals are put on a QDC and a multi hit multi event TDC. Most of the data analysis result from the time and charge information of these converted signals. In the first step, an energy calibration of each detector will be carried out and the efficiency of particle detection will be determined.

Therefore, measurements with the typical γ-ray calibration point sources $^{137}\mathrm{Cs}$, $^{60}\mathrm{Co}$ and $^{88}\mathrm{Y}$ were done and the measurement periods are shown in tab. 4.1. From received γ-ray spectra, the mean channel and their uncertainty of the known γ-ray lines, which are tabulated in table 4.4, are obtained by fitting a Gaussian peak function. The results of the linear energy calibration can be found in table 4.2 and 4.3.

Efficiency Calibration

With the help of the calibration source measurements, the absolute photopeak efficiency can be determined experimentally. This efficiency is required to determine the numbers of emitted γ-rays from the inelastic scattering reaction to be studied. The difference between the absolute efficiency ϵ_{abs} and intrinsic efficiency ϵ_{int} is, that the former is calculated as the ratio of the number of recorded pulses divided by the number of γ-rays emitted from the γ-ray-source, while the latter is determined from the ratio relative to the gamma-rays incident on the detector. The relation between them is

$$\epsilon_{\mathrm{abs}} = \epsilon_{\mathrm{int}} \cdot \left(\frac{\Omega_{\mathrm{det}}}{4\pi}\right), \tag{4.1}$$

where Ω_{det} is the solid angle extented by the detector. The formula for the determined experimental (absolute) efficiency is shown in Eg. 4.2.

$$\epsilon(E_\gamma) = \frac{N_{\mathrm{peak,det}}}{N_{\gamma,\mathrm{source}}}(E_\gamma) \tag{4.2}$$

The area of a Gaussian fit of the photopeak gives the numbers of γ-rays detected $N_{\mathrm{peak,det}}$. The emitted γ-rays of the source result from their activity A_{meas} at the time of measuring, their half-life $T_{1/2}$ and the exposed time t_{meas}. Knowing the numbers of decayed nuclei there are

branching ratios δ, which describe the probability of a γ-ray emission of certain E_γ. In total this determines the number of emitted γ-rays $N_{\gamma,\text{source}}$:

$$N_{\gamma,\text{source}} = \delta \cdot N_{\text{decay}} = \delta \int_{t_1=T_{\text{start}}}^{t_2=T_{\text{stop}}} A(t')\mathrm{d}t' = \delta A_0 \int_{T_{\text{start}}}^{T_{\text{stop}}} \mathrm{d}t (\frac{1}{2})^{\frac{t}{T_{1/2}}}$$
$$= \delta A_0 \cdot \frac{T_{1/2}}{\ln(2)} \left[1 - (\frac{1}{2})^{\frac{t_{\text{meas}}}{T_{1/2}}} \right] \tag{4.3}$$

An assumption of uncorrelated uncertainties between δ and N_{decay} leads to eq. 4.4. However, for the calculation of numbers of decay a correlation between activity and half-life is used, so the Gaussian uncertainty propagation is shown in eq. 4.5. The 1σ uncertainty for source activity was taken from their certifications. An overview of the results is listed in table 4.4.

$$\Delta N_{\gamma,\text{source}} = N_{\gamma,\text{source}} \cdot \left(\frac{\Delta\delta}{\delta} + \frac{\Delta N_{\text{decay}}}{N_{\text{decay}}} \right) \quad \text{with} \tag{4.4}$$

$$\Delta N_{\text{decay}} = \sqrt{N_{\text{decay}}^2 \left[\left(\frac{\Delta A_0}{A_0} \right)^2 + \left(\frac{\Delta T_{1/2}}{T_{1/2}} \right)^2 \right] + \left(A_0 T_{\text{meas}} \cdot (1/2)^{\frac{T_{\text{meas}}}{T_{1/2}}} \right)^2 \left(\frac{\Delta T_{1/2}}{T_{1/2}} \right)^2} \tag{4.5}$$

The efficiencies (listed in tab. A.1) for the five different γ-ray-energies are calculated with less than 2% uncertainty. These results are fitted for each detector with a polynomial of 2$^\text{nd}$ order (see fig. 4.1) to determine the efficiency values at the interesting E_γ from inelastic scattering. Due to the fact that the first three transition in ^{56}Fe have very similiar γ-ray energy to the calibration sources, their uncertainties were chosen with 2% from the physical point of view instead of using the higher mathematical uncertainties from the fit parameters. The results for $E_\gamma = 847\,\text{keV}$ are shown in tab. 4.5.

Table 4.4.: Efficiency related parameters are shown, which are described in eq. 4.3 and 4.5. $T_{\frac{1}{2}}$ and δ values are taken from NNDC [NND].

source	number	$T_{\frac{1}{2}}$	A_{ref} [kBq]	reference date	measure date	A_{meas} [kBq]
^{137}Cs	AY 723	$30.08 \pm 0.09\,\mathrm{y}$	42.50 ± 0.57	$01/07/93\ 12:00$	$23/09/14\ 11:33$	26.06 ± 0.35
^{60}Co	NU-157	$1925.28 \pm 0.14\,\mathrm{d}$	41.90 ± 0.63	$01/11/05\ 12:00$	$23/09/14\ 13:49$	13.01 ± 0.20
^{88}Y	$1714-92$	$106.63 \pm 0.03\,\mathrm{d}$	36.81 ± 0.37	$01/04/14\ 12:00$	$24/09/14\ 10:21$	11.73 ± 0.12

source	t_{meas} [h]	N_{decay}	E_{γ} [keV]	δ	$N_{\gamma,\mathrm{source}}$
^{137}Cs	2.24	$(2.100 \pm 0.029) \cdot 10^8$	661.657 ± 0.003	0.851 ± 0.002	$(1.787 \pm 0.029) \cdot 10^8$
^{60}Co	2.69	$(1.259 \pm 0.019) \cdot 10^8$	1173.228 ± 0.003	0.9985 ± 0.0003	$(1.257 \pm 0.019) \cdot 10^8$
			1332.492 ± 0.004	0.999826 ± 0.000006	$(1.259 \pm 0.019) \cdot 10^8$
^{88}Y	4.81	$(2.030 \pm 0.020) \cdot 10^8$	898.042 ± 0.003	0.937 ± 0.003	$(1.902 \pm 0.025) \cdot 10^8$
			1836.063 ± 0.012	0.992 ± 0.003	$(2.014 \pm 0.026) \cdot 10^8$

Table 4.5.: The fitted efficiency values atthe transition energy of the 1st excited state of ^{56}Fe, $847\,\mathrm{keV}$ are shown. A factor of 10^{-4} has to be applied.

HP Ge	30°	55°	90°	125°	150°
ϵ_{847}	7.26	11.77	10.53	11.52	11.22
$\Delta\epsilon_{847}$	0.15	0.24	0.21	0.23	0.22

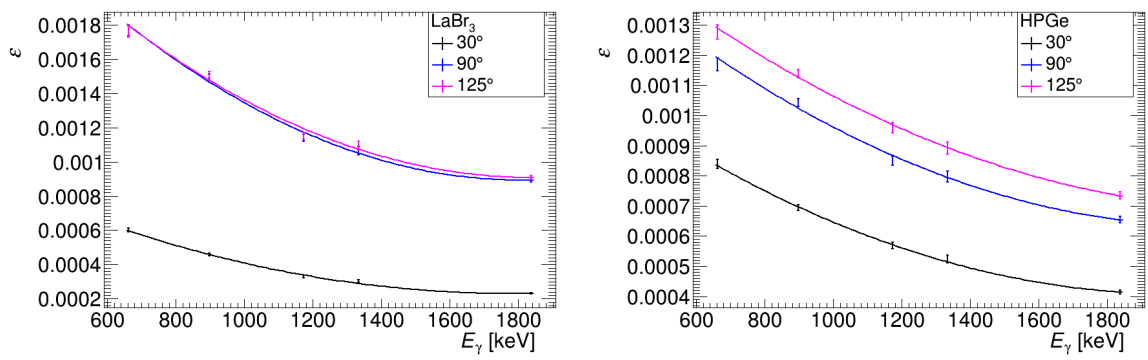| LaBr$_3$	30°	55°	90°	125°	150°
ϵ_{847}	4.88	15.79	15.17	15.34	15.57
$\Delta\epsilon_{847}$	0.10	0.32	0.30	0.31	0.31

Figure 4.1.: A selection of efficiency values are shown and fitted. The other detectors have very similar effeciency as the upper curves.

4.2. Gain Stability of Detectors

During a several day long measurement, the gain stability of scintillation detectors using PMTs must be monitored in order to be able to use time independent gates in the accumulated histograms (fig. 4.6) from the list mode data analysis. The electron capture decay of ^{138}La in the LaBr$_3$ crystal leads to the emission of a 1436 keV γ-ray. Most of the time it sums up with a 32 keV x-ray to 1468 keV. This intrinsic activity [NCB$^+$07], together with the 1460 keV from ^{40}K decay of the environment, has been used as a marker for the gain stability of the detectors used. The peak was analysed with amplitude, mean, width and χ^2 of a Gaussian distribution to every file, which accords in average to a five minutes interval.

In contrast to other experiments [Rei16], a good gain stability was found here. Through the data taking of six days, only two short drifts in the LaBr$_3$ detector set up under 90° (see fig. 4.2) were observed. Hence, files with a mean value outside of one width were not taken into account of the analysis (see appendix fig. A.1). With 120 rejected compared to the 1441 used files, there was overall a stable data taking and the strong conditions to cut instabilities shall only ensure fixed width and no gain drifts in the data. The application of gain matching in this case would not be worthwhile, if most of data can be analysed without it.
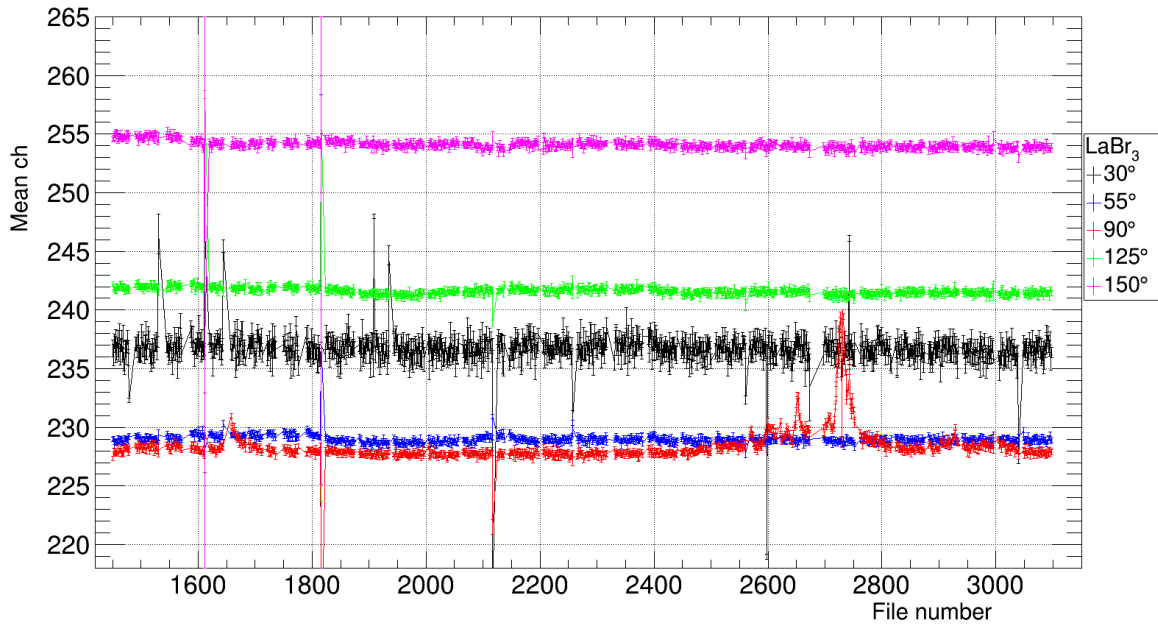

Figure 4.2.: The mean value of intrinsic background peak (1460 keV) position in [ch] is recorded for all five LaBr$_3$ over all lmd-files for testing gain stability.

4.3. Time-of-Flight Calibration

The kinetic energy of fast neutrons can be determined by measuring over a known flight path. their time-of-flight using a pulsed neutron beam. In the described experiment of the γ-ray angular distribution, the neutron time-of-flight (ToF) is determined by the timing information deduced from the LaBr$_3$ and HPGe γ-ray detectors using a multi hit multi event TDC. The sum of a time-of-flight is measured for a flight path of about $s_1 = 8.3\,\mathrm{m}$ from the source to the target and the known ToF of the γ-rays from the target to the detector position $s_2 = 0.3\,\mathrm{m}$. The absolute scale of the ToF is determined by the measurement of the ToF of bremsstrahlung from the photo-neutron source to the detectors. The ToF_{rel} is determined assuming a direct flight path (s_1) of the neutrons or bremsstrahlung from the source to the target and then an emission or a scattering of γ-ray to the detector (s_2). It is measured relative to the radiofrequency signal of the accelerator. The time-of-flight of the γ-flash (ToF_γ) is used to determine the absolute scale and to correct for the unknown internal TDC offset and cable length(t_{x}).

$$ToF_\gamma = t_\gamma + t_{\gamma 2} + t_x = \frac{s_1}{c} + t_{\gamma 2} + t_x$$

$$ToF_{\mathrm{rel}} = t_1 + t_2 + t_x = t_{\mathrm{n}} + t_{\gamma 2} + (ToF_\gamma - \frac{s_1}{c} - t_{\gamma 2})$$

$$t_{\mathrm{n}} = ToF_{\mathrm{rel}} - ToF_\gamma + \frac{s_1}{c} \tag{4.6}$$

The kinetic energy of neutrons is calculated by equation 4.7 with its actual time-of-flight t_{n}. It is obvious that the energy resolution is influenced by the flight path measurement and the timing features of the detectors.

$$E_{\mathrm{kin,n}} = m_{\mathrm{n}} c^2 \left(\frac{1}{\sqrt{1 - (\frac{s_1}{t_{\mathrm{n}} \cdot c})^2}} - 1 \right) \tag{4.7}$$

The ideal tool to understand the neutron time-of-flight spectrum is the LaBr$_3$ scintillator due to its excellent time resolution of $\approx 300\,\mathrm{ps}$ (σ). The raw peak position in TDC units, depicted in fig. 4.3, still depends on cable lengths for example and thus different detectors can not be compared directly. However, by comparison of the TDC spectra of "target in" and "target out" of the beam, the assumed gamma flash is found, which is sometimes separable depending on angle of the detector. For detectors under backward angles, the difference between the gamma flash from the assumed flight path and from the diversed path is observable. One possibility of the diversed path would be a scattering inside one of the fission chambers. A simple approximation based on Pythagoras is done to calculate the difference of time-of-flight of γ-rays being scattered at the center of the fission chambers and take a shortcut (s_3) to the detector without any interaction with the target (see tab. 4.6). Due to its worse time resolution, the gamma flash in the HPGe spectra was more challenging to fit and a comparison of "target in" and "target out" spectra is added in the appendix (fig. A.3).
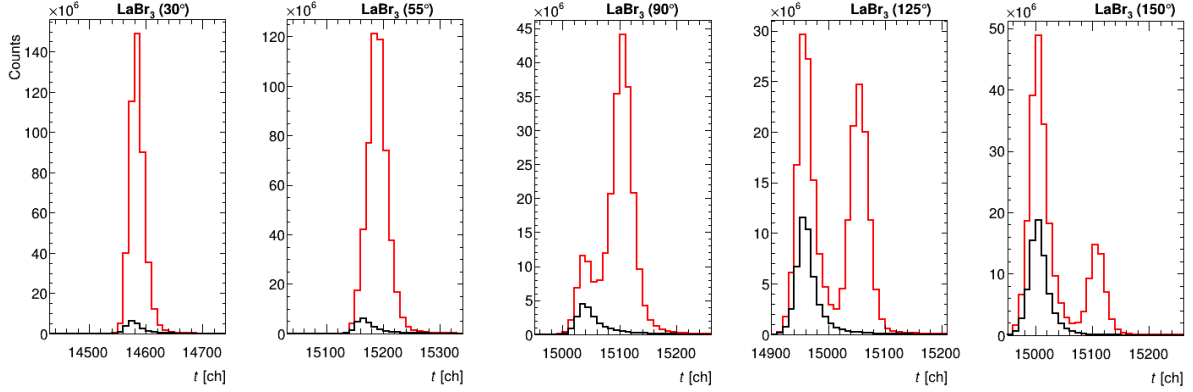
Figure 4.3.: The gamma flash of LaBr$_3$ with target in (red) and out (black) of the beam. Time scale is in TDC units of 24.414 ps/ch, which will be further converted into ns. The differences are shown in path length and time in table 4.6.

Table 4.6.: The peak means of the LaBr$_3$ gamma flash spectra, shown in fig. 4.3, and the theoretical calculated different ToF (Δ_{th}) of straggled γ-rays at the center of the fission chambers are listed. The approximation shows the same trend, which supports the understanding of the "gamma-flash".

	$\theta[°]$	ch$_{\gamma 1}$	ch$_{\gamma 2}$	Δ_{exp} [ch]	Δ_{th} [ch]
1	30	14584	—	—	5
2	55	15189	—	—	16
3	90	15053	15102	49	38
4	125	14960	15054	94	62
5	150	15005	15107	102	76

4.4. Data Analysis Procedure

The Data Acquisition (DAQ) system was adapted to record the signals from all ten detectors and the two fission chambers simultaneously. The schematic is shown in appendix fig. A.2. The LaBr$_3$ and HPGe time signals are converted by a multi hit multi event TDC.

The respective energy signals are converted by a QDC(LaBr$_3$) with a gate length of 150 ns and a peak sensing ADC (HPGe) with a gate of 6000 ns. Each detector is allowed to trigger the DAQ and initialize an event, so that energy and timing information from all detectors is written to a list-mode data file. The data structure of these files is programmed by the MBS software. In addition, scaler values of detector rates, data rate, trigger rate and real, live and dead time were recorded to monitor the experiment and to determine the dead time correction, inter alia. As each detector triggers the DAQ, the spectra of all other detectors that did not trigger in the same event contain the zero value in the QDC (ADC) spectra. Moreover, coincident back-

ground γ-ray can increase the amount of trigger hits in one event, which is avoided by allowing only events with one trigger hit in the analysis.

Further details of the MBS data structure, the DAQ itself and electronics can be found in the PhD thesis of the beamline scientist R. Beyer [Bey14].

To visualize the data analysis, a (process) scheme is shown in fig. 4.4. According to the self-defined MBS file structure, the raw data are unpacked and arr by histograms for QDC/ADC and TDC information for every detector. The time-of-flight (ToF) signals are gained through the accelerator reference time. After some calibration, the event correlations between the neutron time-of-flight and the γ-ray energy in the QDC/ ADC are accumulated in 3D plots. These are corrected with a global ToF-channel dependent dead time factor, as described in the next section. By a subtraction of "target in" and normalized "target out" spectra, the interesting spectra (fig. 4.6) are obtained for each detector. According to the time-of-flight technique, γ-ray spectra are projected for neutron energy windows. By analysing and fitting these, γ-ray intensities $N_\theta(E_\gamma, \Delta E_n)$ of transitions from inelastic scattering are determined depending on the incident neutron energy.
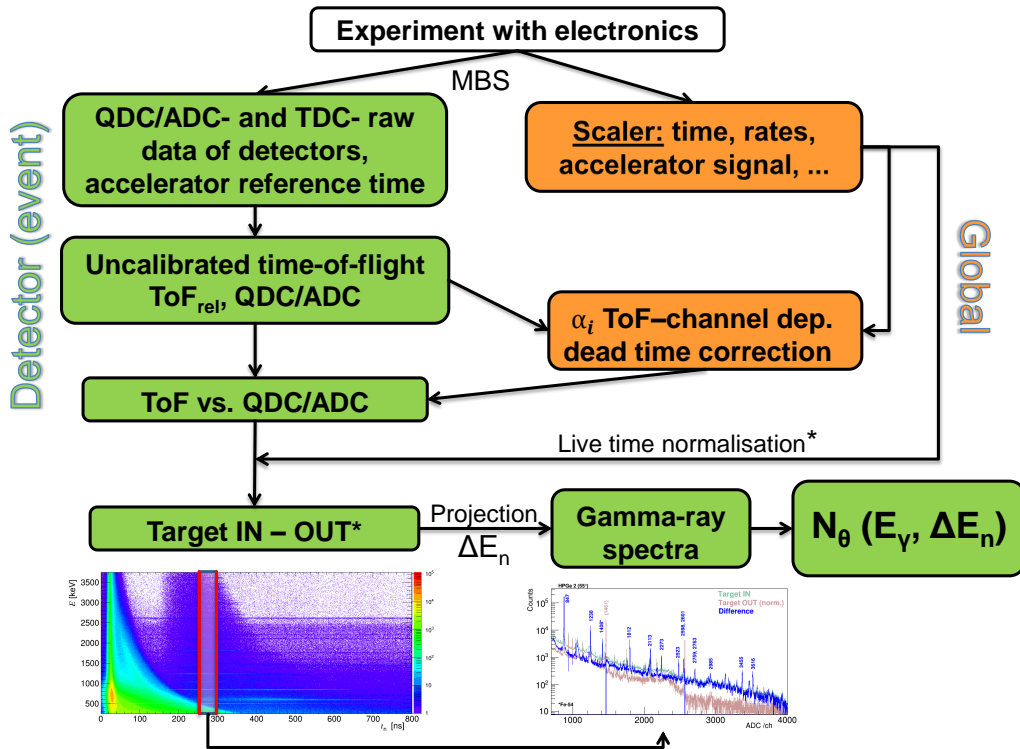

Figure 4.4.: Data analysis scheme.

4.4.1. ToF Channel Dependent Dead Time Correction

At the photo-neutron source nELBE, a pulsed beam of electrons produces bremsstrahlung in a liquid lead target and at the same time neutrons by photonuclear reactions. Due to the short flight path, the bremsstrahlung arrives after almost $28\,\mathrm{ns}$ at the target position. About $140\,\mathrm{ns}$ later, the neutrons start to arrive. After about $2\,\mu\mathrm{s}$, the slowest neutrons have arrived and the sequence is repeated with a new electron bunch from the accelerator every $10\,\mu\mathrm{s}$. The dead time per trigger event is approximately $15\,\mu\mathrm{s}$. As the instantaneous rate of bremsstrahlung quanta and neutrons is not constant, the dead time correction due to data acquisition dead time per trigger event is time-of-flight dependent and not a constant factor.

The dead time of each event is recorded in the list-mode data. Consequently the distribution of blocked time-of-flight intervals for all accelerator periods can be derived from the list-mode data analysis, see fig. 4.5. The ratio of possible unblocked periods to total accelator signals will be the inverse correction factor (see eq. 4.8). A detailed concrete description of calculation of the dead time correction factor α_i for each ToF channel was first published in [BBE+13].

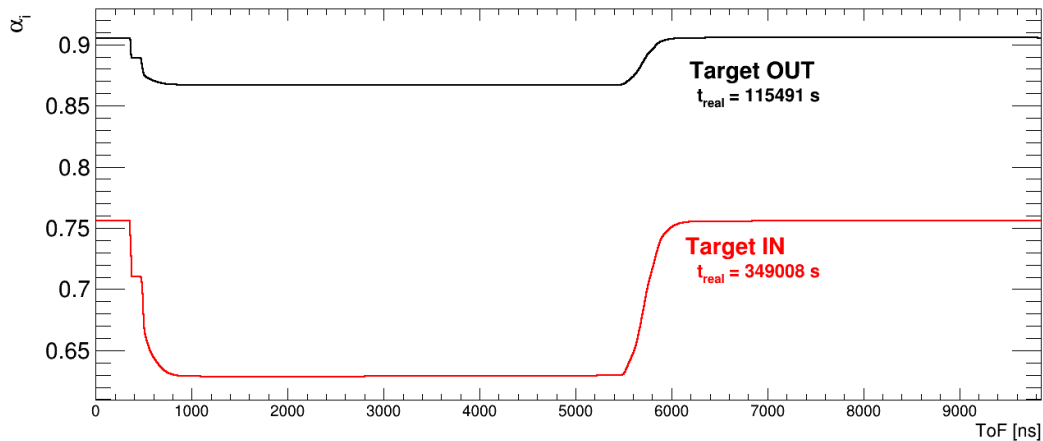$$\alpha_i = \frac{N_{\mathrm{acc}} - N_{\mathrm{block,i}}}{N_{\mathrm{acc}}} \tag{4.8}$$

Figure 4.5.: The ToF channel dependent dead time correction factor α_i is shown and is in compliance with average livetime of 71% "target" in and 89% "target out" - calculated from the electronic Logbook. On the x-axis the uncalibrated relative ToF is used.

In fig. 4.5 α_i of every ToF channel is shown for "target in´´ and "target out´´ data. Lower α_i means higher rate of blocked events, because the DAQ was more busy, as it is obvious for "target in´´ measurements. A calibration of the gamma flash, which corresponds to the falling edge, is not made, which results in the (stepped) shape from a merging of different TDC offsets of every detector. That's why the relative ToF was used in the analysis. The rising edge around

5500 ns results from the end of each dead time ($t_{\mathrm{dead,event}} \approx 15\,\mu$s), which blocks also most of the following accelerator period.

4.4.2. γ-Ray Energy to Neutron Energy Correlation

The main part of the analysis is the measurement of the γ-ray-spectra as a function of time-of-flight. In fig. 4.6 typical γ-ray spectra of a LaBr$_3$ scintillator and a HPGe detector are shown.
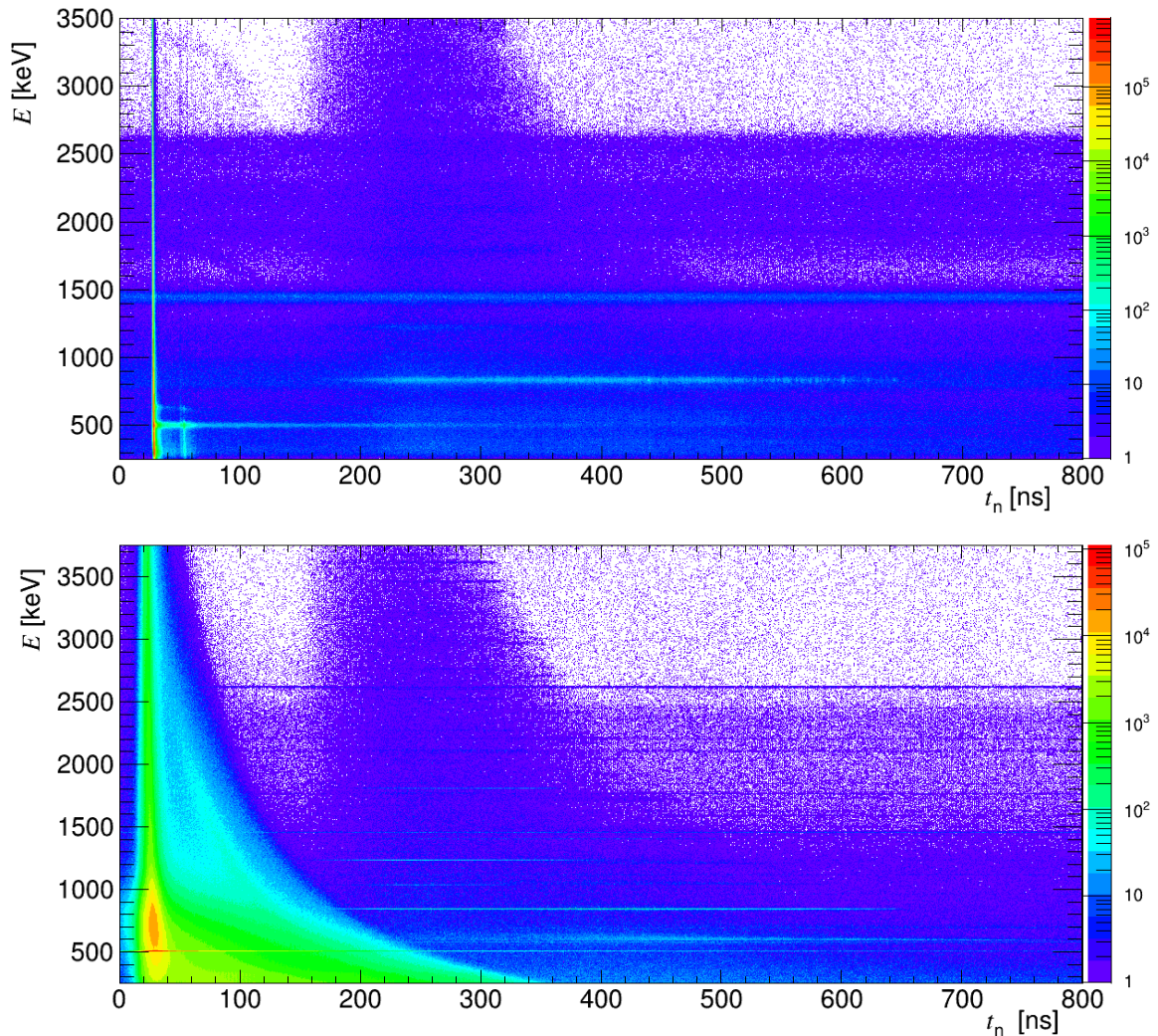

Figure 4.6.: 2D-spectra demonstrate the relation between detected γ-ray energy and neutron ToF/energy. The upper panel shows the spectrum from LaBr$_3$ and the lower panel one from HPGe - both under an angle of 55°.

First of all, the advantages of both detectors type are obvious. The LaBr$_3$ gives an excellent time resolution, which results in a sharp vertical ridge around 28 ns, the γ-flash. This corresponds to events triggered by the bremsstrahlung from the electron beam hitting the photo-neutron source. The backscattering of bremsstrahlung from the beam dump forms the "after pulse" at $t_n \approx 55$ ns. Horizontal ridges in the range of about 170 ns and 650 ns correspond to γ-rays from inelastic scattering of neutrons from the target. Horizontal ridges uncorrelated with time-of-flight are caused by background or intrinsic radioactivity, in particular the ^{40}K decay or ^{138}La electron capture in the lanthanum bromide. Besides the limited γ-ray energy resolution, the intrinsic background is a downside of the LaBr$_3$.

With higher energy resolution of the HPGe detector, more γ-ray lines from inelastic scattering are identifiable and the detector has no intrinsic background. The disadvantage is a worse time resolution, which broadens the gamma flash in a tremendous way.

Although the data are accumulated in histograms, the event information of the correlation between γ-ray and neutron energy is still available. To investigate that, windows are set on the ToF and therefore on the incident neutron energy. Interested in inelastic scattering on ^{56}Fe, neutrons from around 800 keV until 12500 keV are taken into account, which means ToF-gate from 671 to 171 ns. From 3D-spectra the γ-ray spectra are projected to determine the γ-ray intensity based on certain ToF or rather E_n window. In that way, the correlation will be analysed for a 10 ns ToF-binning of the HPGe, and a $1 - 2$ ns binning for LaBr$_3$ data. In the following, the center neutron energy with its resolution will always be indicated for spectra and angular distribution data.

4.4.3. γ-Ray Spectra and Peak Fitting

The typical γ-ray spectra from both detector types are shown in fig. 4.7. One can differentiate between γ-rays from excited state of iron and intrinsic or ambient radioactive decays. Especially in the HPGe spectra, many important detectable γ-ray energies are marked and most of them can be connected with exited states of ^{56}Fe (see level scheme in fig. 2.2). Focusing on the first transition, the spectra of all neutron induced events are analysed to sample the photopeak. The 847 keV-peak is fitted with a Gaussian peak (area, mean and width) and a linear background (offset p_0 and slope p_1) in a narrow window around the peak region. Because the analysis is done with the original QDC/ADC-spectra, they are also shown here.
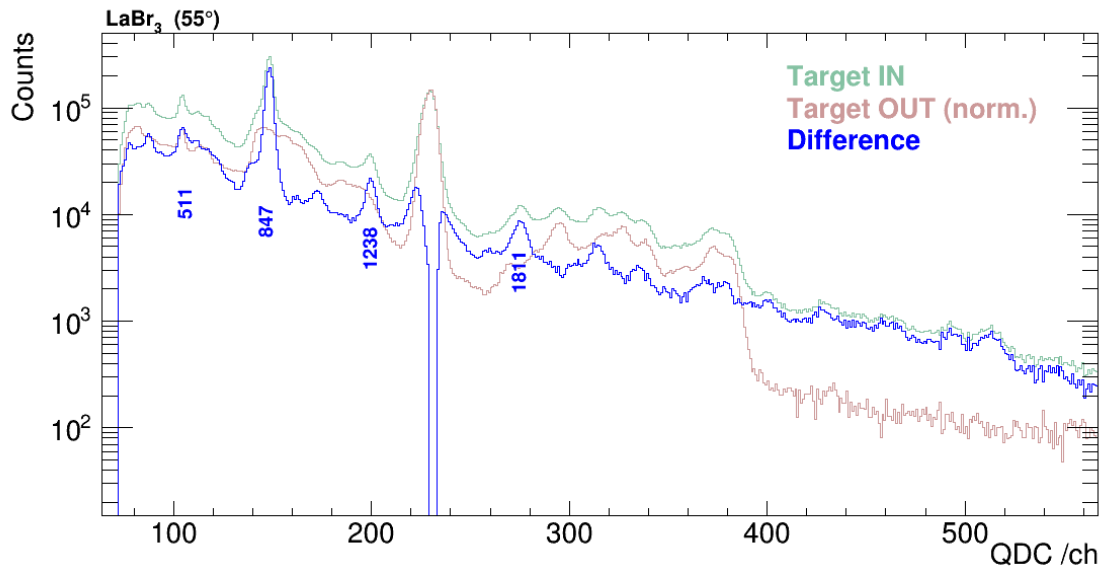
(a) QDC-spectra of the LaBr$_3$ detector under 55°. The first three exited states from ^{56}Fe are observable with adequate energy resolution. The background subtraction seems to overestimate the background in the 1460 keV region. This might be attributed to a small change in the effective energy resolution in the "target in" and "target out" measurements.
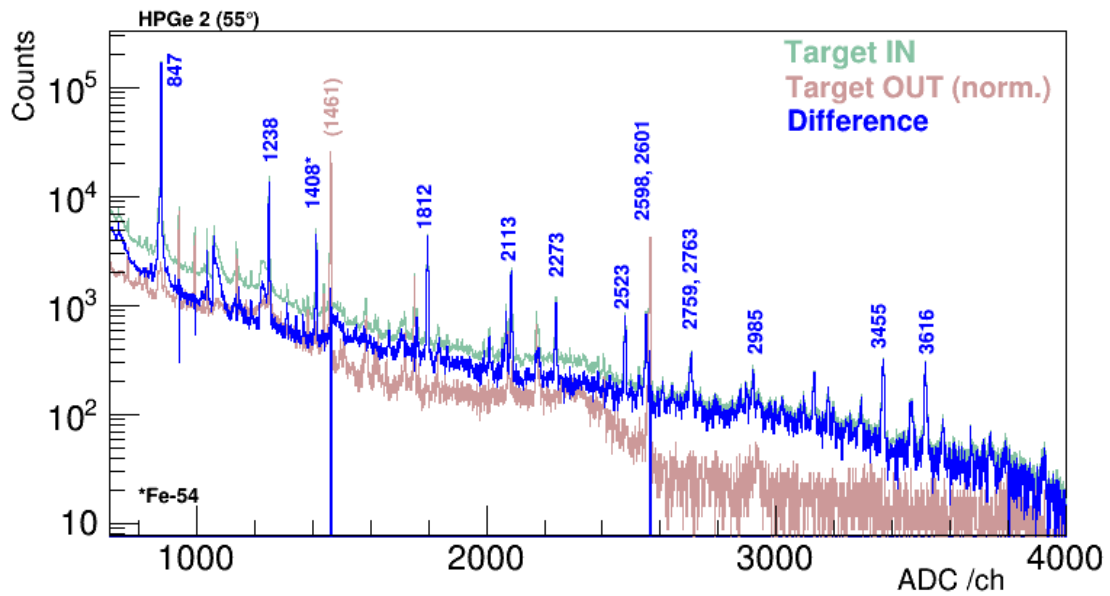
(b) ADC-spectra of HPGe under 55°

Figure 4.7.: For mostly all neutrons from 800 to 12500 keV, the accumulated γ-ray spectra are shown for both detector types exemplary.

Table 4.7.: Mean value and width (1σ) of Gaussian fitted $847\,\text{keV}$-peak for each detector.

HPGe	30°	55°	90°	125°	150°
mean [ch]	878.5	877.0	881.7	874.6	871.2
width [ch]	1.55	1.34	1.42	1.67	1.76

LaBr$_3$	30°	55°	90°	125°	150°
mean [ch]	159.5	148.3	150.7	163.9	172.3
width [ch]	2.13	1.92	2.20	2.19	2.17
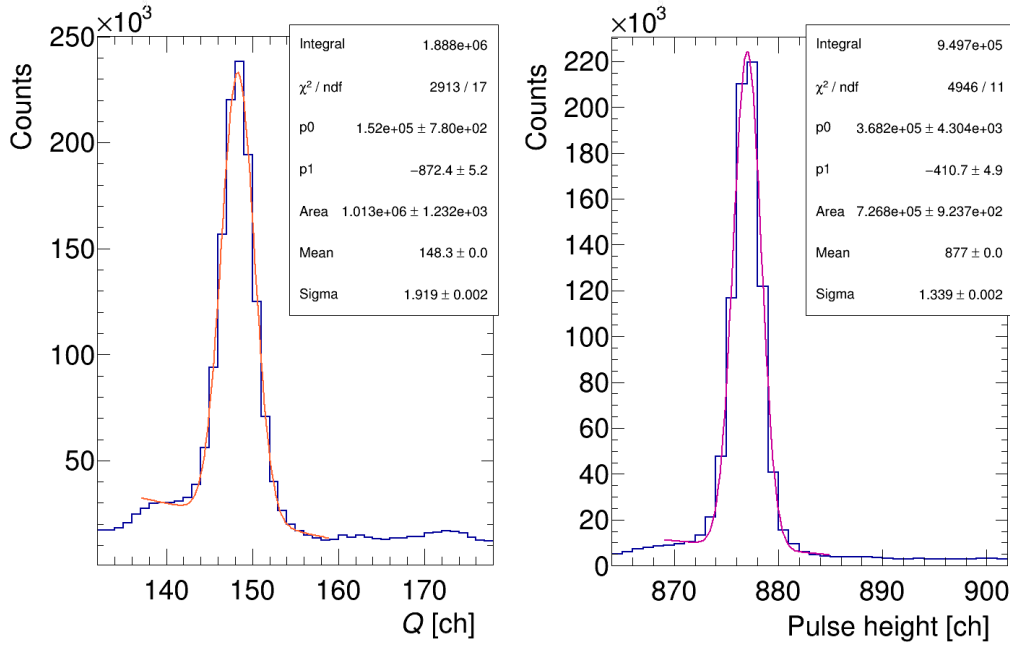
Figure 4.8.: The γ-ray peak of $847\,\text{keV}$ is fitted with full counting statistics of mostly all neutron energy from 800 to $12500\,\text{keV}$. Left panel: LaBr$_3$ detector (55°). Right panel HPGe detector (55°).

Peak Determination at Low Counting Statistics

With increasing neutron energy above $1-2\,\text{MeV}$, the neutron flux decreases and the γ-rays from inelastic scattering are registered with lower counting statistics. Also near threshold of inelastic scattering and for the 90°-detector, the peak areas are determined with highest uncertainties due to low yield. In order for the fitting routine to converge, the width of the Gaussian is fixed to the respective value determined with high counting statistics (see fig. 4.8 and tab. 4.7).
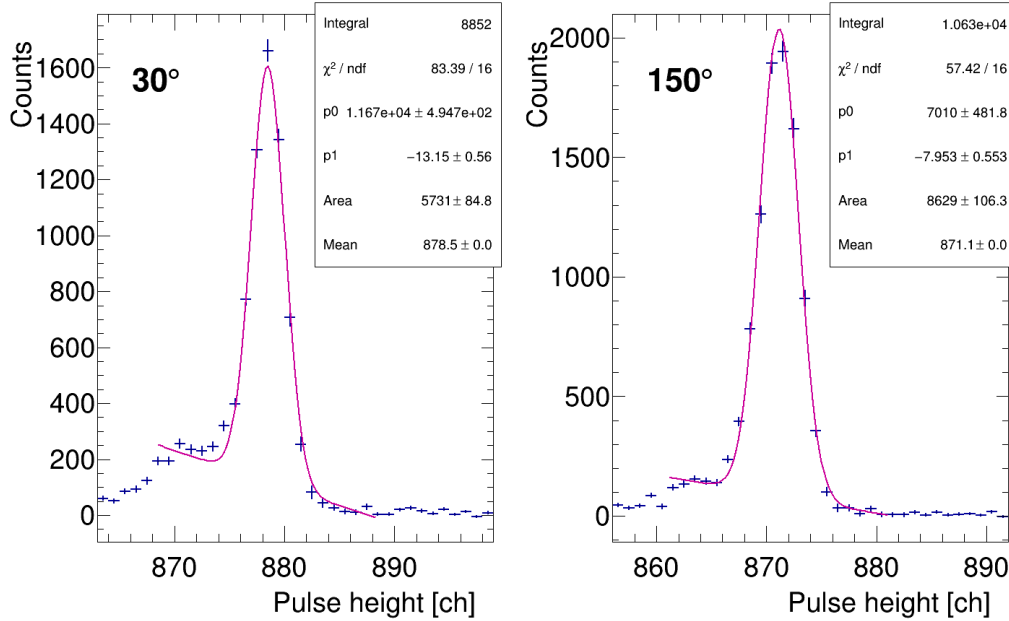
Figure 4.9.: HPGe spectra with fitted γ-ray peak of 847 keV in 10 ns binning is shown. A window on neutron ToF is set from 573 to 583 ns, which complies to $E_n = 982 \pm 16$ keV. The neutron induzed background at 834 keV from scattering on Germanium crystal is discussed.

In the analysis of HPGe spectra, an interesting angle dependent effect was observed. The background under the 847 keV peak contains an additional peak. Neutrons, mostly elastically scattered from the target, undergo an inelastic scattering reaction in the Ge crystal. From the ^{72}Ge$(n, n'\gamma)$ reaction γ-rays with an energy of 834 keV are emitted. There is a high efficiency to detect these reactions as they occur inside the detector. For this reason, the recoiling ^{72}Ge nucleus adds energy to the photopeak of the γ-ray. Due to the angular dependence of the scattering cross section, the 834 keV plus recoil energy form a triangular shape - typical for neutron interactions on HPGe detectors. A more detailed description of neutron induzed background in Germanium detector is found in [FMP96].

In fig. 4.9 HPGe spectra are shown from for- and backward angles. Although the efficiency of the 30° detector is lower, looking at the main peak, there are almost 300 counts per channel in the Ge-background peak. Compared to 150° with ≈ 150 counts per channel, this background phenomenon is lower under backscattered angle, which confirms its origin from elastic scattered neutrons. Unfortunately, this effect was not studied using another target, for example Nickel, which has similiar cross section and was used by Negret et al. at IRMM, whose spectra is attached (fig. A.4). They did not see a major influence on the background, but measured only under angles of 110° and 150°.

To improve fitting of the background, the range is adjusted so that its left side handles the peak and a broad triangle shape is assumed. The dependency of the triangle shape on neutron energy is not covered by this routine and could be one possible explanation for some remaining irregular occuring asymmetries.
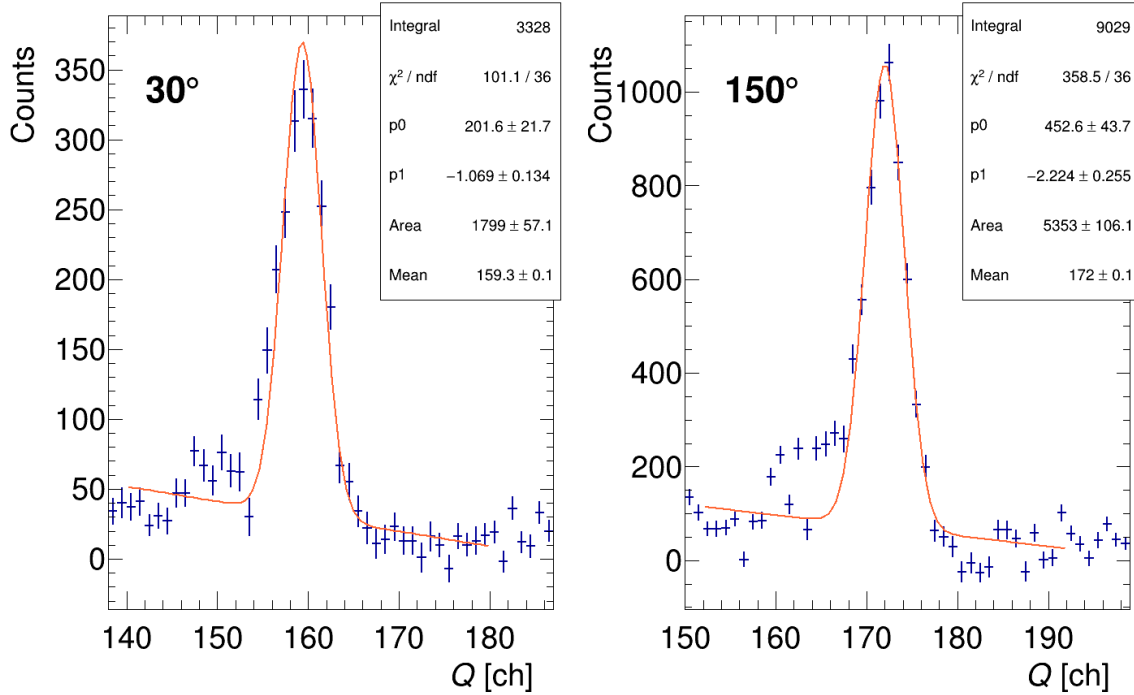

Figure 4.10.: LaBr$_3$ spectra with fitted γ-ray peak of 847 keV in 2 ns binning is shown. A window on neutron ToF is set from 527 to 529 ns, which corresponds to $E_n = 1166 \pm 4$ keV. The fluctuations are caused by spectra subtraction of "target in" and "target out" plus the high intrinsic background of the lanthanum bromide.

For LaBr$_3$, the fixed Gaussian width and a broader linear background handled the sometimes fluctuating data from subtraction (see fig. 4.10). The "target out" substraction is needed due to the instrinsic background, but results in higher statistical uncertainties. However, a similiar systematic angle dependency could not be found. A possible inelastic neutron scattering on aluminium would emit a γ-ray at 843 keV, but the shells of the detectors are too thin and it is not observed in "target out" runs.

To better determine the neutron induced background, especially from target scattered events a measurement with a Nickel or other sample is higly recommended for future experiments with this setup.

4.5. Simulated Correction for Detection Efficiency and γ-Ray Self-Absorption

Simulation is an important tool in modern physics, especially for experiments in the field of high energy physics, but also in neutron-related ones. Knowing all the physical parameters of an involved particle in the simulation at everytime results in the possibility to study physical processes, which are not directly accessible in the experiment, but observable in their influence on the outcome in the end. Due to the big variety of physical parameters and understandings numerical methods are used very often in modern times and in particular so called Monte-Carlo-Simulations. Every simulation is of course based on the assumption of the current unterstanding of the physical interaction and transportion processes or rather the implimantation of these in the corresponding simulation libraries. Most programmes used are MCNP, FLUKA and GEANT4. The following results were obtained with simulations based on GEANT4.

Two systematic effects in the measurement of the γ-ray angular distribution were observed and needed correction, which werde done by simulations:

Due to the target dimensions it has to be considered as an extended source. The photopeak efficiency determination is based on measurements with calibrated point sources, see sec. 4.1. Therefore, a correction factor (sec. 4.5.3) was calculated using GEANT4 for the ratio of the efficiency for an extended source and point source:

$$\epsilon = \left(\frac{\epsilon_{\text{extended}}}{\epsilon_{\text{point}}} \right)_{\text{GEANT4}} \cdot \epsilon_{\text{point,measured}} = c_{\text{ext},\theta} \cdot \epsilon_{\text{point,measured}}. \tag{4.9}$$

Another effect due to the extended target dimensions is the absorption of the γ-rays from inelastic neutron scattering inside the target. As the different detectors view the target under different angles, the path lengths inside the target of the the γ-rays hitting the detector are different, too. This interesting effect has been illustrated in fig. 4.11, where the γ-ray intensity is shown, only with the point source efficiency correction:

In LaBr$_3$, the 55°-data is clearly higher than the 125° one. The opposite effect is seen in HPGe, where also 150° have more counts than 30°. To some extend, these two are more or less the same in LaBr$_3$. This mirrored effect can be explained with the twisted target angle of $\theta_t = 109.5°$. Some detectors see almost the side surface of the cylindrical target and γ-rays have a longer way inside the target with higher possiblity of scatter and absorption effects.

4.5.1. Simulated Setup of Experiment

A simulation will always be a re-construction of the experiment with some simplifications. In this case, sensitive volumes of the detector are used in addition to an aluminium housing, but without the amplifying electronics. According to information from the manufacturer (Ortec, Canberra, Saint-Gobain Crystals), the main dimensions are listed in table 4.8, which were implemented in the geometric file of the GEANT4-simulation.

Table 4.8.: The dimensions of the simulated setup are shown.The distance between the front of the detector and the target center is 300 mm and the target dimensions are 79 mm diameter and 4.5 mm thickness.

For consistency, a comparison is made from the geometric correction simulation(sec. 4.5.3) to an analytic point source calculation with 10^9 Geantinos, which is the initial condition in the simluation, too.

The names of Canberra (CB) detectors are $EGC100-250-SEG4$ $N° \cdots$.

LaBr$_3$	30°	55°	90°	125°	150°
name	SN 1631	SN 923	SN 2820	SN 2821	SN 2822
size	$2'' \cdot 2''$	$3'' \cdot 3''$	$3'' \cdot 3''$	$3'' \cdot 3''$	$3'' \cdot 3''$
r_{scin} [mm]	25.4	38.1	38.1	38.1	38.1
t_{alu} [mm]	0.5	0.5	0.5	0.5	0.5
end cap gap [mm]	2.0	2.0	2.0	2.0	2.0
$r_{Al-housing}$ [mm]	28.75	41.25	41.25	41.25	41.25
a [mm]	302.5	302.5	302.5	302.5	302.5
Ω	0.02203	0.04925	0.04925	0.04925	0.04925
calc. #	1753346	3919307	3919307	3919307	3919307
det. #	1752097	3917832	3918685	3921828	3918605
diff. [%]	-0.07	-0.04	-0.02	0.06	-0.02

| HPGe	30°	55°	90°	125°	150°
name	$43-N31529A$	$41-N31587A$	$N° 73615$	$41-N31569A$	$N° 73633$
rel. eff.	60% (Ortec)	100% (Ortec)	100% (CB)	100% (Ortec)	100% (CB)
$r_{crystal}$ [mm]	34.15	39.55	38.25	39.1	38.35
$l_{crystal}$ [mm]	76.1	90	86.5	93.1	86.9
r_{inner} [mm]	5.5	5.5	5.5	5.5	5.5
$s_{Ge-hole}$ [mm]	8	8	8	8	8
t_{alu} [mm]	1.0	1.0	1.0	1.0	1.0
end cap gap [mm]	3.0	4.0	6.0	4.0	6.0
a [mm]	304	305	307	305	307
Ω	0.03927	0.05217	0.04821	0.05100	0.04846
#calc.	3125270	4151434	3836237	4058642	3856091
#det.	3126347	4151721	3839117	4058399	3854337
difference [%]	0.03	0.01	0.08	-0.01	-0.05
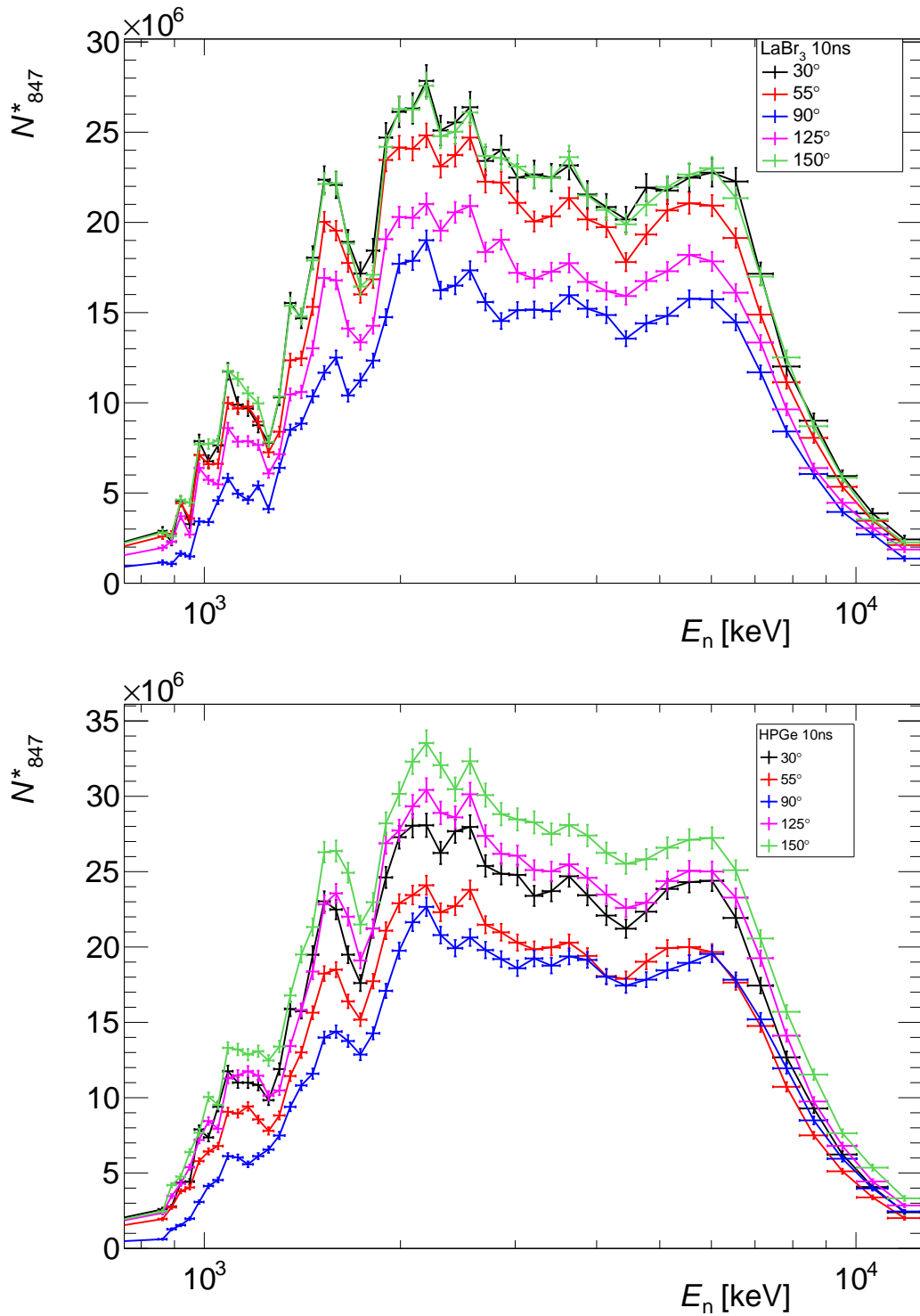
Figure 4.11.: Point source efficiency corrected γ-ray intensities $N^{\star}_{847}$ are shown with an equidistant ToF-binning of 10 ns in neutron energy dependency. A discrepancy is observed for 55° and 125° or rather 30° and 150°, which is switched for both detector types (upper panel: LaBr$_3$; lower panel: HPGe).

4.5.2. Interaction Point of Inelastic Scattering

In addition, the realistic geometry of the target and the detectors, including surrounding materials, the distribution of the interaction points inside the extended iron target, is of importance for the simulation of the extended source. The intensity of neutron inelastic interactions is decreasing because of elastic neutron scattering in the layers of target material before the inelastic scattering occurs. To simulate this effect, a neutron source is located in $1\,\text{m}$ distance from the target with a beam diameter to fully irradiate the target from -z direction. Between the normal of the target and the neutron beam is an angle of $19.5°$ due to the experimental setup. Scatter effects outside the target are not considered. The position at which the inelastic scattering happens is tracked in the simulation by detecting the starting point of the emitted γ-ray.
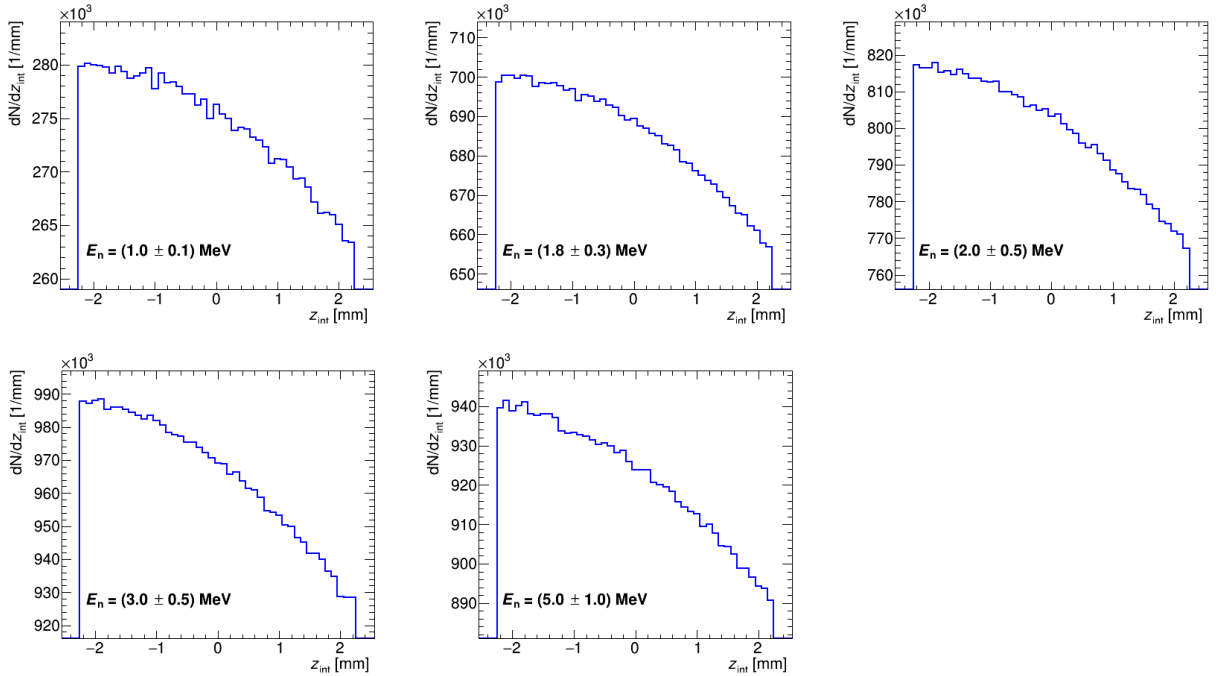
Figure 4.12.: The interaction points of inelastic scattering are simulated for different incident neutron energies. The target is irradiated from -z direction with 10^9 neutrons per simulation.

Simulations are done for different neutron energies of 1 to $5\,\text{MeV}$. To rule out any resonance effects, a uniform distribution over a certain energy resolution is assumed. The results are shown in fig. 4.12. For higher neutron energy, more inelastic scattering events take place because the cross sections are higher and above $2\,\text{MeV}$ more states can be populated. All tested neutron energies show a similiar slope of 5% decrease of the interaction point of inelastic scattering along the z-axis of target. The most likely reason is elastic scattering of neutrons, which is forward peaked (example in fig. 4.13). Nevertheless the 5% decrease is implemented as an

initial conditions to simulate the absorbtion correction of the emitted γ-rays, whose initial positions are non trivial.
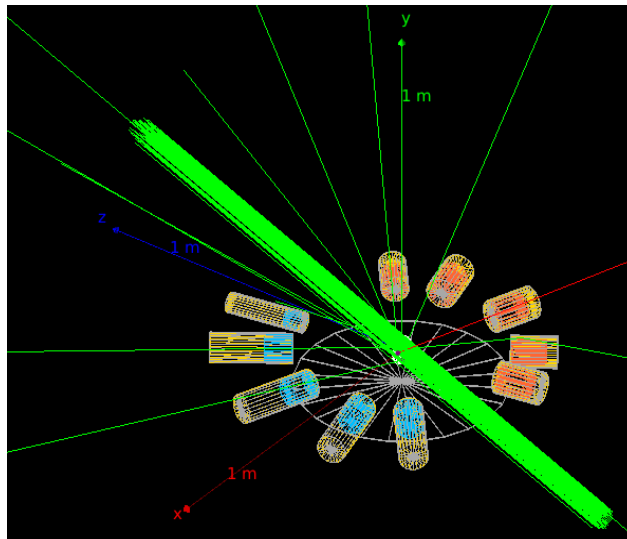
(a)

Figure 4.13.: An example of the GEANT4 simulation shows the setup and the trajectories of 100 started neutrons of $E_n = 1.0 \pm 0.1\,\text{MeV}$ in the lower right corner. Neutrons illustrated in green are mostly elastically scattered forward peaked and one inelastic scattering γ-ray is tracked in red.

4.5.3. Geometric Correction for Extended Source Efficiency

The effective solid angle of the extended source geometry can be simulated in GEANT4 using "*geantinos*" test particles that follow straight trajectories without any interaction and are registered in the sensitive volume of the LaBr$_3$ and HPGe crystals. In table 4.9, the ratio of detected geantinos, either from an extended or point source, are computed (Eq. 4.10). This ratio will be used as a correction factor for an efficiency of an extended target/source. The uncertainties are always standard deviation.

$$c_{\text{ext},\theta} = \left(\frac{\epsilon_{\text{extended}}}{\epsilon_{\text{point}}} \right)_{\text{GEANT4}} = \frac{N_{geantino,extended,\theta}}{N_{geantino,point,\theta}} \tag{4.10}$$

The simulation is tested with an analytic formula for the solid angle of each detector and determined by how many test particles arrive from a point source. Although spherical detector

Table 4.9.: Correction factor $c_{\text{ext},\theta}$ displays the geometric effect of an extended target in comparison to pointlike γ-ray calibration source for each detector.

HPGe	30°	55°	90°	125°	150°
$c_{\text{ext},\theta}$	0.9979	1.0045	1.0028	0.9942	0.9893
$\Delta c_{\text{ext},\theta}$	0.0008	0.0007	0.0007	0.0007	0.0007
LaBr$_3$	30°	55°	90°	125°	150°
$c_{\text{ext},\theta}$	0.9945	0.9943	1.0048	1.0041	0.9989
$\Delta c_{\text{ext},\theta}$	0.0011	0.0007	0.0007	0.0007	0.0007

volumes are used in the simulation, the analytic calculation is comparable for a point source, because only the first interaction counts and so the volume can be reduzed to circular shape. The solid angle Ω_{det} of such a disk shaped detector surface with radius a and point source to detector surface distance d is given by

$$\Omega_{\text{det}} = 2\pi \left(1 - \frac{d}{\sqrt{d^2 + a^2}} \right). \tag{4.11}$$

The comparison between the simulated events (#det.) and the analytic calculated ones(#calc.), shown in tab. 4.8, gives agreement better than one permill, showing that the geantino simulation agrees with the analytical formula in the case of point source geometry.

4.5.4. γ-Ray-Self-Absorption Effect inside the Target

A major effect to correct is the self-absorption of γ-rays, because the mean free path of an 1 MeV γ-ray inside a volume of iron is about 2.12 cm. The basic of the calculation is the Lambert-Beer-law (eq. 4.12), which describes the attentuation of light (γ-rays) depending on the material (Fe), in which it is propagating.

$$\frac{I}{I_0} = \exp[-\mu \cdot \rho_{\text{Fe}} \cdot d] \tag{4.12}$$

$$l = \frac{1}{\mu \rho_{\text{Fe}}} = \frac{1}{\sigma n} \tag{4.13}$$

The ratio $^I/_{I_0}$ is often called transmission T and is determined by the mass attentuation factor μ, the material density ρ_{Fe} and distance/track length d inside the material. Eq. 4.13 gives the connection to cross section σ and number of target particle per unit volume n. Table 4.10 gives an insight into possible attentuations length inside the target. l is the mean free path.
In the simulation, the following ratio c_{abs} (eq. 4.14) is determined by comparing detected γ-rays with initial energy of e.g $E_\gamma = 847$ keV. Therefore, γ-rays are started isotropically from

Table 4.10.: The attentuation inside the iron target is listed for different track lengths. The mass attentuation factor μ is taken from XCOM [BHS$^+$98].

E_γ [keV]	847	1238	1811
μ [cm^2/g]	0.0652	0.0535	0.0451
d [cm]	$I/I_0(847\,\mathrm{keV})$	$I/I_0(1238\,\mathrm{keV})$	$I/I_0(1811\,\mathrm{keV})$
0.01	0.995	0.996	0.996
0.1	0.950	0.959	0.965
0.225	0.891	0.910	0.923
0.5	0.774	0.810	0.837
1	0.598	0.656	0.701
2	0.358	0.431	0.492
3	0.214	0.283	0.345
3.95	0.132	0.190	0.246

Table 4.11.: Correction factor $c_{\mathrm{abs},\theta}(E_\gamma)$ due to γ-ray-self-absorption inside the ^{nat}Fe-target is tabulated for each detector and a γ-ray energy of $E_\gamma = 847\,\mathrm{keV}$. An overview of more $c_{\mathrm{abs},\theta}(E_\gamma)$ for the first three excited state energies is shown in the appendix table A.2.

HPGe	30°	55°	90°	125°	150°
$c_{\mathrm{abs},\theta}(847\,\mathrm{keV})$	1.1862	1.4599	1.3645	1.1497	1.1245
$\Delta c_{\mathrm{abs},\theta}(847\,\mathrm{keV})$	0.0010	0.0011	0.0011	0.0008	0.0008

LaBr$_3$	30°	55°	90°	125°	150°
$c_{\mathrm{abs},\theta}(847\,\mathrm{keV})$	1.1246	1.1514	1.3660	1.4577	1.1861
$\Delta c_{\mathrm{abs},\theta}(847\,\mathrm{keV})$	0.0012	0.0009	0.0011	0.0012	0.0009

the extended target with a 5% decrease discussed in sec. 4.5.2 in a vacuum or an iron filled target volume. This energy dependent factor will correct the γ-rays from inelastic scattering, which are absorbed or scattered inside the target. The result for $E_\gamma = 847\,\mathrm{keV}$ can be found in table 4.11.

$$c_{\mathrm{abs},\theta}(E_\gamma) = \frac{N_{\mathrm{vacuum},\theta}}{N_{\mathrm{Fe},\theta}} \tag{4.14}$$

4.6. High-Resolution γ-Ray Intensity Data

The two previous discussed correction factors are implemented in the analysis of the γ-ray intensity in the following way:

$$N_\theta^\aleph(E_\gamma, \Delta E_\mathrm{n}) = \frac{c_{\mathrm{abs},\theta}(E_\gamma) \cdot N_\theta(E_\gamma, \Delta E_\mathrm{n})}{c_{\mathrm{ext},\theta} \cdot \epsilon_{\mathrm{point},\theta}(E_\gamma)} \tag{4.15}$$

The γ-ray intensity is calculated from its peak area in the fitted gamma spectra with all corrections from simulation for γ-ray-self-absorption $c_{\mathrm{abs},\theta}$ and the extended source efficiency calibration $(c_{\mathrm{ext},\theta} \cdot \epsilon_{\mathrm{point},\theta}(E_\gamma))$ and it is always correlated with a certain neutron energy resolution. With a fine binning of 1 ns of the LaBr$_3$, the counting stastistic is high enough for all peak fit to converge (see fig. 4.14). To reduce statistical uncertainties below 5 % a 2 ns binning was applied for the final analysis of the γ-ray angular distribution. Therefore, γ-ray intensity in the 2 ns binning is shown in fig. 4.15, where interesting resonance structures, which will be further investigated in sec. 5, are also seen, although a portion of energy resolution is forfeited. The blue curve of the 90°-detector shows the lowest intensity and weaker amplitudes at resonance structures. This effect is due to the anisotropy in the angular distribution.

The measured γ-ray intensities can be compared with measured integrated scattering cross section from [NBD$^+$14] by scaling the cross section. One sees in fig. 4.14 for the 1 ns binning that the resonant structures in the cross section are at the same energies. This indicates also a good agreement in the time-of-flight and therefore neutron energy calibration. The measured γ-ray angular distribution thus corresponds closely to the inelastic cross section.

The inelastic scattering experiment of Negret et al. [NBD$^+$14] at the GAINS setup used HPGe detectors under backscattering angles of 110° and 150°, as written before. These angles are nodes of the fourth order Legendre polynomial and allow a determination of the total inelastic scattering cross section independent from the angular distribution for multipole order up to three [Bru02]. As a flight path of ≈ 200 m is used, the HPGe detectors are allowed to reach a high energy resolution (ToF resolution of 8 ns for a 1 MeV neutron). But at the same time, no information about the 4$^\mathrm{th}$ order Legendre coefficient can be obtained from that experiment. However, for the presented experiment of this work, fourth order coefficients were determined and their influence will be discussed in the next section.
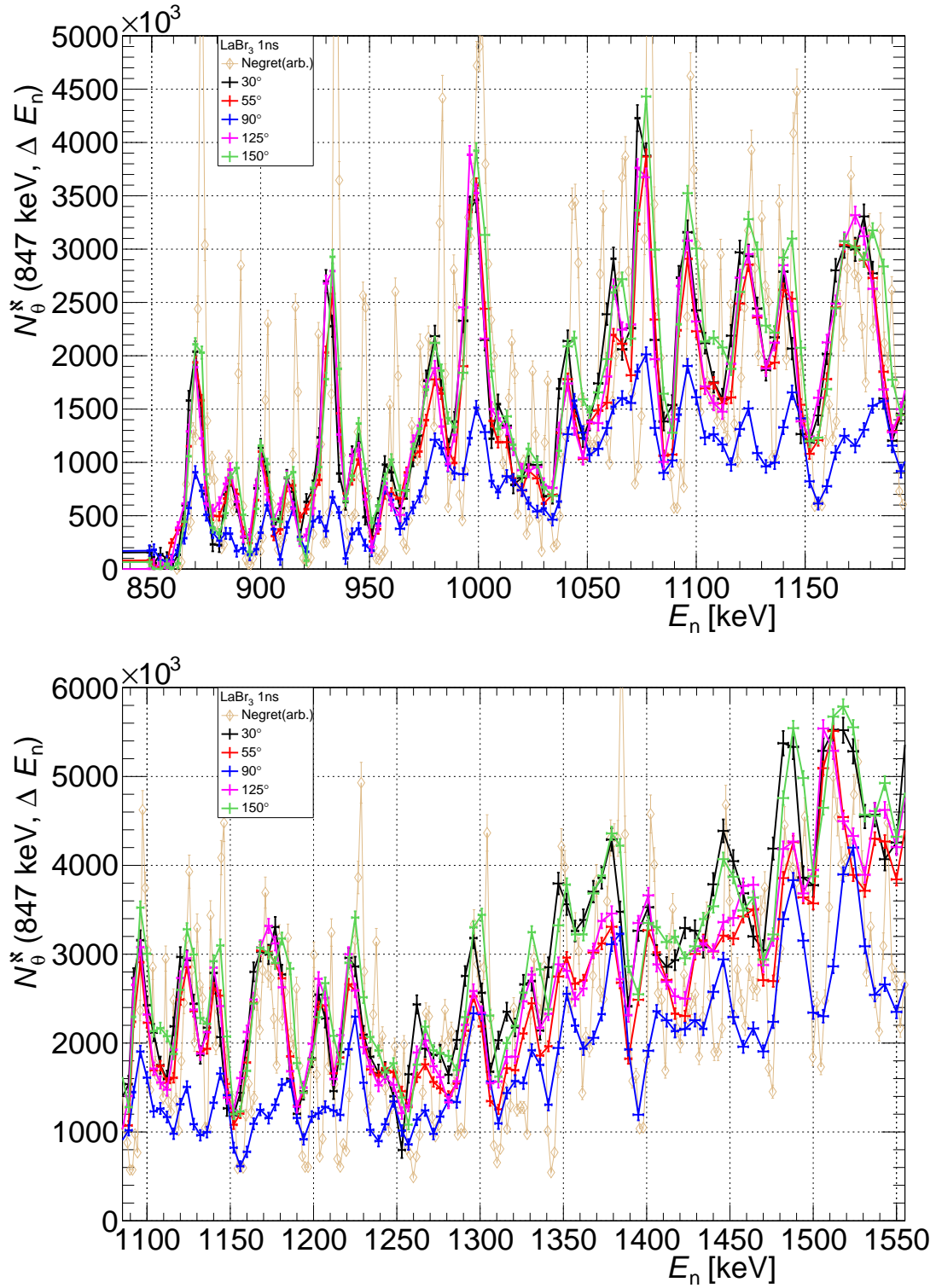
Figure 4.14.: Corrected γ-ray intensities of $1\,\text{ns}$ LaBr$_3$ binning are shown in comparison with a high resolution inelastic scattering cross section from Negret et al. [NBD+14] in arbitary units due to a scaling to cross check the neutron energy calibration.
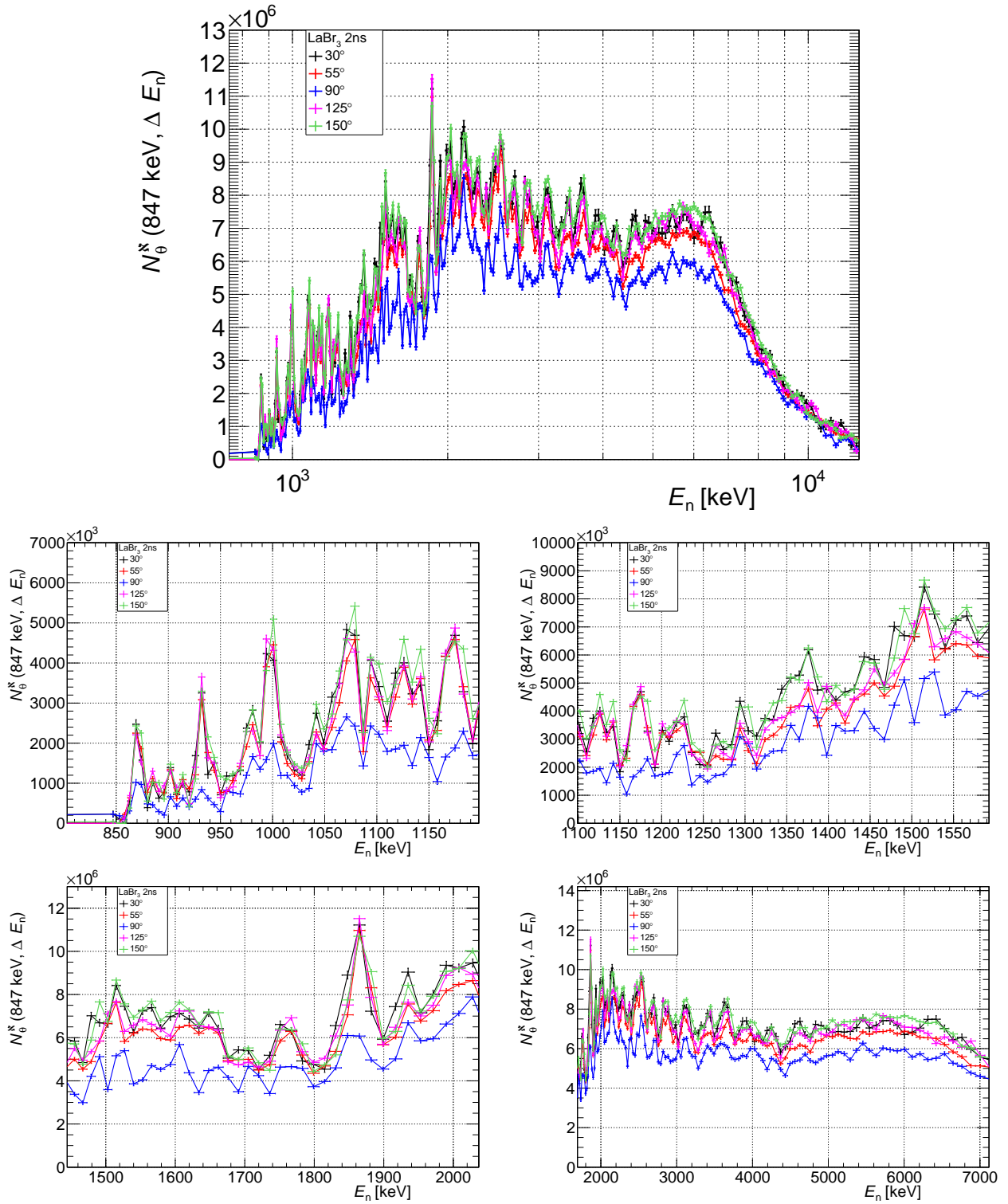
Figure 4.15.: Corrected γ-ray intensities of $2\,\mathrm{ns}$ LaBr$_3$ binning are shown, to determine acceptable uncertainties in angular distribution.

5. Results and Outlook

The normalized angular distribution data points of a certain neutron energy ($\pm$ resolution) are calculated with the following equation 5.1, because it is a relative measurement of intensities, if all detector can see the possible events of the same neutron spectrum at the same time. It is fulfilled by the concurrence of this measurement with the designed setup.

$$\frac{W(\theta)}{W(90°)} = W_{\mathrm{n}}(\theta) = \frac{\sigma_\theta(E_\gamma, \Delta E_{\mathrm{n}})}{\sigma_{90°}(E_\gamma, \Delta E_{\mathrm{n}})} = \frac{N_\theta^{\aleph}(E_\gamma, \Delta E_{\mathrm{n}})}{N_{90°}^{\aleph}(E_\gamma, \Delta E_{\mathrm{n}})}. \tag{5.1}$$

The data for $10\,\mathrm{ns}$ of HPGe and $2\,\mathrm{ns}$ binning of LaBr$_3$ are fitted by a function (eq. 5.2) based on progression of Legendre polynomials divided by the normalization of 90°.

$$W_{\mathrm{n,fit}}(\theta) = \frac{1 + a_2(\Delta E_{\mathrm{n}})P_2(\cos\theta) + a_4(\Delta E_{\mathrm{n}})P_4(\cos\theta)}{1 + a_2(\Delta E_{\mathrm{n}}) \cdot (-0.5) + a_4(\Delta E_{\mathrm{n}}) \cdot 0.375} \tag{5.2}$$

The measured γ-ray angular distributions are compared to the best documented measurement so far from D. L. Smith, 1976 [Smi76]. Fig. 5.1 and 5.2 show a selection of neutron energy range from $930\,\mathrm{keV}$ to $2030\,\mathrm{keV}$.
The comparison shows that the γ-ray angular distribution, although measured at a very similar neutron energy interval, depends strongly on the energy resolution of the measurement. This is due to the resonant structures visible in the inelastic scattering that have a width of $1-5\,\mathrm{keV}$. The new measurements using the LaBr$_3$ scintillation detector have a sufficient time resolution to resolve most of these structures. The resonant structures measured before in the inelastic scattering cross sections are correlated with strongly changes in the γ-ray angular distribution.

At $E_{\mathrm{n}} \approx 930\mathrm{keV}$, the high resolution measurement with the LaBr$_3$ scintillation detectors ($\Delta E_{\mathrm{n}} = \pm 3\,\mathrm{keV}$) shows one of strongest anisotropic distribution. Whereas the measurements using HPGe detectors with a lower resolution ($\Delta E_{\mathrm{n}} = \pm 20\,\mathrm{keV}$) show a smaller anisotropy. It is interesting to note that the HPGe data of this work agree with the measurement of D. L. Smith that had a similar neutron energy resolution.
At $E_{\mathrm{n}} \approx 980\mathrm{keV}$, the opposite effect is observed, when the high resolution measurement of this work ($\Delta E_{\mathrm{n}} = \pm 3\,\mathrm{keV}$) reveals a smaller anisotropy than measurements with a lower resolution ($\Delta E_{\mathrm{n}} = \pm 20\,\mathrm{keV}$). From the γ-ray intensity distribution as a function of neutron energy it can be assumed, that if the resolution is good enough to resolve the resonant structures, the γ-ray
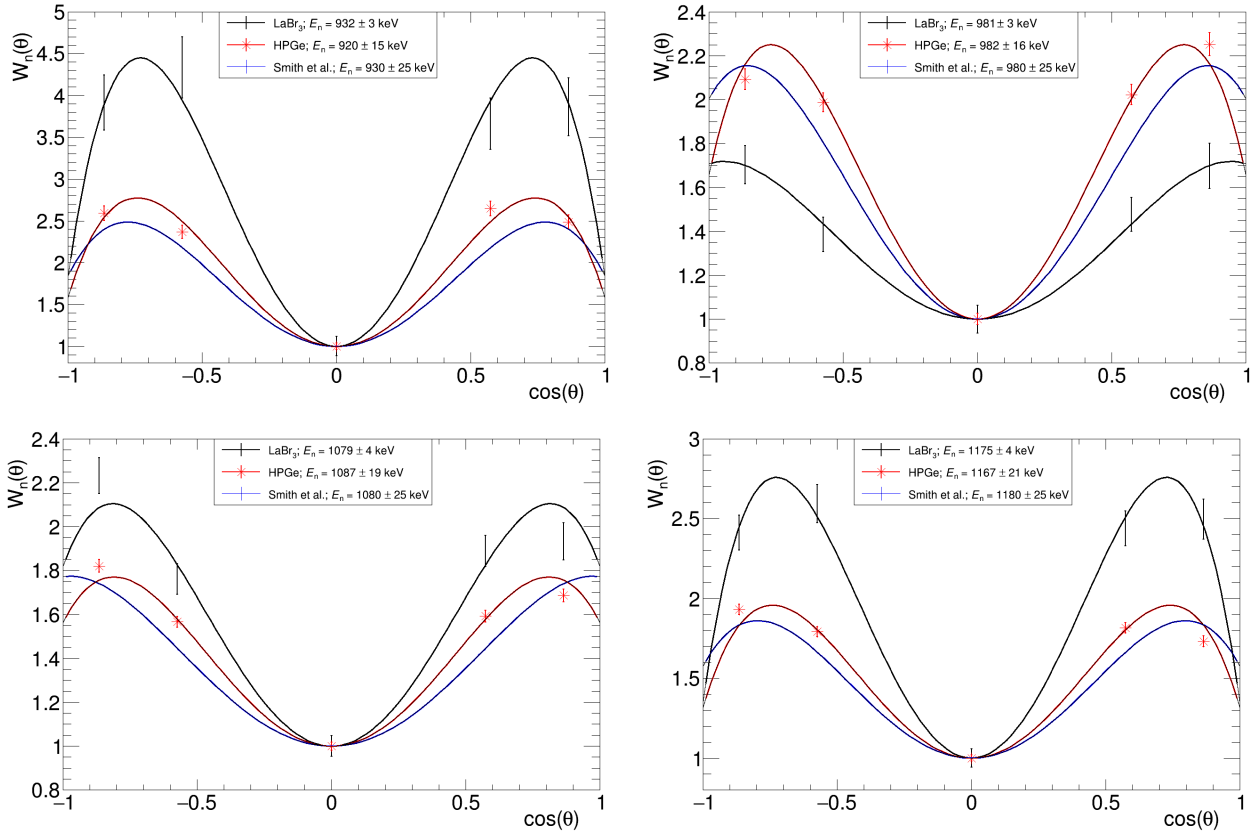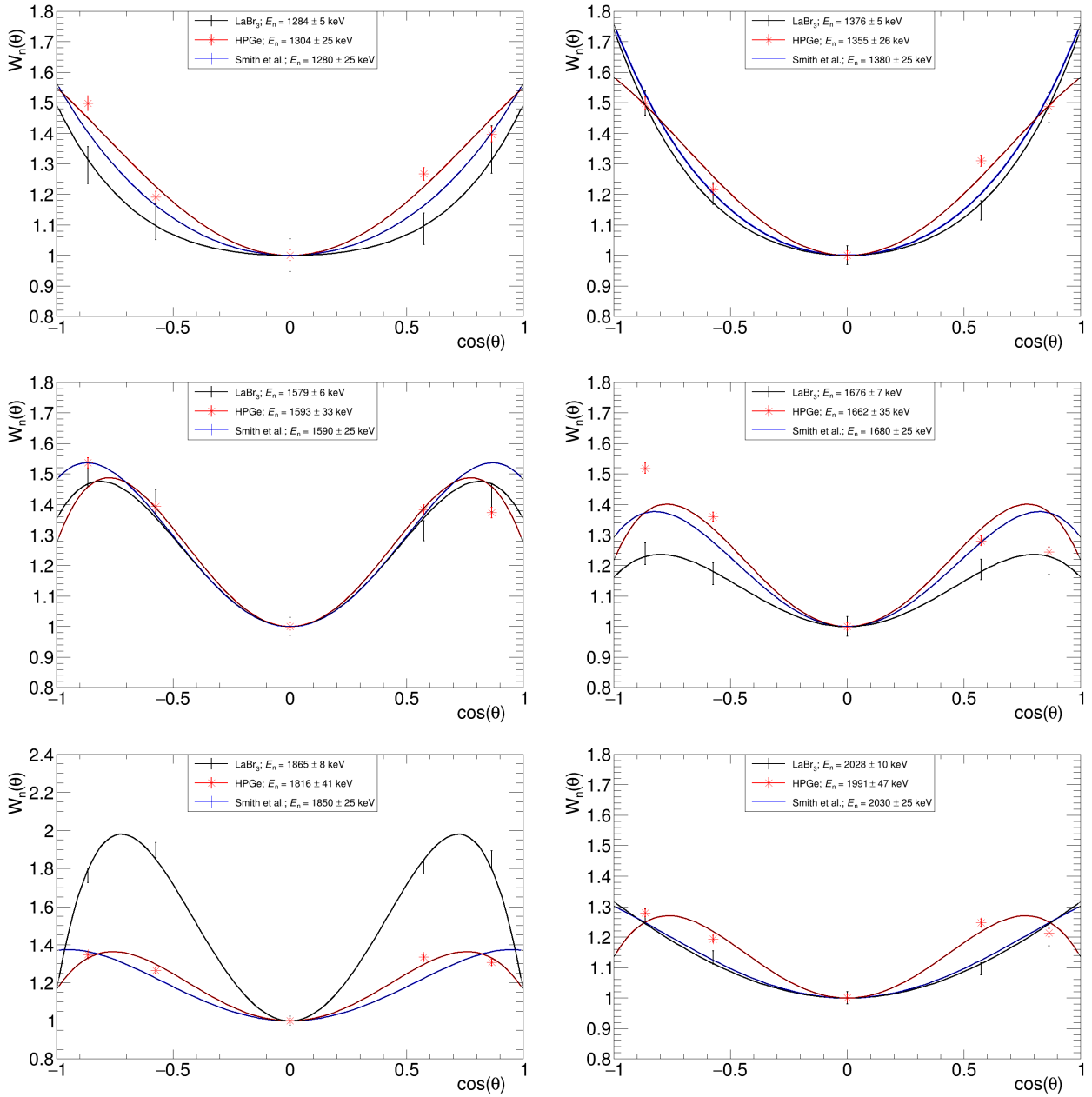
Figure 5.1.: A selection (part I) of γ-ray angular distributions measured in this work with LaBr$_3$ scintillation detectors and HPGe detectors are compared with the measurement of D. L. Smith (1976).

angular distributions fluctuates more strongly as if only the average over several neighbouring resonances were measured. In Comparison to the data by D. L. Smith, this is the case at 930 keV and 1180 keV. D. L. Smith measured positive a_4 values at 1280 keV and 1380 keV, which is confirmed in this work. This phenomenon of $a_4 > 0$ is partly extended until 1500 keV, where Smith did not measure or publish anything. At a higher neutron energy further away from the threshold the resonant structures still exist, but their angular distributions become flatter. At 1865 keV, again, a stronger anisotropy is observed.

Table 5.1 shows the fitted Legendre parameters from this work in comparison with the data from Smith. The fit procedure of Smith was verified. The fitted Legendre parameters for all neutron energy bins from threshold to roughly 2 MeV are shown in fig. 5.3. The threshold of the reaction is $E_\mathrm{n} \approx 862\,\mathrm{keV}$ due to the repulsion on the Fe-nucleus. Near the threshold, the yield is very low, hence the uncertainties of the fitted parameter are quite high, too. The high resolution data results of LaBr$_3$ are listed in the appendix tab. A.3.

Figure 5.2.: A selection (part II) of γ-ray angular distributions measured in this work with LaBr$_3$ scintillation detectors and HPGe detectors are compared with the measurement of D. L. Smith (1976).

E_{n} [keV] $\pm$ ΔE_{n} [keV]	$a_2 \pm \Delta a_2$	$a_4 \pm \Delta a_4$	$W(125°) \pm \Delta W(125°)$
Smith			
930 ± 25	0.521 ± 0.030	-0.511 ± 0.033	1.193 ± 0.013
980 ± 25	0.539 ± 0.013	-0.302 ± 0.014	1.113 ± 0.005
1080 ± 25	0.435 ± 0.017	-0.144 ± 0.019	1.053 ± 0.007
1180 ± 25	0.398 ± 0.039	-0.331 ± 0.044	1.125 ± 0.017
1280 ± 25	0.312 ± 0.031	$0.020 \pm \mathbf{0.040}$	0.990 ± 0.002
1380 ± 25	0.396 ± 0.018	0.039 ± 0.020	0.982 ± 0.008
1590 ± 25	0.319 ± 0.022	-0.167 ± 0.025	1.062 ± 0.010
1680 ± 25	0.226 ± 0.012	-0.155 ± 0.015	1.058 ± 0.006
1850 ± 25	0.245 ± 0.031	-0.089 ± 0.036	1.033 ± 0.014
2030 ± 25	0.190 ± 0.018	-0.023 ± 0.021	1.008 ± 0.008
HPGe 10 ns			
920 ± 15	0.480 ± 0.036	-0.679 ± 0.050	1.258 ± 0.019
982 ± 16	0.459 ± 0.024	-0.481 ± 0.033	1.182 ± 0.013
1050 ± 18	0.420 ± 0.020	-0.230 ± 0.027	1.086 ± 0.010
1167 ± 21	0.336 ± 0.018	-0.473 ± 0.025	1.180 ± 0.010
1304 ± 25	0.319 ± 0.016	-0.038 ± 0.021	1.012 ± 0.008
1355 ± 26	0.338 ± 0.014	-0.056 ± 0.019	1.019 ± 0.007
1593 ± 33	0.244 ± 0.011	-0.243 ± 0.015	1.092 ± 0.006
1662 ± 35	0.206 ± 0.011	-0.211 ± 0.015	1.080 ± 0.006
1816 ± 41	0.178 ± 0.011	-0.209 ± 0.015	1.079 ± 0.006
1991 ± 47	0.144 ± 0.009	-0.156 ± 0.013	1.059 ± 0.005
LaBr$_3$ 2 ns			
932 ± 3	0.591 ± 0.098	-0.956 ± 0.135	1.364 ± 0.052
981 ± 3	0.411 ± 0.056	-0.152 ± 0.075	1.056 ± 0.029
1079 ± 4	0.488 ± 0.042	-0.357 ± 0.056	1.135 ± 0.022
1175 ± 4	0.427 ± 0.050	-0.737 ± 0.069	1.281 ± 0.027
1284 ± 5	0.268 ± 0.049	0.061 ± 0.065	0.975 ± 0.025
1376 ± 5	0.384 ± 0.029	0.062 ± 0.038	0.974 ± 0.015
1593 ± 7	0.337 ± 0.026	-0.055 ± 0.035	1.019 ± 0.013
1691 ± 7	0.256 ± 0.032	-0.237 ± 0.044	1.090 ± 0.017
1865 ± 8	0.292 ± 0.022	-0.537 ± 0.030	1.205 ± 0.011
2028 ± 10	0.193 ± 0.019	-0.008 ± 0.025	1.002 ± 0.010

Table 5.1.: Incident neutron energy, fitted parameter a_2 and a_4 and anisotropy correction factor $W(125°)$ are listed for the plotted angular distribution in fig. 5.1 and 5.2. By verified the fit parameter of Smith, one discrepancy was found for $E_{\mathrm{n}} = 1280$ keV with an uncertainty of a_4 of 0.040 instead of 0.004, which is set in bold.
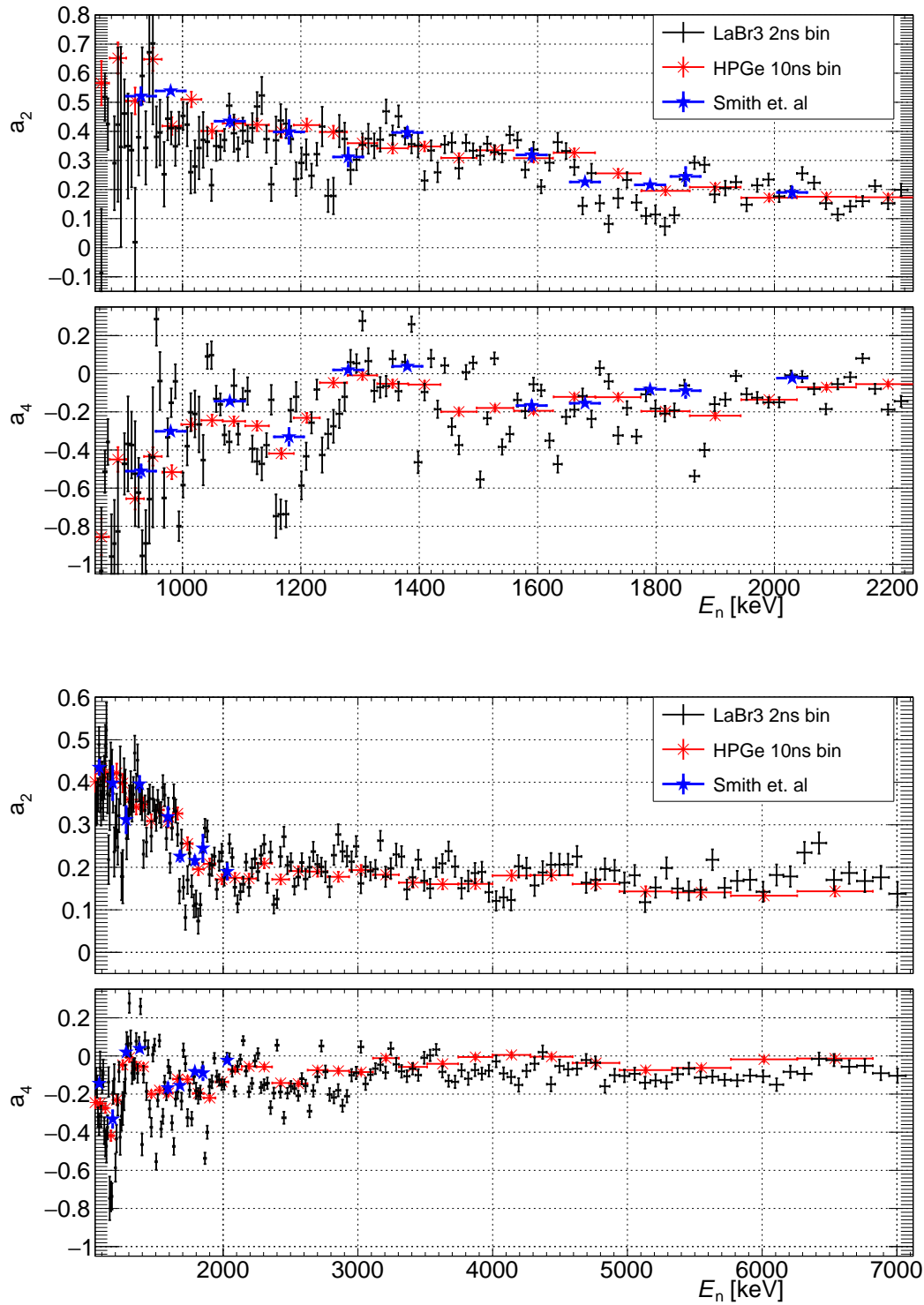
Figure 5.3.: Comparison of fit parameters a_2 and a_4 for neutron energy from threshold up to 2.2 MeV or 7 MeV shows its devolution and flattening of the γ-ray-angular distribution at higher neutron energies.

Anisotropy Factor

An important result and contribution is the calculation of a correction factor for cross section measurements as it was done in the previous experiment published in [BSH+14]. At first, the results show clearly that there is no isotropy, except the region of 1280 keV to 1400 keV, and also an angular distribution correction factor has to be neutron energy dependent. If the experiment is done with one detector set up under 125° and total cross sections are aimed, the correction factor can be derived from eq. 2.4:

$$\sigma_{\text{tot}} = \frac{d\sigma}{d\Omega}(125°) \cdot \frac{4\pi}{W(125°)} \qquad \text{with} \tag{5.3}$$

$$W(\theta) = 1 + a_2(E_n)P_2(\cos(125°)) + a_4(E_n)P_4(\cos(125°)) \tag{5.4}$$
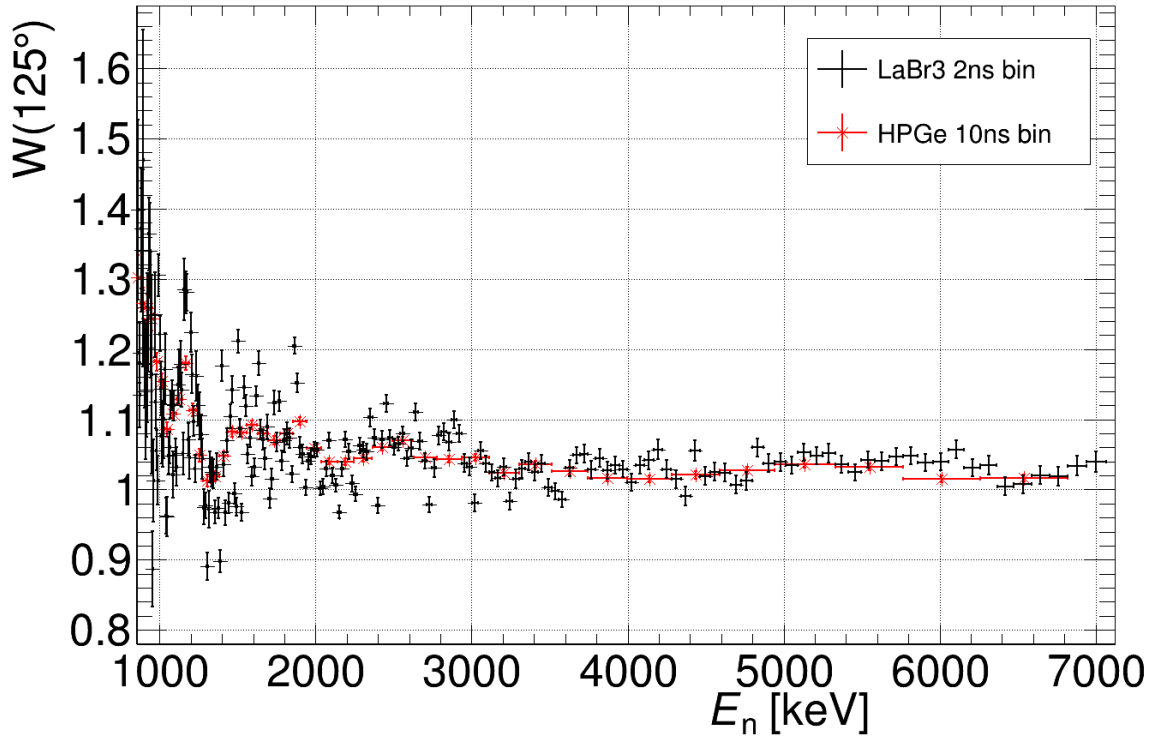
Figure 5.4.: Comparison of anisotropy factor $W(125°)$ for neutron energy over a wide MeV range.

Although the detector covers a certain opening angle, only the single angle of 125° is considered for the calculation. With $P_2(\cos(125°)) = -0.006515$ and $P_4(\cos(125°)) = -0.385187$, the influence of a_4 will be significant. In table 5.1 and A.3 the factor $W(125°)$ is shown with

majority of data above 1, because of negativity of a_4. A comparison of the anisotropy of the results can be found in fig. 5.4 and 5.5.
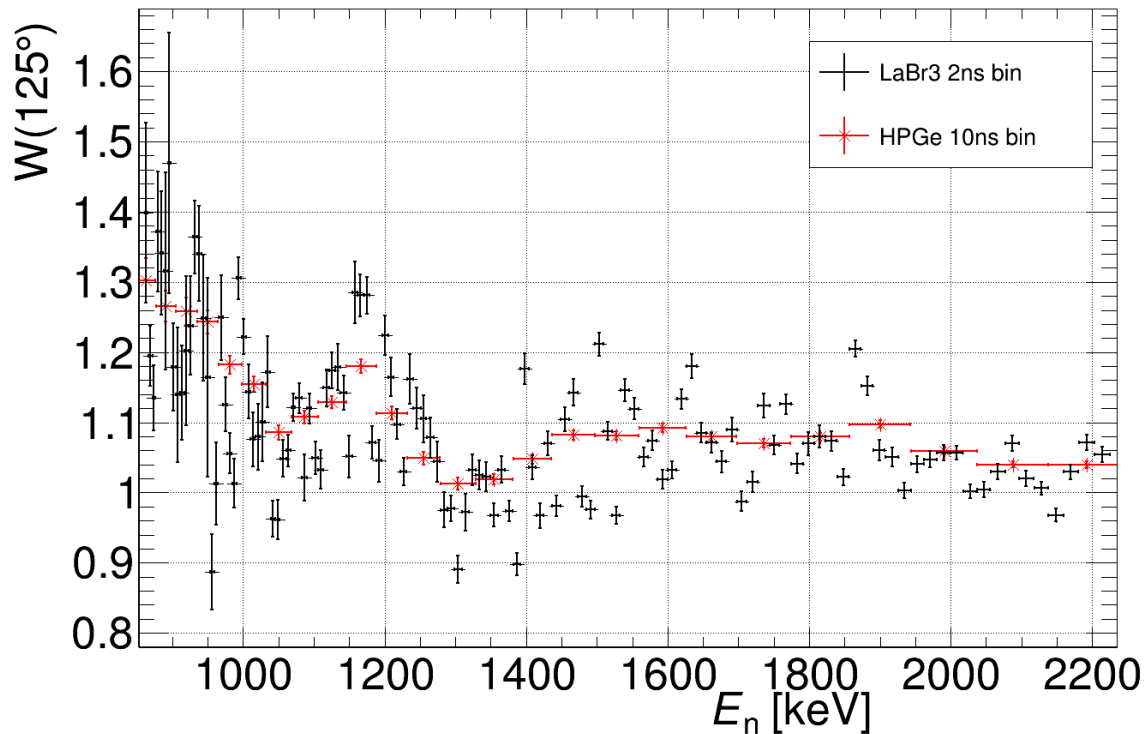
Figure 5.5.: Comparison of anisotropy factor $W(125°)$ for neutron energy from threshold up to 2.2 MeV.

Further Investigation on Resonant Structures

In the following paragraph the most prominent resonant structures from fig. 4.15 are further investigated, especially compared to close-by energies. Interestingly, Smith somehow focused his energies near these resonant structures, but his resolution was not high enough to resolve them. He presumably intended a higher yield and acceptable acquisition times.

From changing angular distributions, one can extract how broad the resonance could be, if the anisotropy changes very rapidly or more slowly, which probably correspond maybe with an overlapping of some resonances very close to each other.
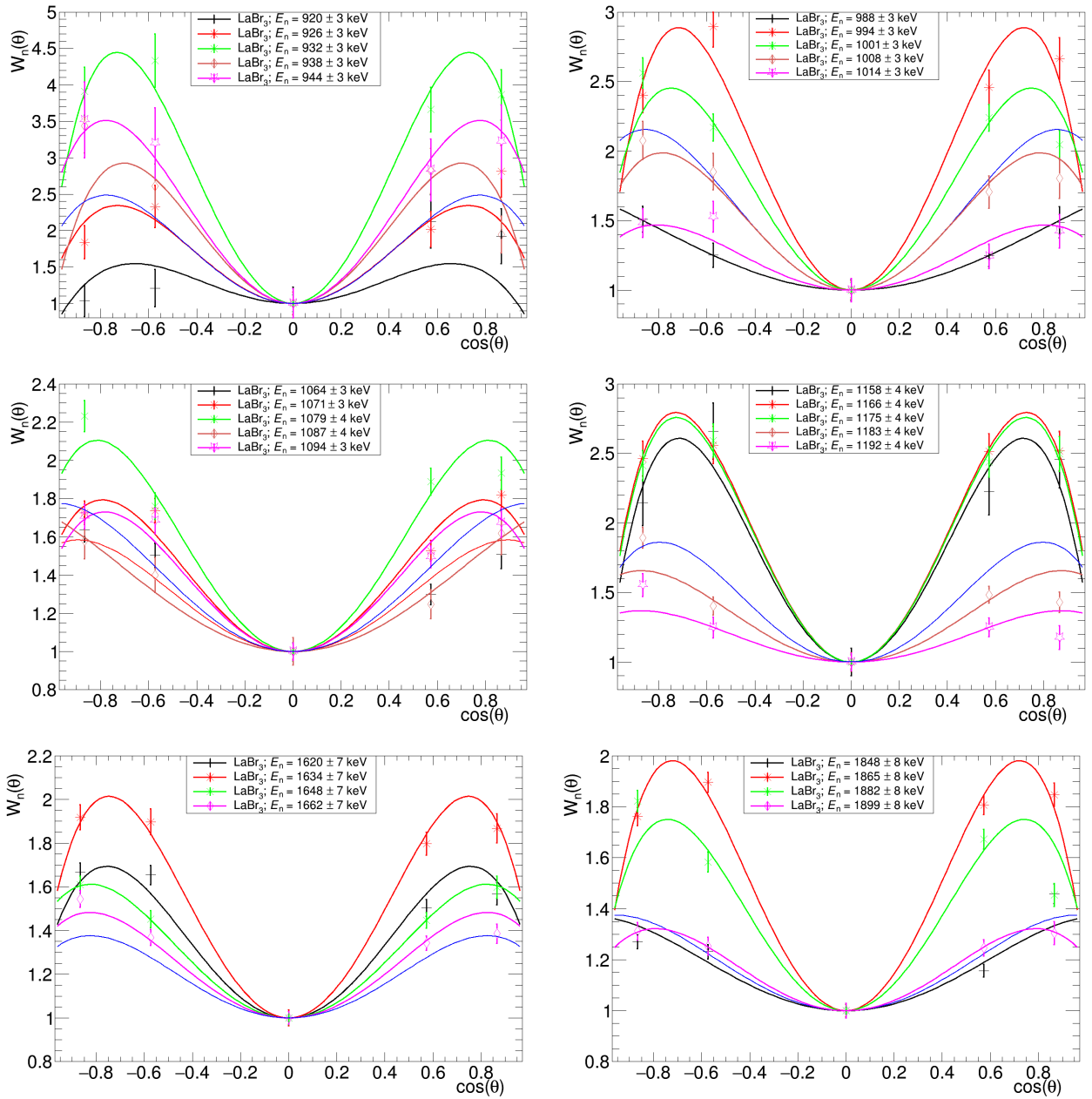
Figure 5.6.: The development (part I) of high resolution angular distribution data of LaBr$_3$ is plotted at different energy to show its remarkable energy dependence and width of some resonance structures like the one at about 1170 keV. The blue lines are from the data of D. L. Smith at comparable energies (see tab. 5.1).
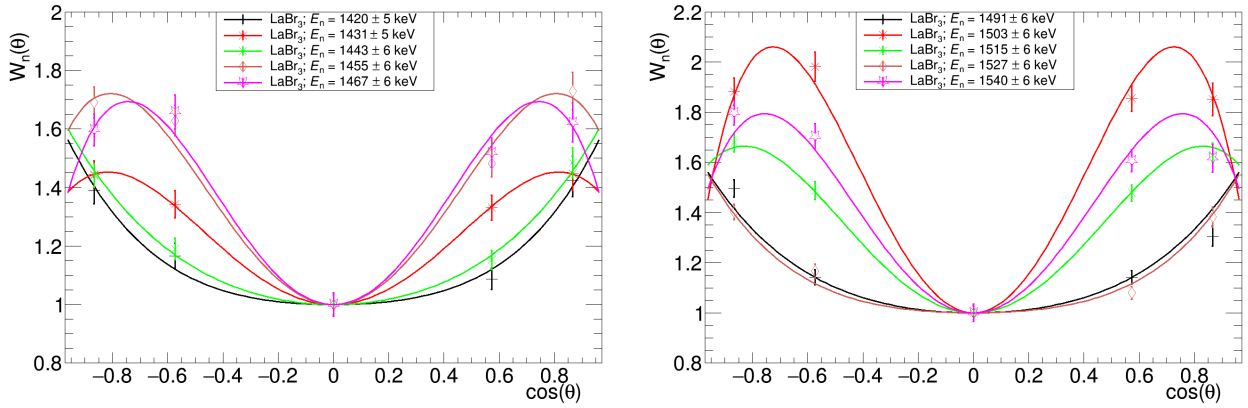
Figure 5.7.: The development (part II) of high resolution angular distribution data of LaBr$_3$ is plotted at different energy to show its remarkable energy dependence and how the a_4 term influence the shape. The blue lines are from the data of D. L. Smith at comparable energies (see tab. 5.1).

Outlook

In further research the cross section can be calculated by analysing the neutron flux with all its corrections by means of the fission chamber data. Using the analysed angular distributions, integrated cross sections are achievable. For the angular distribution, the neutron flux is only important if it is not measured at the same time. But the big advantage of the setup used here is the concurrence of this measurement. Prospectively the measurement of the 1238 keV and 1811 keV γ-rays will be analysed to gain insight into angular distributions of other transitions. In the future a correlation analysis of the measured γ-ray angular distribution and the inelastic and total cross sections measured with high resolution might allow to determine the average width and level spacing in the energy range of a few MeV neutron energy for the compound nucleus ^{57}Fe.

6. Summary

The inelastic scattering of ^{56}Fe has been investigated at the neutron time-of-flight facility nELBE. The γ-ray angular distribution from the first excited state in ^{56}Fe at $847\,$keV has been measured for different incident neutron energies in the range from threshold to $7\,$MeV.

The measurement was carried out using a homogeneous iron target of natural isotopic composition with a thickness of $4.5\,$mm. The γ-rays were detected in a new setup using five large HPGe detectors located under $30°$, $55°$, $90°$, $125°$ and $150°$ and five large LaBr$_3$ scintillation detectors under the same angles. The experimental data were stored in list mode files, so that the γ-ray energy and time-of-flight information from each detector was recorded in coincidence. The most important corrections to the data were made for the detection efficiencies in extended source geometry and the self-absorption of the γ-rays inside the target material. These corrections were simulated using the particle transport code GEANT4.

For the first time, high-resolution γ-ray angular distributions could be measured using a short flight path and the excellent time resolution of the LaBr$_3$ scintillation detectors. The neutron energy resolution amounts to typically $3\,$kev at $1\,$MeV and $10\,$keV at $2\,$MeV. The previously measured parameter of D. L. Smith can be spezified with higher resolution and more isolated data of resonant like structures are available.
The resonant structure found in the γ-ray angular distribution data are very similar to the inelastic scattering cross section. At low energies, these structures can be explained by resolved resonances and at energies above about $1.4\,$MeV neutron energy, the resonant structures can be interpreted as Ericsson fluctuations.

The angular anisotropy of the $847\,$keV transition decreases above the threshold for the second excited state and higher states due to the feeding through γ-ray cascade decay. With the γ-ray angular distributions of this thesis, a correction factor was determined for the inelastic scattering cross section measurement by Beyer et al. [BSH$^+$14], where only one HPGe under $125°$ was used and isotropic emission was asssumed. It was shown, that the gamma-ray angular distributions of $847\,$keV strongly depend on the incident neutron energy and that there is only isotropy in transition very far from the threshold.

A. Appendix

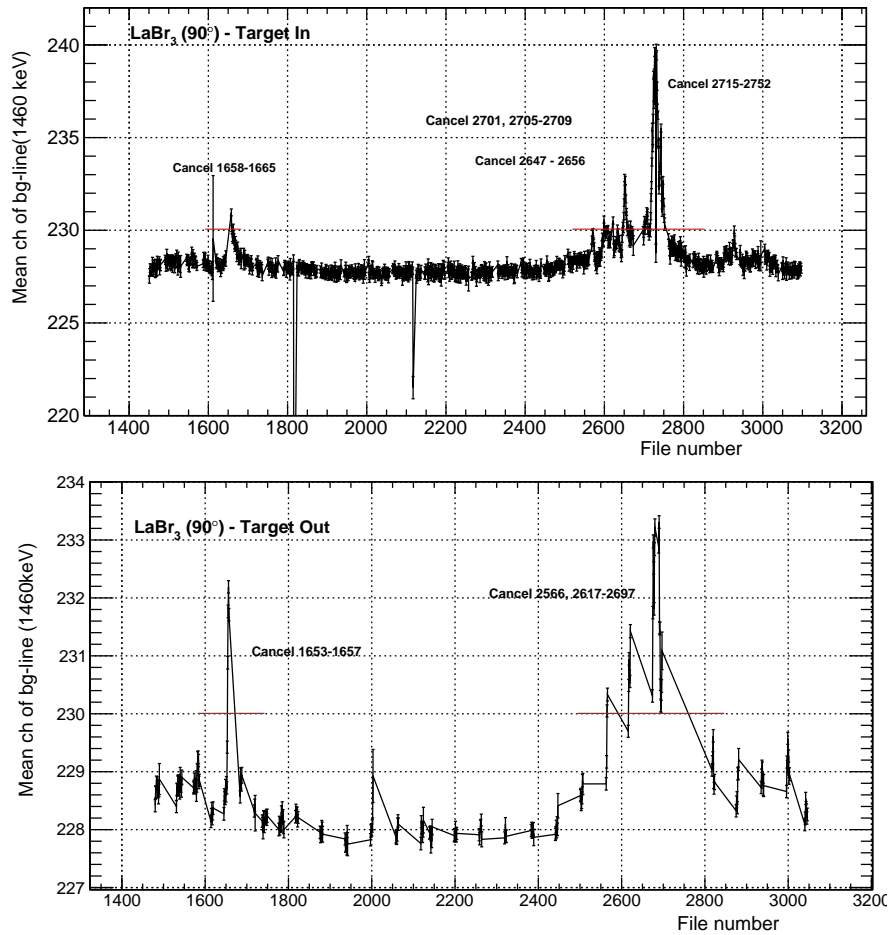The appendix with further figure, experimental schemes and additional information complete this work.

Figure A.1.: The plots show the mean channel of the self activity photons ($1460\,\mathrm{keV}$) above the file number and for deviations bigger than the peak width the files are not used in the analysis. Therefore some files were cancelled and did not contribute to the analysis.
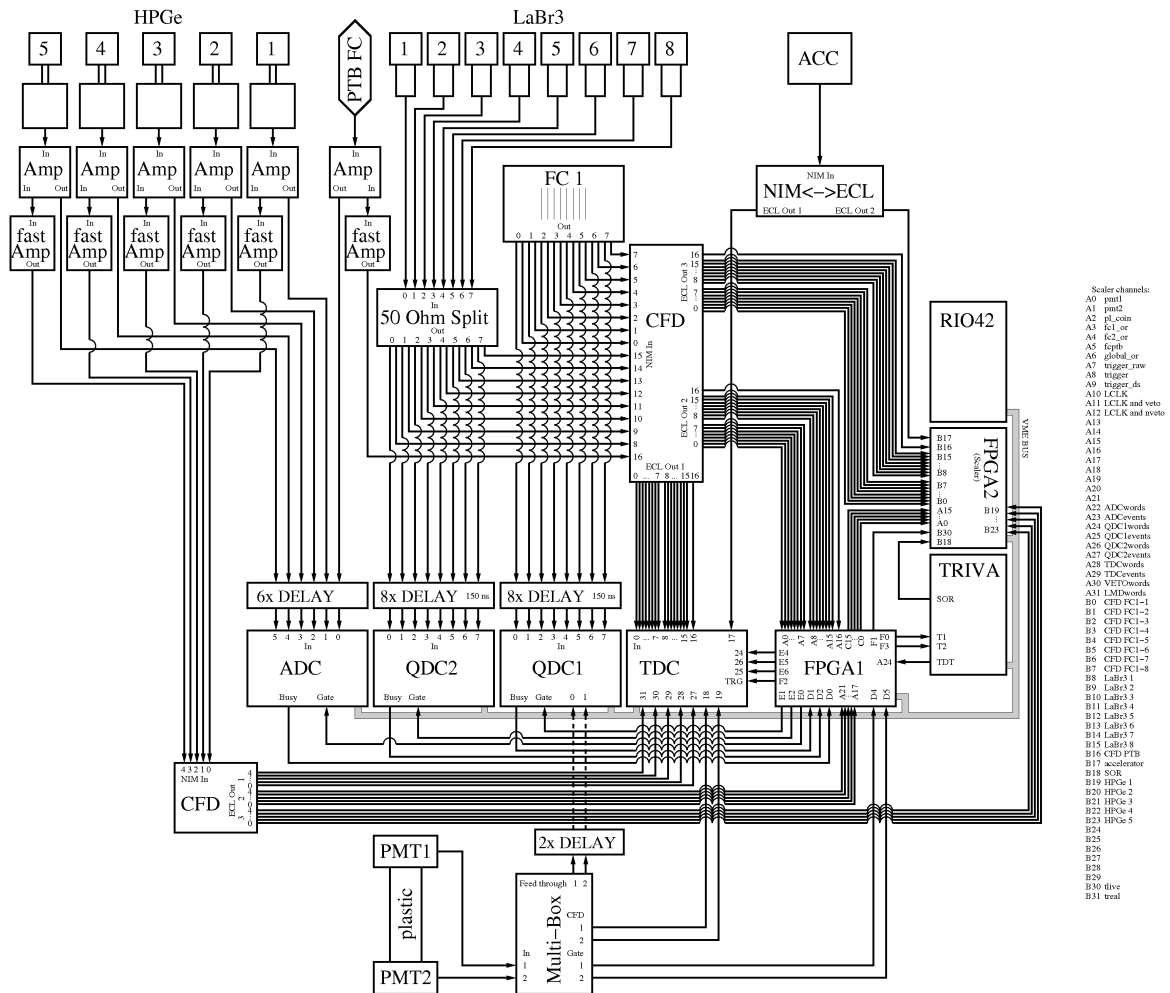
Figure A.2.: The electronic plan and the FPGA trigger logic of the experiment is shown. This heart piece of the experiment was planned, performed and logged by beamline scientist Dr. R. Beyer.
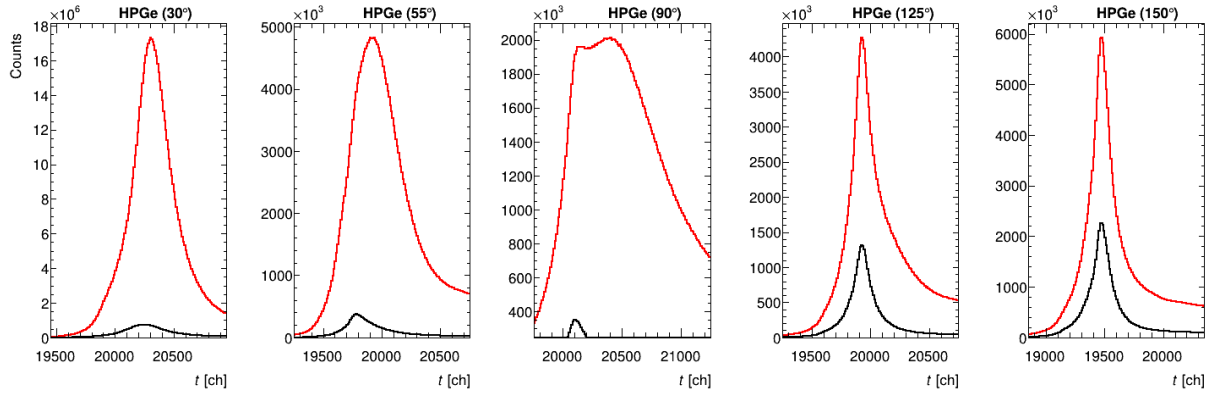
Figure A.3.: The gamma-flash of HPGe with target in (red) and out (black) of the beam. The peaks are broadened and it reflects the worse time resolution of the germanium detector.
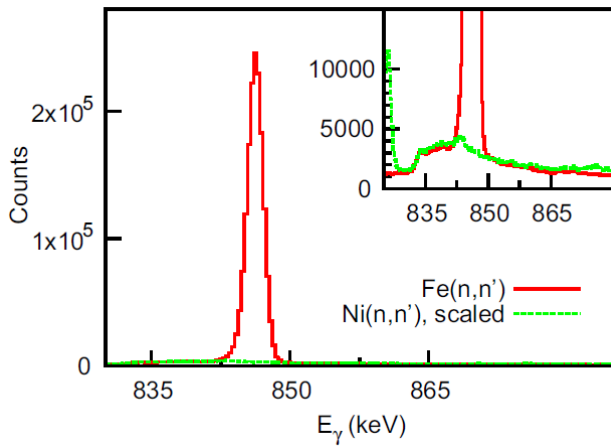
Figure A.4: At IRMM a Nickel target was used to study the neutron induzed background on the HPGe, because a gamma with 834 plus triangle shape from repulsion energy would overlap the proper ^{56}Fe-peak. The spectra is taken from Negret ET AL. [NBD+14].

Table A.1.: Overview of the calculated efficiency values from calibration point sources ^{137}Cs, ^{60}Co and ^{88}Y.

	LaBr$_3$					HPGe				
	30°	55°	90°	125°	150°	30°	55°	90°	125°	150°
ϵ_{661}	6.02	18.49	17.66	17.60	17.77	8.39	13.28	11.70	12.76	12.47
$\Delta\epsilon_{661}$	0.10	0.30	0.29	0.29	0.29	0.14	0.22	0.19	0.21	0.20
ϵ_{1173}	3.30	12.00	11.40	11.53	11.93	5.68	9.47	8.50	9.60	9.18
$\Delta\epsilon_{1173}$	0.05	0.19	0.18	0.18	0.19	0.09	0.15	0.13	0.15	0.14
ϵ_{1332}	3.04	11.29	10.66	10.96	11.49	5.23	8.82	7.96	8.92	8.50
$\Delta\epsilon_{1332}$	0.05	0.17	0.16	0.17	0.18	0.10	0.16	0.14	0.16	0.15
ϵ_{898}	4.58	14.95	14.94	15.09	15.42	6.94	11.41	10.42	11.38	11.00
$\Delta\epsilon_{898}$	0.06	0.20	0.20	0.20	0.21	0.09	0.15	0.14	0.15	0.15
ϵ_{1836}	2.31	9.10	8.94	9.08	9.18	4.14	7.30	6.55	7.35	6.89
$\Delta\epsilon_{1836}$	0.03	0.12	0.12	0.12	0.12	0.06	0.10	0.09	0.10	0.09

Table A.2.: Overview of the absorption correction factor of gamma energies of the three first exited states of ^{56}Fe.

	LaBr$_3$					HPGe				
	30°	55°	90°	125°	150°	30°	55°	90°	125°	150°
$c_{\mathrm{abs},\theta}(847\,\mathrm{keV})$	1.1251	1.1511	1.3655	1.4514	1.1853	1.1886	1.4645	1.3596	1.1462	1.1242
$\Delta c_{\mathrm{abs},\theta}(847\,\mathrm{keV})$	0.0012	0.0009	0.0011	0.0012	0.0009	0.0010	0.0011	0.0011	0.0008	0.0008
$c_{\mathrm{abs},\theta}(1238\,\mathrm{keV})$	1.1008	1.1218	1.2957	1.3639	1.1481	1.1509	1.3709	1.2890	1.1187	1.0990
$\Delta c_{\mathrm{abs},\theta}(1238\,\mathrm{keV})$	0.0012	0.0008	0.0010	0.0011	0.0009	0.0010	0.0010	0.0010	0.0008	0.0008
$c_{\mathrm{abs},\theta}(1811\,\mathrm{keV})$	1.0816	1.0995	1.2419	1.2991	1.1218	1.1247	1.3038	1.2369	1.0980	1.0845
$\Delta c_{\mathrm{abs},\theta}(1811\,\mathrm{keV})$	0.0012	0.0008	0.0009	0.0010	0.0008	0.0009	0.0010	0.0010	0.0008	0.0008

Table A.3.: Result of 2 ns binning LaBr$_3$ with parameter a_2 and a_4 for the fitted angular distribution and the correction factor $W(125°)$, which demonstrates the anisotropy.

$E_n \pm \Delta E_n$ [keV]	$a_2 \pm \Delta a_2$	$a_4 \pm \Delta a_4$	$W(125°) \pm \Delta W(125°)$
863 ± 2	-0.088 ± 0.221	-1.034 ± 0.332	1.399 ± 0.128
869 ± 3	0.518 ± 0.082	-0.514 ± 0.111	1.195 ± 0.043
874 ± 2	0.425 ± 0.089	-0.358 ± 0.120	1.135 ± 0.046
880 ± 3	-0.316 ± 0.146	-0.959 ± 0.222	1.371 ± 0.085
885 ± 2	0.291 ± 0.162	-0.891 ± 0.229	1.341 ± 0.088
891 ± 3	0.423 ± 0.265	-0.827 ± 0.365	1.316 ± 0.141
896 ± 2	0.347 ± 0.344	-1.224 ± 0.482	1.469 ± 0.186
902 ± 3	0.461 ± 0.118	-0.473 ± 0.161	1.179 ± 0.062
908 ± 3	0.350 ± 0.181	-0.368 ± 0.249	1.140 ± 0.096
914 ± 3	0.335 ± 0.127	-0.374 ± 0.175	1.142 ± 0.067
920 ± 3	0.019 ± 0.187	-0.525 ± 0.275	1.202 ± 0.106
926 ± 3	0.380 ± 0.131	-0.623 ± 0.182	1.238 ± 0.070
932 ± 3	0.591 ± 0.098	-0.956 ± 0.135	1.364 ± 0.052
938 ± 3	0.343 ± 0.126	-0.890 ± 0.175	1.341 ± 0.067
944 ± 3	0.672 ± 0.172	-0.658 ± 0.233	1.249 ± 0.090
950 ± 3	0.702 ± 0.278	-0.438 ± 0.368	1.164 ± 0.142
956 ± 3	0.381 ± 0.105	0.286 ± 0.139	0.887 ± 0.054
962 ± 3	0.396 ± 0.113	-0.038 ± 0.152	1.012 ± 0.059
969 ± 3	0.253 ± 0.111	-0.652 ± 0.156	1.249 ± 0.060
975 ± 3	0.443 ± 0.074	-0.334 ± 0.100	1.126 ± 0.039
981 ± 3	0.411 ± 0.056	-0.152 ± 0.075	1.056 ± 0.029
988 ± 3	0.349 ± 0.067	-0.040 ± 0.090	1.013 ± 0.035
994 ± 3	0.411 ± 0.056	-0.800 ± 0.078	1.305 ± 0.030
1001 ± 3	0.453 ± 0.048	-0.584 ± 0.066	1.222 ± 0.025
1008 ± 3	0.423 ± 0.074	-0.380 ± 0.101	1.144 ± 0.039
1014 ± 3	0.260 ± 0.073	-0.202 ± 0.100	1.076 ± 0.038
1021 ± 3	0.279 ± 0.090	-0.211 ± 0.123	1.079 ± 0.047
1028 ± 3	0.343 ± 0.107	-0.266 ± 0.146	1.100 ± 0.056
1035 ± 3	0.371 ± 0.096	-0.453 ± 0.132	1.172 ± 0.051
1042 ± 3	0.364 ± 0.050	0.091 ± 0.066	0.963 ± 0.025
1049 ± 3	0.215 ± 0.054	0.097 ± 0.073	0.961 ± 0.028
1057 ± 4	0.350 ± 0.051	-0.132 ± 0.069	1.049 ± 0.027
1064 ± 3	0.346 ± 0.043	-0.161 ± 0.058	1.060 ± 0.022
1071 ± 3	0.370 ± 0.038	-0.321 ± 0.052	1.121 ± 0.020
1079 ± 4	0.488 ± 0.042	-0.357 ± 0.056	1.135 ± 0.022
1087 ± 4	0.394 ± 0.064	-0.062 ± 0.086	1.021 ± 0.033

$E_n \pm \Delta E_n$ [keV]	$a_2 \pm \Delta a_2$	$a_4 \pm \Delta a_4$	$W(125°) \pm \Delta W(125°)$
1094 ± 3	0.339 ± 0.041	-0.317 ± 0.055	1.120 ± 0.021
1102 ± 4	0.402 ± 0.045	-0.134 ± 0.060	1.049 ± 0.023
1110 ± 4	0.366 ± 0.054	-0.091 ± 0.072	1.033 ± 0.028
1118 ± 4	0.412 ± 0.051	-0.394 ± 0.069	1.149 ± 0.027
1126 ± 4	0.486 ± 0.050	-0.460 ± 0.067	1.174 ± 0.026
1134 ± 4	0.523 ± 0.064	-0.473 ± 0.086	1.179 ± 0.033
1142 ± 4	0.373 ± 0.047	-0.375 ± 0.063	1.142 ± 0.024
1150 ± 4	0.218 ± 0.058	-0.137 ± 0.078	1.051 ± 0.030
1158 ± 4	0.369 ± 0.082	-0.747 ± 0.114	1.285 ± 0.044
1166 ± 4	0.437 ± 0.056	-0.737 ± 0.078	1.281 ± 0.030
1175 ± 4	0.427 ± 0.050	-0.737 ± 0.069	1.281 ± 0.027
1183 ± 4	0.374 ± 0.045	-0.191 ± 0.060	1.071 ± 0.023
1192 ± 4	0.236 ± 0.058	-0.121 ± 0.078	1.045 ± 0.030
1201 ± 4	0.292 ± 0.053	-0.586 ± 0.073	1.224 ± 0.028
1209 ± 4	0.320 ± 0.052	-0.433 ± 0.072	1.165 ± 0.028
1218 ± 4	0.247 ± 0.041	-0.257 ± 0.056	1.097 ± 0.022
1227 ± 4	0.322 ± 0.039	-0.083 ± 0.052	1.030 ± 0.020
1236 ± 4	0.417 ± 0.068	-0.426 ± 0.092	1.162 ± 0.036
1246 ± 5	0.178 ± 0.056	-0.316 ± 0.077	1.120 ± 0.030
1255 ± 4	0.178 ± 0.063	-0.276 ± 0.086	1.105 ± 0.033
1265 ± 5	0.401 ± 0.055	-0.210 ± 0.075	1.078 ± 0.029
1274 ± 4	0.374 ± 0.056	-0.121 ± 0.074	1.044 ± 0.029
1284 ± 5	0.268 ± 0.049	0.061 ± 0.065	0.975 ± 0.025
1294 ± 5	0.302 ± 0.036	0.055 ± 0.048	0.977 ± 0.018
1304 ± 5	0.353 ± 0.040	0.277 ± 0.051	0.891 ± 0.020
1314 ± 5	0.375 ± 0.051	0.066 ± 0.068	0.972 ± 0.026
1324 ± 5	0.350 ± 0.043	-0.090 ± 0.057	1.032 ± 0.022
1334 ± 5	0.371 ± 0.041	-0.071 ± 0.054	1.025 ± 0.021
1344 ± 5	0.469 ± 0.041	-0.065 ± 0.054	1.022 ± 0.021
1355 ± 5	0.387 ± 0.033	0.077 ± 0.043	0.968 ± 0.017
1365 ± 5	0.452 ± 0.037	-0.092 ± 0.049	1.032 ± 0.019
1376 ± 5	0.384 ± 0.029	0.062 ± 0.038	0.974 ± 0.015
1387 ± 5	0.356 ± 0.032	0.260 ± 0.041	0.898 ± 0.016
1398 ± 6	0.352 ± 0.042	-0.465 ± 0.057	1.177 ± 0.022
1409 ± 5	0.231 ± 0.033	-0.096 ± 0.044	1.035 ± 0.017
1420 ± 5	0.334 ± 0.035	0.080 ± 0.046	0.967 ± 0.018
1431 ± 5	0.259 ± 0.034	-0.186 ± 0.046	1.070 ± 0.018
1443 ± 6	0.355 ± 0.030	0.043 ± 0.039	0.981 ± 0.015

$E_{\mathrm{n}} \pm \Delta E_{\mathrm{n}}$ [keV]	$a_2 \pm \Delta a_2$	$a_4 \pm \Delta a_4$	$W(125°) \pm \Delta W(125°)$
1455 ± 6	0.362 ± 0.033	-0.278 ± 0.045	1.105 ± 0.017
1467 ± 6	0.273 ± 0.036	-0.374 ± 0.049	1.142 ± 0.019
1479 ± 6	0.361 ± 0.029	0.008 ± 0.038	0.994 ± 0.015
1491 ± 6	0.334 ± 0.025	0.057 ± 0.033	0.976 ± 0.013
1503 ± 6	0.317 ± 0.031	-0.555 ± 0.043	1.212 ± 0.016
1515 ± 6	0.358 ± 0.025	-0.234 ± 0.033	1.088 ± 0.013
1527 ± 6	0.328 ± 0.024	0.080 ± 0.032	0.967 ± 0.012
1540 ± 6	0.323 ± 0.030	-0.384 ± 0.041	1.146 ± 0.016
1553 ± 6	0.388 ± 0.029	-0.317 ± 0.039	1.119 ± 0.015
1566 ± 6	0.370 ± 0.026	-0.138 ± 0.035	1.051 ± 0.013
1579 ± 6	0.268 ± 0.027	-0.197 ± 0.036	1.074 ± 0.014
1593 ± 7	0.337 ± 0.026	-0.055 ± 0.035	1.019 ± 0.013
1606 ± 6	0.210 ± 0.023	-0.087 ± 0.031	1.032 ± 0.012
1620 ± 7	0.292 ± 0.027	-0.351 ± 0.037	1.133 ± 0.014
1634 ± 7	0.363 ± 0.032	-0.474 ± 0.044	1.180 ± 0.017
1648 ± 7	0.332 ± 0.027	-0.226 ± 0.036	1.085 ± 0.014
1662 ± 7	0.277 ± 0.027	-0.189 ± 0.036	1.071 ± 0.014
1676 ± 7	0.144 ± 0.029	-0.117 ± 0.039	1.044 ± 0.015
1691 ± 7	0.256 ± 0.032	-0.237 ± 0.044	1.090 ± 0.017
1705 ± 7	0.153 ± 0.027	0.030 ± 0.036	0.988 ± 0.014
1720 ± 7	0.082 ± 0.029	-0.040 ± 0.039	1.015 ± 0.015
1736 ± 8	0.170 ± 0.033	-0.324 ± 0.045	1.124 ± 0.017
1751 ± 7	0.233 ± 0.027	-0.180 ± 0.036	1.068 ± 0.014
1767 ± 8	0.155 ± 0.026	-0.329 ± 0.036	1.126 ± 0.014
1783 ± 8	0.109 ± 0.027	-0.108 ± 0.037	1.041 ± 0.014
1799 ± 8	0.114 ± 0.031	-0.183 ± 0.043	1.070 ± 0.016
1815 ± 8	0.073 ± 0.030	-0.209 ± 0.041	1.080 ± 0.016
1831 ± 8	0.112 ± 0.027	-0.192 ± 0.036	1.073 ± 0.014
1848 ± 8	0.235 ± 0.022	-0.061 ± 0.030	1.022 ± 0.011
1865 ± 8	0.292 ± 0.022	-0.537 ± 0.030	1.205 ± 0.011
1882 ± 8	0.285 ± 0.025	-0.400 ± 0.034	1.152 ± 0.013
1899 ± 8	0.183 ± 0.027	-0.160 ± 0.037	1.060 ± 0.014
1917 ± 9	0.205 ± 0.025	-0.135 ± 0.034	1.051 ± 0.013
1935 ± 9	0.226 ± 0.021	-0.012 ± 0.028	1.003 ± 0.011
1953 ± 9	0.148 ± 0.023	-0.107 ± 0.031	1.040 ± 0.012
1971 ± 9	0.214 ± 0.023	-0.126 ± 0.030	1.047 ± 0.012
1990 ± 9	0.234 ± 0.021	-0.151 ± 0.028	1.057 ± 0.011

Bibliography

[ABF+07]   E. Altstadt, C. Beckert, H. Freiesleben, V. Galindo, E. Grosse, A.R. Junghans, J. Klug, B. Naumann, S. Schneider, R. Schlenk, A. Wagner, and F.-P. Weiss. A photo-neutron source for time-of-flight measurements at the radiation source ELBE. *Annals of Nuclear Energy*, 34(1–2):36 − 50, 2007.

[AMATB+15]   J. Adamczewski-Musch, M. Al-Turany, D. Bertini, H. G. Essel, and S. Linev. *The Go4 Analysis Framework Introduction V5.0.* GSI, Gesellschaft für Schwerionenforschung mbH, Planckstrasse 1, D-64291 Darmstadt Germany, 06 2015.

[BB52]   John M. Blatt and L. C. Biedenharn. The Angular Distribution of Scattering and Reaction Cross Sections. *Rev. Mod. Phys.*, 24:258–272, Oct 1952.

[BBE+13]   R. Beyer, E. Birgersson, Z. Elekes, A. Ferrari, E. Grosse, R. Hannaske, A.R. Junghans, T. Kögler, R. Massarczyk, A. Matić, R. Nolte, R. Schwengner, and A. Wagner. Characterization of the neutron beam at nELBE. *Nuclear Instruments and Methods in Physics Research Section A: Accelerators, Spectrometers, Detectors and Associated Equipment*, 723:151 − 162, 2013.

[Ber07]   Carlos A. Bertulani. *Nuclear Physics in a Nutshell.* Princeton University Press, 2007. ISBN-13: 978-0-691-12505-3.

[Bey14]   Roland Beyer. *Inelastische Streuung schneller Neutronen an ^{56}Fe.* PhD thesis, TU Dresden, 2014.

[BHS+98]   M.J. Berger, J.H. Hubbell, S.M. Seltzer, J. Chang, J.S. Coursey, R. Sukumar, D.S. Zucker, and K. Olsen. XCOM: Photon Cross Sections Database, 03 1998. NIST Standard Reference Database 8 (XGAM).

[BLS71]   P. Boschung, J.T. Lindow, and E.F. Shrader. Scattering of fast neutrons by ^{12}C, ^{54}Fe, ^{56}Fe, ^{58}Ni and ^{60}Ni. *Nuclear Physics A*, 161(2):593–609, 1971.

[Boh36]   Niels Bohr. Neutron Capture and Nuclear Constitution. *Nature*, pages 344 − 348, Feb. 1936.

[Bru02]   C.R Brune. Gaussian quadrature applied to experimental γ-ray yields. *Nuclear Instruments and Methods in Physics Research Section A: Accelerators, Spectrometers, Detectors and Associated Equipment*, 493:106 − 110, 2002.

[BSH+14]   R. Beyer, R. Schwengner, R. Hannaske, A.R. Junghans, R. Massarczyk, M. Anders, D. Bemmerer, A. Ferrari, A. Hartmann, T. Kögler, M. Röder, K. Schmidt, and A. Wagner. Inelastic scattering of fast neutrons from excited states in ^{56}Fe. *Nuclear Physics A*, 927:41–52, July 2014.

[BVE+68]   E. Barnard, J. A. M. De Villiers, C. A. Engelbrecht, D. Reitmann, and A.B. Smith. High-Resolution Fast-Neutron Cross Sections of Iron. *North-Holland Publishing Co., Amsterdam*, Nuclear Physics(A118):321–346, 1968.

[CDB+14]   M.B. Chadwick, E. Dupont, E. Bauge, A. Blokhin, O. Bouland, D.A. Brown, R. Capote, A. Carlson, Y. Danon, C. De Saint Jean, M. Dunn, U. Fischer, R.A. Forrest, S.C. Frankle, T. Fukahori, Z. Ge, S.M. Grimes, G.M. Hale, M. Herman, A. Ignatyuk, M. Ishikawa, N. Iwamoto, O. Iwamoto, M. Jandel, R. Jacqmin, T. Kawano, S. Kunieda, A. Kahler, B. Kiedrowski, I. Kodeli, A.J. Koning, L. Leal, Y.O. Lee, J.P. Lestone, C. Lubitz, M. MacInnes, D. McNabb, R. McKnight, M. Moxon, S. Mughabghab, G. Noguere, G. Palmiotti, A. Plompen, B. Pritychenko, V. Pronyaev, D. Rochman, P. Romain, D. Roubtsov, P. Schillebeeckx, M. Salvatores, S. Simakov, E.Sh. Soukhovitski i, J.C. Sublet, P. Talou, I. Thompson, A. Trkov, R. Vogt, and S. van der Marck. The CIELO Collaboration: Neutron Reactions on ^{1}H, ^{16}O, ^{56}Fe, ^{235,238}U, and ^{239}Pu. *Nuclear Data Sheets*, 118:1 – 25, 2014.

[CIE]   Iron Cielo Evaluation Project [online] (https://ndclx4.bnl.gov/gf/project/cielo_iron/).

[Day56]   Robert B. Day. Gamma Rays from Neutron Inelastic Scattering. *Phys. Rev.*, 102(3):767–787, May 1956.

[DMP73]   J. K. Dickens, G. L. Morgan, and F. G. Perey. Neutron-Induced Gamma-Ray Production in Iron for the Energy Range $0.8 \leq E_{n} \leq 20$ MeV. *Nuclear Science and Engineering: 50, 311-336 (1973)*, 50:311–336, 1973.

[EK10]   H.G. Essel and N. Kurz. *GSI Multi-Branch System Reference Manual*. GSI, Gesellschaft für Schwerionenforschung mbH, Planckstrasse 1, D-64291 Darmstadt Germany, 08 2010.

[Eri60]   Torleif Ericson. The Statistical Model and Nuclear Level Densities. *Advances in Physics*, 9(36):425–511, 1960.

[EXF]   Experimental Nuclear Reaction Data (EXFOR) (https://www-nds.iaea.org/exfor/exfor.htm).

[FKK80]   Herman Feshbach, Arthur Kerman, and Steven Koonin. The statistical theory of multi-step compound and direct reactions. *Annals of Physics*, 125(2):429–476, April 1980.

[FMP96]   G. Fehrenbacher, R. Meckbach, and H.G. Paretzke. Fast neutron detection with germanium detectors: computation of response functions for the 692 keV inelastic scattering peak. *Nuclear Instruments and Methods in Physics Research Section A: Accelerators, Spectrometers, Detectors and Associated Equipment,* 372(1-2):239–245, March 1996.

[HF52]   Walter Hauser and Herman Feshbach. The Inelastic Scattering of Neutrons. *Phys. Rev.,* 87:366–373, Jul 1952.

[HTB13]   M. Herman, A. Trkov, and D. Brown. Fe isotope evaluation within the CIELO project. In *Nuclear Measurements, Evaluations and Applications (NEMEA-7) Collaborative International Evaluated Library Organisation (CIELO),* Nuclear Science NEA/NSC/DOC(2014)13, pages 65–73, Geel, Belgium, November 2013.

[II13]   Osamu Iwamoto and Nobuyuki Iwamoto. Review of nuclear data of major actinides and ^{56}Fe in JENDL-4.0. In *Nuclear Measurements, Evaluations and Applications (NEMEA-7) Collaborative International Evaluated Library Organisation (CIELO),* Nuclear Science NEA/NSC/DOC(2014)13, pages 75–83, Geel, Belgium, November 2013.

[JEN]   Japanese Evaluated Nuclear Data Library (JENDL) (http://wwwndc.jaea.go.jp/jendl/jendl.html).

[K̈16]   Toni Kögler. *Bestimmung des neutroneninduzierten Spaltquerschnitts von $^{242}Pu.$* PhD thesis, TU Dresden; HZDR, 2016. to be published.

[K.A14]   K.A. Olive et al. Particle Data Group (PDG). *Chin. Phys. C,* 38(090001), 2014.

[KMM⁺77]   I. A. Korzh, V. A. Mishchenko, E. N. Mozhzhukhin, N. M. Pravdivij, and I. E. Sanzhur. Differential Scattering Cross Sections Of $1.5 - 3.0$ MeV Neutrons For Ti, Fe And Bi. *Ukrainskii Fizichnii Zhurnal,* 22:87, 1977.

[KP70]   W. E. Kinney and F. G. Perey. Neutron Elastic- and Inelaslic-Scattering Cross Sections for ^{56}Fe in the Energy Range 4.19 to 8.56 MeV. *OKNL,* 45, 6 1970.

[KTW15]   T. Kawano, P. Talou, and H. A. Weidenmüller. Random-matrix approach to the statistical compound nuclear reaction at low energies using the Monte Carlo technique. *Phys. Rev. C,* 92:044617, Oct 2015.

[Lea35]   D. E. Lea. Secondary Gamma Rays Excited by the Passage of Neutrons through Matter. *Proceedings of the Royal Society of London A: Mathematical, Physical and Engineering Sciences,* 150(871):637–668, July 1935.

[MF63]   J. B. Marion and J. L. Fowler. *Fast Neutron Physics, Part II: Experiment and Theory,* volume IV. Interscience Publishers, New York-London, 1963.

[MFRP+83]   A. Marcinkowski, R.W. Finlay, G. Randers-Pehrson, C.E. Brient, J.E. O'Donnell, and K. Stankiewicz. Neutron emission spectra and angular distributions at 25.7 MeV neutron bombarding energies. *Nuclear Physics A*, 402(2):220–234, June 1983.

[MRW10]   G. E. Mitchell, A. Richter, and H. A. Weidenmüller. Random matrices and chaos in nuclear physics: Nuclear reactions. *Rev. Mod. Phys.*, 82:2845–2901, Oct 2010.

[NBD+14]   A. Negret, C. Borcea, Ph. Dessagne, M. Kerveno, A. Olacel, A. J. M. Plompen, and M. Stanoiu. Cross-section measurements for the 56Fe(n, xnγ) reactions. *Physical Review C*, 90(3)(034602), 09 2014.

[NCB+07]   R. Nicolini, F. Camera, N. Blasi, S. Brambilla, R. Bassini, C. Boiano, A. Bracco, F.C.L. Crespi, O. Wieland, G. Benzoni, S. Leoni, B. Million, D. Montanari, and A. Zalite. Investigation of the properties of a $1''x1''$ LaBr$_3$:Ce scintillator. *Nuclear Instruments and Methods in Physics Research Section A: Accelerators, Spectrometers, Detectors and Associated Equipment*, 582(2):554–561, November 2007.

[NND]   National Nulcear Data Center (NNDC) - (http://www.nndc.bnl.gov/).

[PRSZge]   B. Povh, K. Rith, C. Scholz, and F. Zetsche. *Teilchen und Kerne.* Springer Verlag, 1997; 4.Auflage. ISBN 3-540-61737-X.

[Rei16]   Tobias Reinhardt. . PhD thesis, TU Dresden; HZDR, 2016. to be published / private communication.

[Sat56]   G. R. Satchler. Angular Distribution of Nuclear Reaction Products. *Phys. Rev.*, 104:1198–1200, Nov 1956.

[SBD+12]   P. Schillebeeckx, B. Becker, Y. Danon, K. Guber, H. Harada, J. Heyse, A.R. Junghans, S. Kopecky, C. Massimi, M.C. Moxon, N. Otuka, I. Sirakov, and K. Volev. Determination of Resonance Parameters and their Covariances from Neutron Induced Reaction Cross Section Data. *Nuclear Data Sheets*, 113(12):3054 – 3100, 2012. Special Issue on Nuclear Reaction Data.

[SGG37]   G. T. Seaborg, G. E. Gibson, and D. C. Grahame. Inelastic Scattering of Fast Neutrons. *Phys. Rev.*, 52:408–414, Sep 1937.

[She63]   Eric Sheldon. Angular Correlation in Inelastic Nucleon Scattering. *Reviews of Modern Physics*, 35(4), 10 1963.

[Smi76]   Donald L. Smith. Fast-Neutron-Gamma-Ray Production From Elemental Iron: $E_n \lesssim 2\,\mathrm{MeV}$. *Argonne National Laboratory, Argonne, Illinois 60439, U.S.A.*, ANL/NDM-20, 05 1976. Nuclear Data and Measurements Series.

[SMKN94]   D. Schmidt, W. Mannhart, H. Klein, and R. Nolte. Neutron Scattering on Natural Iron at Incident Energies between 9.4 and 15.2 MeV. Neutronenphysik 20, PTB, 11 1994. ISBN 3-89429-552-X.

[VCK71]   F. Voss, S. Cierjacks, and L. Kropp. Measurement of High Resolution γ-Ray Production Cross Sections in Inelastic Neutron Scattering on Al and Fe between 0.8 and 13 MeV. In *Third Conference on Neutron Cross Sections and Technology, Knoxville, Tennessee*, 1971.

List of Figures

List of Tables

Danksagung

Am Ende meiner Masterarbeit und damit am Ende meines Studiums ist es an der Zeit, Danke zu sagen:

Ein großer Dank gebührt meinen Eltern und Großeltern, welche mich zeitlebens schon bei allem, was ich an, großherzig unterstützen und auf die mich immer verlassen kann.
Von ganzem Herzen danke ich meiner Herzensdame Frieda. Fast alle Semester hat sie mich schon begleitet, in manchen Wochen sehr nah beieinander, in einigen wieder weit voneinander entfernt und trotzdem stets in Liebe verbunden. Das haben wir vor gut $1\frac{1}{2}$ Jahren besiegelt mit unserer genialen Hochzeit. Für die Unterstützung in den letzten Wochen vor der Abgabe dieser Arbeit danke ich dir besonders.

Ich möchte mich ebenfalls bei all den Kollegen am HZDR, im Speziellen im 2.Stock des Gebäudes 620, bedanken für die erheiternde tägliche Mahlzeit und vielerlei guter Gespräche über die Jahre hinweg.
Besonderer Dank gilt meinem Betreuer Dr. Arnd R. Junghans, der stets den Fortschritt der Arbeit im Auge hatte und für Fragen und hilfreichen Anmerkungen zur Verfügung stand. Außerdem hat er mir ermöglicht, meine Ergebnisse auf einem CHANDA-Workshop in Paris vorzutragen und einen Posterpreis auf einer ICTP-IAEA-Schule in Triest zu gewinnen.
Ich wäre aber nie so weit gekommen, wenn mir die Kollegen aus meinem Büro Roland Beyer und Toni Kögler nicht so gut zur Seite gestanden wären und mir im 1x1 des Programmierens der Datenanalyse und im Verständnis des Experiments unglaublich weitergeholfen hätten. Vielen Dank an Toni, dass du mir alle meine ROOT und Go4-Fragen auch gern zwei- oder dreimal erklärt hast und an Roland, dass du immer für Fragen/Antworten zur Seite saßt.
Für wissenschaftlichen Diskurs, Anmerkungen und der eigentlichen Beantragung und Planung des Experiments geht mein Dank an Roland Schwengner. Letztlich bedanke ich mich bei dem Abteilungsleiter Andreas Wagner.

Für den sportlichen Ausgleich bedanke ich mich bei meiner Volleyballmannschaft und meinen Dart-Sympathisanten. Allen Kommilitonnen, Mitbewohnern, ICF'lern und Freunden danke ich für eine tolle Studienzeit in einer noch schöneren Stadt.

Erklärung

Hiermit versichere ich, dass ich die vorliegende Arbeit ohne unzulässige Hilfe Dritter und ohne Benutzung anderer als der angegebenen Hilfsmittel angefertigt habe. Die als fremde Quellen direkt oder indirekt übernommenen Gedanken sind als solche kenntlich gemacht. Die Arbeit wurde bisher weder im Inland noch im Ausland in gleicher oder ähnlicher Form einer anderen Prüfungsbehörde vorgelegt. Die vorgelegte Arbeit wurde am Helmholtz-Zentrum Dresden-Rossendorf, Institut für Strahlenphysik, im Zeitraum von Januar 2015 bis Dezember 2016 angefertigt.

Mirco Dietz
Dresden, 18. Februar 2016